DTIC FILE COPY

①

Office of Naval Research

Contract N00014-89-J-1023
Contract N00014-89-J-1565
National Sciences Foundation Grant DMR-89-12927

EFFECT OF LEADS AND QUANTUM FLUCTUATIONS IN SMALL SUPERCONDUCTING TUNNEL JUNCTIONS

AD-A227 311

DTIC
S ELECTE D
SEP 27 1990
B

By

Alan Thornton Johnson, Jr.

August 1990

Technical Report No. 30

This document has been approved for public release and sale; its distribution is unlimited. Reproduction in whole or in part is permitted by the U.S. Government.

Division of Applied Sciences
Harvard University · Cambridge, Massachusetts

90 09 26 268

Unclassified
SECURITY CLASSIFICATION OF THIS PAGE

REPORT DOCUMENTATION PAGE

Form Approved
OMB No 0704-0188

1a. REPORT SECURITY CLASSIFICATION
Unclassified

1b. RESTRICTIVE MARKINGS

2a. SECURITY CLASSIFICATION AUTHORITY
N/A

2b. DECLASSIFICATION / DOWNGRADING SCHEDULE

3. DISTRIBUTION / AVAILABILITY OF REPORT
Unclassified/unlimited

4. PERFORMING ORGANIZATION REPORT NUMBER(S)
Technical Report No. 30

5. MONITORING ORGANIZATION REPORT NUMBER(S)

6a. NAME OF PERFORMING ORGANIZATION
Harvard University

6b. OFFICE SYMBOL *(If applicable)*
N/A

7a. NAME OF MONITORING ORGANIZATION
Office of Naval Research

6c. ADDRESS *(City, State, and ZIP Code)*
Division of Applied Sciences
Harvard University
Cambridge, MA 02138

7b. ADDRESS *(City, State, and ZIP Code)*
800 N. Quincy Street
Arlington, VA 22217

8a. NAME OF FUNDING / SPONSORING ORGANIZATION
Office of Naval Research

8b. OFFICE SYMBOL *(If applicable)*

9. PROCUREMENT INSTRUMENT IDENTIFICATION NUMBER
N00014-89-J-1023

8c. ADDRESS *(City, State, and ZIP Code)*
800 N. Quincy Street
Arlington, VA 22217

10. SOURCE OF FUNDING NUMBERS

PROGRAM ELEMENT NO.	PROJECT NO.	TASK NO	WORK UNIT ACCESSION NO

11. TITLE *(Include Security Classification)*
Effect of Leads and Quantum Fluctuations in Small Superconducting Tunnel Junctions (Unclassified)

12. PERSONAL AUTHOR(S)
Alan Thornton Johnson, Jr.

13a. TYPE OF REPORT
Interim (Technical)

13b. TIME COVERED
FROM ________ TO ________

14. DATE OF REPORT *(Year, Month, Day)*
August 1990

15. PAGE COUNT
156

16. SUPPLEMENTARY NOTATION

17. COSATI CODES

FIELD	GROUP	SUB-GROUP

18. SUBJECT TERMS *(Continue on reverse if necessary and identify by block number)*

19. ABSTRACT *(Continue on reverse if necessary and identify by block number)*

For more than 20 years, experimenters have used the resistively-and-capacitively-shunted-junction (RCSJ) model to predict the dynamics of Josephson junctions. As the sample area decreases, two effects ignored in the model become relevant: First, the low impedance of the leads at high frequency (roughly 100 Ω) compared to the dc impedance of 1 GΩ), and second, quantum fluctuations of φ, the order parameter phase difference between the junction electrodes. We have observed dramatic evidence of the importance of both these effects. Keywords: Josephson junctions; Tunnel junctions; [illegible] (KR)

20. DISTRIBUTION / AVAILABILITY OF ABSTRACT
☐ UNCLASSIFIED/UNLIMITED ☐ SAME AS RPT. ☐ DTIC USERS

21. ABSTRACT SECURITY CLASSIFICATION
Unclassified

22a. NAME OF RESPONSIBLE INDIVIDUAL

22b. TELEPHONE *(Include Area Code)*

22c. OFFICE SYMBOL

DD Form 1473, JUN 86

Previous editions are obsolete.

SECURITY CLASSIFICATION OF THIS PAGE

Using electron beam lithography and dilution refrigeration, we have made samples as small as 0.04 μm^2 and measured their properties at temperatures from 20 mK to 6 K. The ratio of the charging energy $E_C \equiv e^2/2C$ to the Josephson coupling energy E_J varied from 0.01 to 6.

When $R_n < 1$ kΩ, and E_C/E_J is small, the devices act like the conventional ones of earlier investigations. As R_n and E_C/E_J increase, we observe striking new behavior. First, an anomalous resistance R_0 appears on the low-voltage branch of the still-hysteretic current-voltage characteristic (IVC), inconsistent with the RCSJ model, but allowed by a model that contains the leads.

Second, the retrapping current I_r attains a nonzero, plateau minimum as $T \to 0$, in contrast to the $e^{-\Delta/kT}$ dependence predicted by the RCSJ model. To explain this, we must add to the model both the leads and the onset of pair-breaking quasiparticle tunneling at $V = 2\Delta/e$. We present analog simulations and an analytic estimation procedure for I_r that agree quantitatively with the data.

A modified RCSJ model, incorporating the leads, but keeping the assumption of a classical phase, predicts that R_0 decreases at low temperature as $e^{-2E_J/kT}$. The measured $R_0(T)$ is nonzero and constant at low T due to quantum fluctuations. We obtain a good fit to the data by assuming that the leads limit the phase slip to 2π per escape from the potential well, but otherwise have no effect on the escape rate. At high temperatures, the escape rate is given by the Kramers intermediate-damping result, while as $T \to 0$, it crosses over to the prediction of MQT theory.

Finally, when a magnetic field is applied to the sample, decreasing E_J and increasing E_C/E_J, a new type of IVC appears. This IVC closely resembles those predicted by fully quantum mechanical theories of a junction with a quasiparticle tunneling shunt.

Accession For
NTIS GRA&I ☑
DTIC TAB ☐
Unannounced ☐
Justification

By
Distribution/
Availability Codes
Dist: A-1
Avail and/or Special

DTIC
COPY
INSPECTED
1

Office of Naval Research

Contract N00014-89-J-1023
Contract N00014-89-J-1565
National Sciences Foundation Grant DMR-89-12927

EFFECT OF LEADS AND QUANTUM FLUCTUATIONS IN SMALL SUPERCONDUCTING TUNNEL JUNCTIONS

by

Alan Thornton Johnson, Jr.

Technical Report No. 30

Reproduction in whole or in part is permitted for any purpose of the United States Government. Approved for public release; distribution unlimited.

August 1990

The research reported in this document was made possible through support extended the Division of Applied Sciences, Harvard University, by the Office of Naval Research, under Contracts N00014-89-J-1023, N00014-89-J-1565 and by the National Sciences Foundation Grant DMR-89-12927.

Division of Applied Sciences
Harvard University · Cambridge, Massachusetts

Abstract

For more than 20 years, experimenters have used the resistively-and-capacitively-shunted-junction (RCSJ) model to predict the dynamics of Josephson junctions. As the sample area decreases, two effects ignored in the model become relevant: first, the low impedance of the leads at high frequency (roughly 100 Ω, compared to the dc impedance of 1 GΩ), and second, quantum fluctuations of φ, the order parameter phase difference between the junction electrodes. We have observed dramatic evidence of the importance of both these effects.

Using electron beam lithography and dilution refrigeration, we have made samples as small as 0.04 μm^2 and measured their properties at temperatures from 20 mK to 6 K. The ratio of the charging energy $E_C \equiv e^2/2C$ to the Josephson coupling energy E_J varied from 0.01 to 6.

When $R_n < 1$ kΩ, and E_C/E_J is small, the devices act like the conventional ones of earlier investigations. As R_n and E_C/E_J increase, we observe striking new behavior. First, an anomalous resistance R_0 appears on the low-voltage branch of the still-hysteretic current-voltage characteristic (IVC), inconsistent with the RCSJ model, but allowed by a model that contains the leads.

Second, the retrapping current I_r attains a non-zero, plateau minimum as $T \rightarrow 0$, in contrast to the $e^{-\Delta/kT}$ dependence predicted by the RCSJ model. To explain this, we must add to the model both the leads and the onset of pair-breaking quasiparticle tunneling at $V = 2\Delta/e$. We present analog simulations and an analytic estimation procedure for I_r that agree quantitatively with the data.

A modified RCSJ model, incorporating the leads, but keeping the assumption of a classical phase, predicts that R_0 decreases at low temperature as $e^{-2E_J/kT}$. The measured $R_0(T)$ is non-zero and constant at low T due to quantum fluctuations. We obtain a good fit to the data by assuming that the leads limit the phase slip to 2π per escape from the potential well, but otherwise have no effect on the escape rate. At high temperatures, the escape rate is given by the Kramers intermediate-damping result, while as $T \rightarrow 0$, it crosses over to the prediction of MQT theory.

Finally, when a magnetic field is applied to the sample, decreasng E_J and increasing E_C/E_J, a new type of IVC appears, with features reminiscient of both the Coulomb blockade and the Josephson effect. This IVC closely resembles those predicted by fully quantum mechanical theories of a junction with a quasiparticle tunneling shunt.

Table of Contents

page

Abstract iii

List of Figures viii

List of Tables xi

Chapter One. Introduction 1

Chapter Two. The Quantum Mechanical Junction 11

- 2.1 Quantizing the junction Hamiltonian 11
- 2.2 Ohmic dissipation 14
- 2.3 A simple model 19
- 2.4 Quasiparticle tunneling dissipation 21
- 2.5 The choice of wavefunctions 27
- 2.6 Phase transitions in the quantum junction 28
- 2.7 Summary 34

Chapter Three. Experimental Techniques 35

- 3.1 Sample fabrication 35
  - 3.1.1 Contact pads 36
  - 3.1.2 Electron beam lithography: resist considerations 39
  - 3.1.3 Electron beam lithography: the EBL system 44
  - 3.1.4 Tin deposition 46
  - 3.1.5 Areas for future work 47
- 3.2 Measurement at dilution refrigerator temperatures 48
  - 3.2.1 Top-loading 49

3.2.2 Temperature measurement and control 51

3.2.3 Electrical set-up 53

Chapter Four. Experimental Results 54

4.1 Current-voltage characteristics (IVCs) 54

4.2 Junction characterization 59

4.2.1 The critical current I_c 59

4.2.2 The retrapping current I_r 61

4.2.3 The low-voltage branch resistance R_0 67

4.3 Effect of an applied magnetic field 70

4.3.1 Intermediate fields: novel IVCs 72

4.3.2 Intermediate fields and an applied ac signal 75

4.3.3 Large magnetic fields: N-I-N tunneling 77

4.4 Summary 87

Chapter Five. The RCSJ-plus-leads Model 89

5.1 The retrapping current 89

5.1.1 The retrapping current in the RCSJ model 90

5.1.2 The RCSJ-plus-leads model 96

5.2 R_0 105

5.2.1 The importance of $R_0 > 0$ 107

5.2.2 Numerical results 111

5.3 The critical current 117

5.4 Summary 123

Chapter Six. Conclusions and Suggestions for Future Work 124

References 131

Appendix: Sample Fabrication Procedures 136

Acknowledgements 140

List of Figures

page

Fig. 1.1 (a) Schematic of a Josepson junction 2

(b) Josephson potential 2

Fig. 1.2 Measured I-V curve, zero magnetic field 5

Fig. 1.3 $I_r(T)$, data and RCSJ prediction for the sample with $R_n = 1.1$ kΩ 6

Fig. 1.4 $R_0(T)$, data and classical theory for the sample with $R_n = 140$ kΩ 7

Fig. 1.5 Measured I-V curve, intermediate magnetic field 9

Fig. 2.1 (a) Bandstructure for $E_C << E_J$ 13

(b) Bandstructure for $E_C >> E_J$ 13

Fig. 2.2 Charge space transitions for a junction with an ohmic shunt 16

Fig. 2.3 Junction with an ohmic shunt: comparison of the I-V curves predicted by simple model and complete theory 18

Fig. 2.4 (a) Simple model of a junction with an ohmic shunt 20

(b) Charge space transitions for the simple model 20

Fig. 2.5 Charge space transitions for a junction with a quasiparticle tunneling shunt 22

Fig. 2.6 $T = 0$ theoretical I-V curves for junctions with different strength quasiparticle tunneling shunts 25

Fig. 2.7 Theoretical I-V curves for a junction with a quasiparticle shunt at different temperatures 26

Fig. 2.8 Diagram discussing the origin of the capacitance renormalization due to quasiparticle tunneling 30

Fig. 2.9 Sketch of energy bands distorted by quasiparticle tunneling 32

Fig. 2.10 Phase diagram for a junction with a quasiparticle shunt 33

Fig. 3.1 Lift-off with an undercut resist profile yields a smooth-edged film 37

Fig. 3.2 Sketch of the deep u-v contact printing chuck 40

Fig. 3.3 Outline of the evaporation procedure 41

Fig. 3.4 How a two-layer resist system produces an undercut profile 42

Fig. 3.5 Schematic of the electron beam lithography system 45

Fig. 3.6 Diagram of the top-loading slug 50

Fig. 4.1 Measured I-V curve for the sample with $R_n = 140$ kΩ 56

Fig. 4.2 Two I-V curves for the sample with $R_n = 140$ kΩ, with the same current axis, but different voltage axes 57

Fig. 4.3 $I_c(T)$ for seven samples 60

Fig. 4.4 $I_r(T)$ for four samples 62

Fig. 4.5 $I_c(T)$, $I_r(T)$, and theory for the sample with $R_n = 140$ kΩ 63

Fig. 4.6 (a) RCSJ model I-V curve in the absence of fluctuations 65

(b) RCSJ model I-V curve in the presence of large fluctuations 65

Fig. 4.7 $R_0(T)$ for seven samples 68

Fig. 4.8 $R_0(T)$ for the sample with $R_n = 140$ kΩ 69

Fig. 4.9 $I_c(H)$, data and theory for the sample with $R_n = 8.3$ kΩ 71

Fig. 4.10 Six I-V curves of the 140 kΩ sample at contant T and different magnetic fields 73

Fig. 4.11 A progression of I-V curves of the 140 kΩ sample at constant H and different T 74

Fig. 4.12 Series of I-V curves from the sample with $R_n = 21$ kΩ, at constant T and H, but different levels of applied 100 MHz power 76

Fig. 4.13 Series of I-V curves from the sample with $R_n = 26$ kΩ, at constant T and H, but different levels of applied 100 MHz power 78

Fig. 4.14 Series of I-V curves from the sample with R_n = 21 kΩ, at constant T and H, but different levels of applied 800 MHz power 79

Fig. 4.15 I-V curve and its derivative for the sample with R_n = 140 kΩ, driven normal by a large magnetic field 81

Fig. 4.16 Gap voltage versus magnetic field for the sample with R_n = 8.3 kΩ 82

Fig. 4.17 dV/dI vs. V for the 140 kΩ sample in various magnetic fields 84

Fig. 4.18 dV/dI vs. V for the 74 kΩ sample in two magnetic fields 85

Fig. 4.19 Diagram of the multi-junction sample used to obtain the data in Fig. 4.18. 86

Fig. 5.1 (a) The RCSJ model 91

(b) The washboard potential 91

Fig. 5.2 Comparison of the quasiparticle I-V curve with R_L and the theory of Chen, et al. (1988) 93

Fig. 5.3 $I_r(T)$ for three samples and two theories for one of the samples 95

Fig. 5.4 $I_r(T)$, data and 4 theories for the sample with R_n = 1.1 kΩ 97

Fig. 5.5 The two-frequency RCSJ-plus-leads model 101

Fig. 5.6 Simulated I_{r0} versus shunt resistance for a junction with low-impedance leads 103

Fig. 5.7 Comparison of $I_r(T)$ for the R_n=8.3 kΩ sample with an analytic estimate and analog simulation 104

Fig. 5.8 (a) The Josephson potential with $I_{r0} < I < I_{c0}$ 108

(b) Phase space for the Josephson system, showing the running state attractor and basins of attraction for two trapped states 108

Fig. 5.9 Three commonly used models for the junction leads 109

Fig. 5.10 The Josephson potential with $I << I_{c0}$ 112

Fig. 5.11 $R_0(T)$, data and theory, for the sample with R_n = 520 Ω 114

Fig. 5.12 $R_0(T)$, data and classical theory, for the samples with R_n = 14.8 kΩ and 140 kΩ 115

Fig. 5.13 Comparison of $R_0(T)$ for the R_n = 14.8 kΩ sample with a theory including both thermal activation and quantum tunneling 116

Fig. 5.14 $R_0(T)$ for the R_n = 14.8 kΩ sample in a 600 G magnetic field 118

Fig. 5.15 I_c/I_{c0} vs. R_0 for four junctions from this work and samples of other authors 121

Fig. 6.1 The quantum metrological triangle 129

List of Tables

Table 4.1 Parameters for various samples 55

Table 5.1 Comparison of measured and calculated I_r^{min} for three samples 106

Chapter One

Introduction

The Copenhagen interpretation asserts that *all* phenomena are intrinsically quantum mechanical. According to Bohr's correspondence principle, classical mechanics, which predicts accurately the behavior of large objects (bowling balls, pendula, etc.) may in principle be derived from quantum mechanics, in a suitable approximation. We understand the classical mechanics of macroscopic objects, and can calculate their motion with extraordinary precision. The same is true of the quantum mechanics of microscopic entities, such as atoms, electrons and simple molecules. The details of the transition between these two regimes, the physics of so-called *mesoscopic* systems, remains largely unexplored, and is the subject of intense experimental and theoretical effort.

Solid state physics provides an abundance of examples of this research. Quantum conductance fluctuations, unique to each sample, result from the interference of time-reversed electronic Feynman paths in small metal wires and semiconducting devices [Smith, 1989]; they disappear in large samples, as the interference effects average to zero. As a second example, quantized conductance levels have been observed in the transport of ballistic carriers through short channels with width of order the Fermi wavelength [van Wees, et al., 1988]. We have tried to investigate the crossover from classical to quantum mechanics through an experimental study of mesoscopic superconducting tunnel junctions.

Also known as a Josephson junction, this device, made of two superconductors separated by an insulating barrier (see Fig. 1.1), has been an active research subject since Josephson's prediction of Cooper pair tunneling [1962]. In the RCSJ model [McCumber, 1968], the current flows through three channels: the Josephson (supercurrent) channel, the capacitance C formed by the junction's parallel plate structure, and the quasiparticle tunneling channel with normal resistance R_n [Giaever, 1960]. Current conservation yields an equation of motion for φ, the phase difference between the collective superconducting

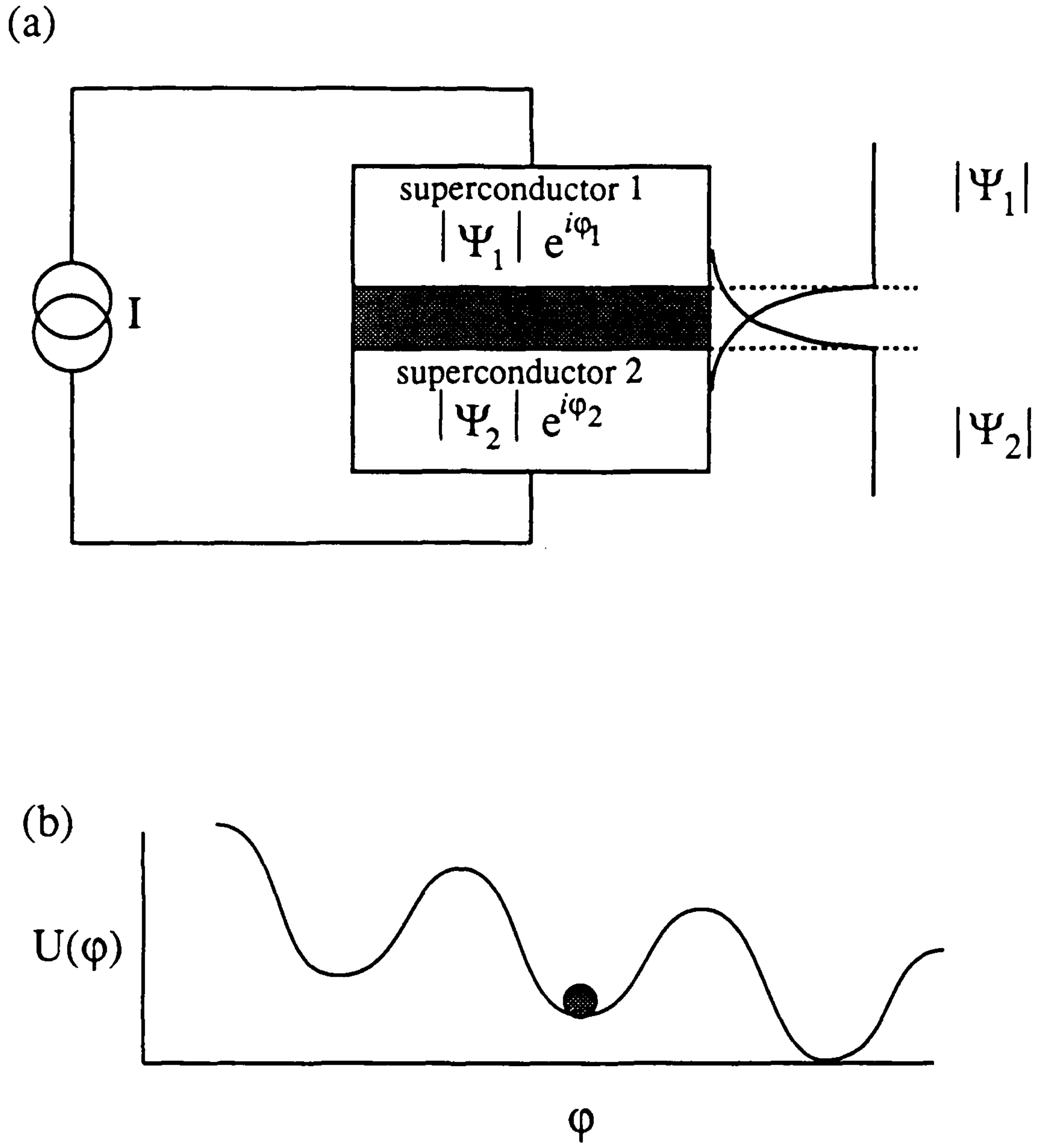
(a)
superconductor 1
|Ψ1| e^iφ1
I
superconductor 2
|Ψ2| e^iφ2
|Ψ1|
|Ψ2|
(b)
U(φ)
φ

Fig. 1.1: (a) Josephson junction schematic. Overlap of the superconducting wavefunctions allows Cooper pair tunneling. (b) the Josephson potential, $U(\varphi) = -E_J\cos\varphi - \hbar I\varphi/2e$.

wavefunctions of the two electrodes. The motion is that of a classical particle (whose position and velocity are sharp variables) with mass proportional to C, damped by a fluid of viscosity scaling as $1/R_n$, moving in a cosinusoidal potential with amplitude $E_J = h\Delta/8e^2R_n$, Δ being the superconducting energy gap. This model is an outstandingly successful description of the dynamics of conventional junctions with $E_J >> E_C$. $E_C \equiv e^2/2C$ is the energy due to a single-electron charge difference across the capacitor.

As we reduce the junction area A, E_J ($\propto A$) decreases, while E_C ($\propto A^{-1}$) becomes larger. Ignoring damping[‡], the system's Lagrangian is:

$$L = \frac{C}{2}\left(\frac{\hbar\dot{\varphi}}{2e}\right)^2 + E_J \cos\varphi \ . \tag{1.1}$$

The canonical momentum of φ is $p_\varphi = (\hbar/2e)^2 C\dot{\varphi}$. Localizing φ to one potential well ($\Delta\varphi = 2\pi$) leads to a momentum uncertainty $\Delta p_\varphi \approx \hbar$, as required by Heisenberg's principle. The kinetic energy, therefore, has fluctuations of magnitude $\Delta K.E.$, given by:

$$\Delta K.E. = \frac{(\Delta p_\varphi)^2}{2C}\left(\frac{2e}{\hbar}\right)^2 \approx \frac{2e^2}{C} = 4E_C \ . \tag{1.2}$$

If $\Delta K.E.$ exceeds E_J, the energy barrier to phase motion, the classical model breaks down. We routinely make Sn-SnOx-Sn junctions with $A = 0.04\ \mu\text{m}^2$ and $C = 1\text{-}2$ fF. Since

$$E_C / k = \frac{e^2}{2Ck} \cong \frac{1}{C\,[\text{fF}]}\ \text{K, and}\ E_J / k = \frac{h\Delta}{8e^2R_nk} \cong \frac{11}{R_n\,[\text{k}\Omega]}\ \text{K}, \tag{1.3}$$

we expect to observe the inadequacy of the classical picture in samples with $R_n > 10\ \text{k}\Omega$.

[‡] The effect of damping is to *reduce* the quantum fluctuations of φ [Caldeira and Leggett, 1981]. Our calculation, therefore, is only indicative of the *potential* for breakdown of the classical model.

A second assumption of the RCSJ model also fails as the sample area decreases. When R_n is large, it is no longer possible to ignore high-frequency current flow through the leads attached to the sample. Modern amplifier technology allows the lead impedance to be ~1 GΩ at dc. At frequencies above a few hundred MHz, however, transmission line effects reduce the impedance to 50-100 Ω. If R_n and $1/\omega C$ are much larger than this value, nearly all the high-frequency current flows through the leads. In this work, we have observed dramatic evidence of the importance of both quantum fluctuations and the presence of the leads.

The samples used in this investigaion had R_n ranging from 500 Ω to 140 kΩ. The ratio E_C/E_J varied from about 0.01 to 6. We increased E_C/E_J further by applying a dc magnetic field to the sample, which reduces E_J.

When $E_J >> E_C$, our samples behave like the conventional junctions of earlier investigations [Danchi, 1983]. As E_C/E_J increases, we observe striking new behavior. The I-V characteristic (IVC) is still hysteretic, but the critical current is greatly reduced, and there is an anomalous resistance R_0 on the low voltage branch (see Fig. 1.2). The combination of hysteresis and $R_0 > 0$ is absolutely inconsistent with the RCSJ model. Secondly, the retrapping current I_r (defined in Fig. 1.2) attains a non-zero, temperature independent value as $T \rightarrow 0$, pictured in Fig. 1.3, in contrast to the exponentially vanishing $I_r(T)$ predicted by the RCSJ model. Both of these new properties derive from the low impedance presented by the leads at high frequency; to explain the latter we also must invoke the existence of pair-breaking quasiparticle tunneling for $V \geq 2\Delta/e$.

If we take the leads into account, but continue to assume that φ is classical, we expect $R_0(T)$ to decrease at low temperature as the Boltzmann factor $e^{-2E_J/kT}$. In Fig. 1.4, we see, however, that our measured $R_0(T)$ is constant at low temperature, due to the effect of quantum mechanical phase fluctuations, described by the theory of macroscopic quantum tunneling [Caldeira and Leggett, 1981; Iansiti, 1988].

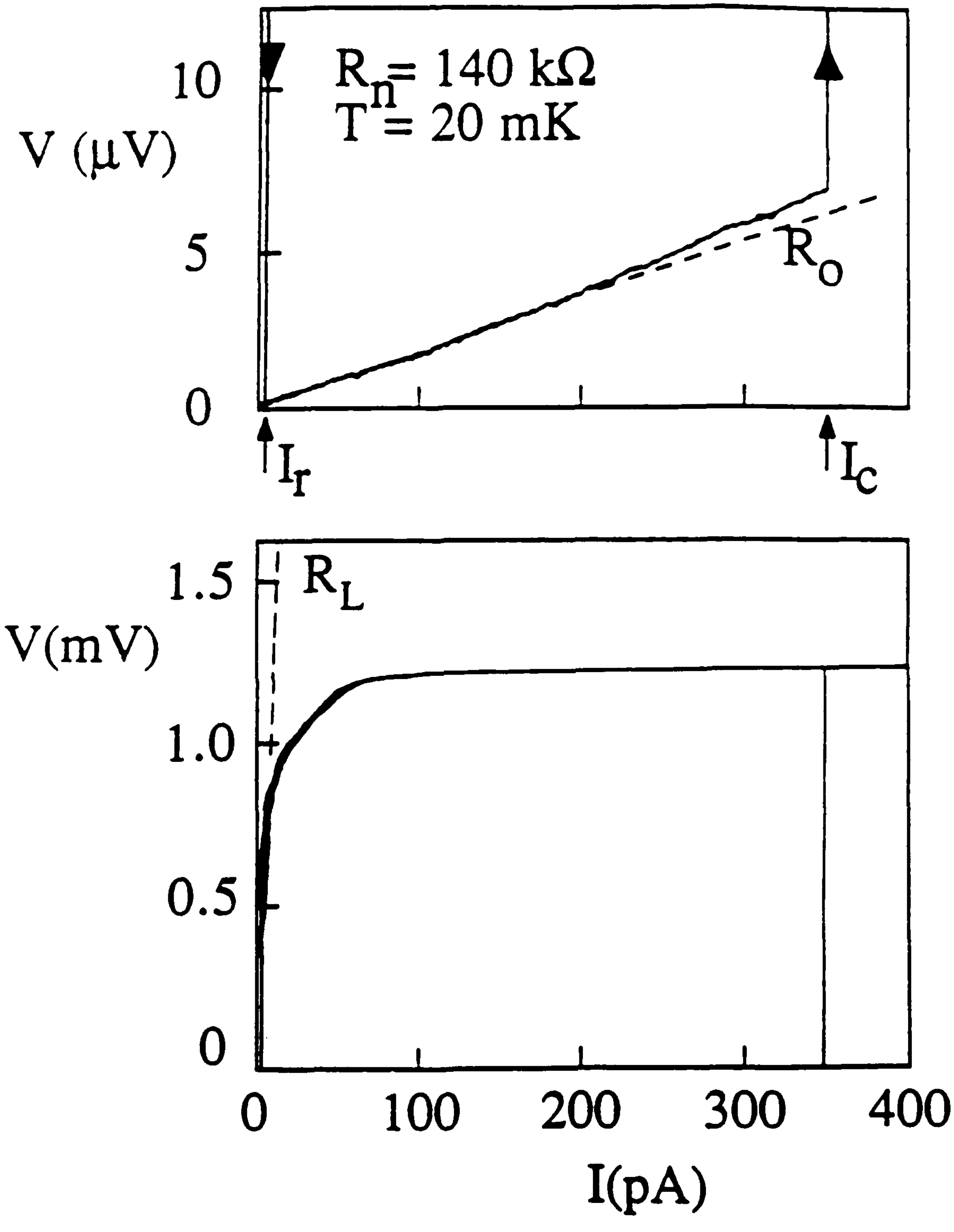

Fig. 1.2: Two IVCs for the R_n = 140 kΩ sample, with the same current axis, but differing voltage axes. The top voltage axis is expanded 100 times relative to the bottom, revealing the anomalous low-voltage resistance. I_c, I_r, R_O, and R_L are defined.

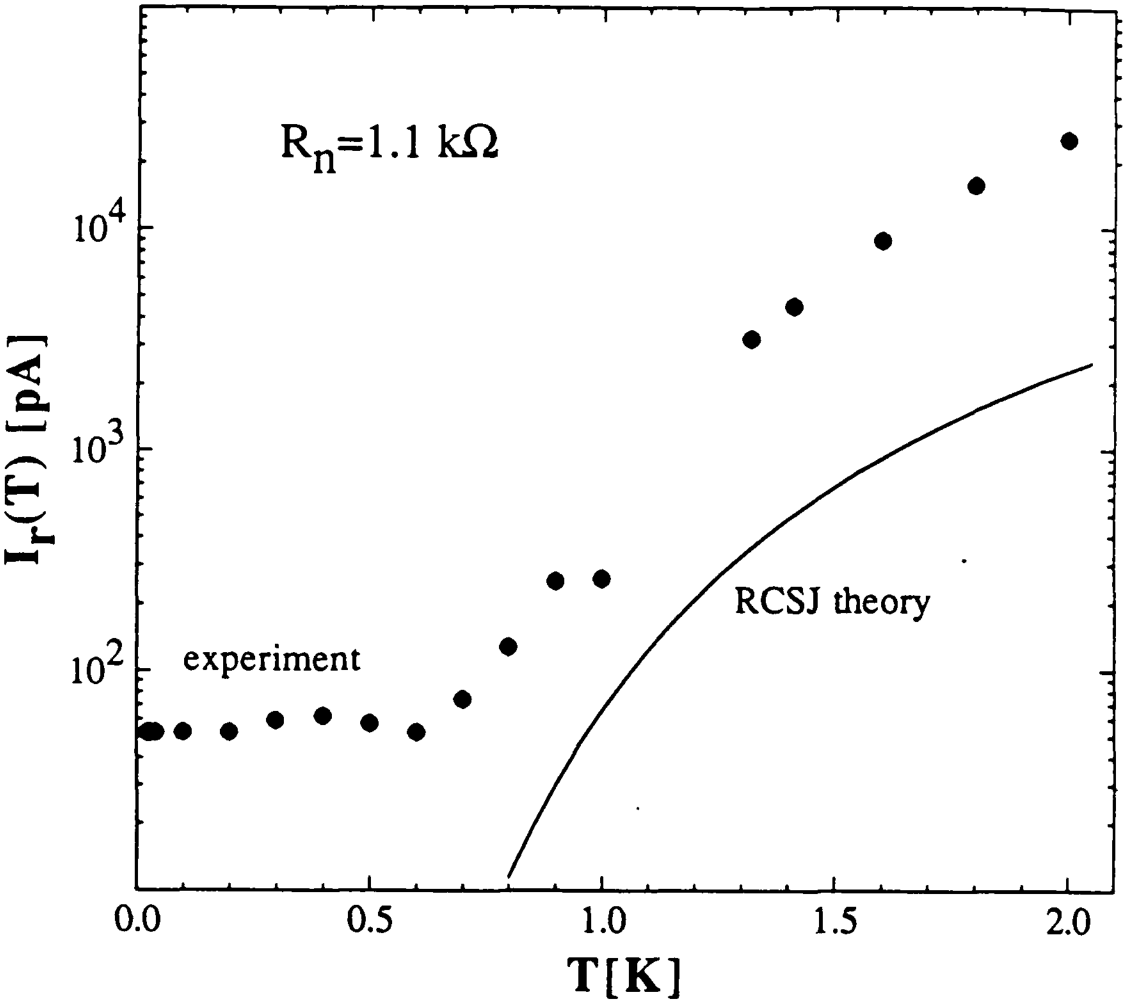

Fig. 1.3: $I_r(T)$, data and theory, for the sample with $R_n = 1.1$ kΩ. The data level off at low temperature, in contrast to RCSJ model prediction that I_r vanishes exponentially.

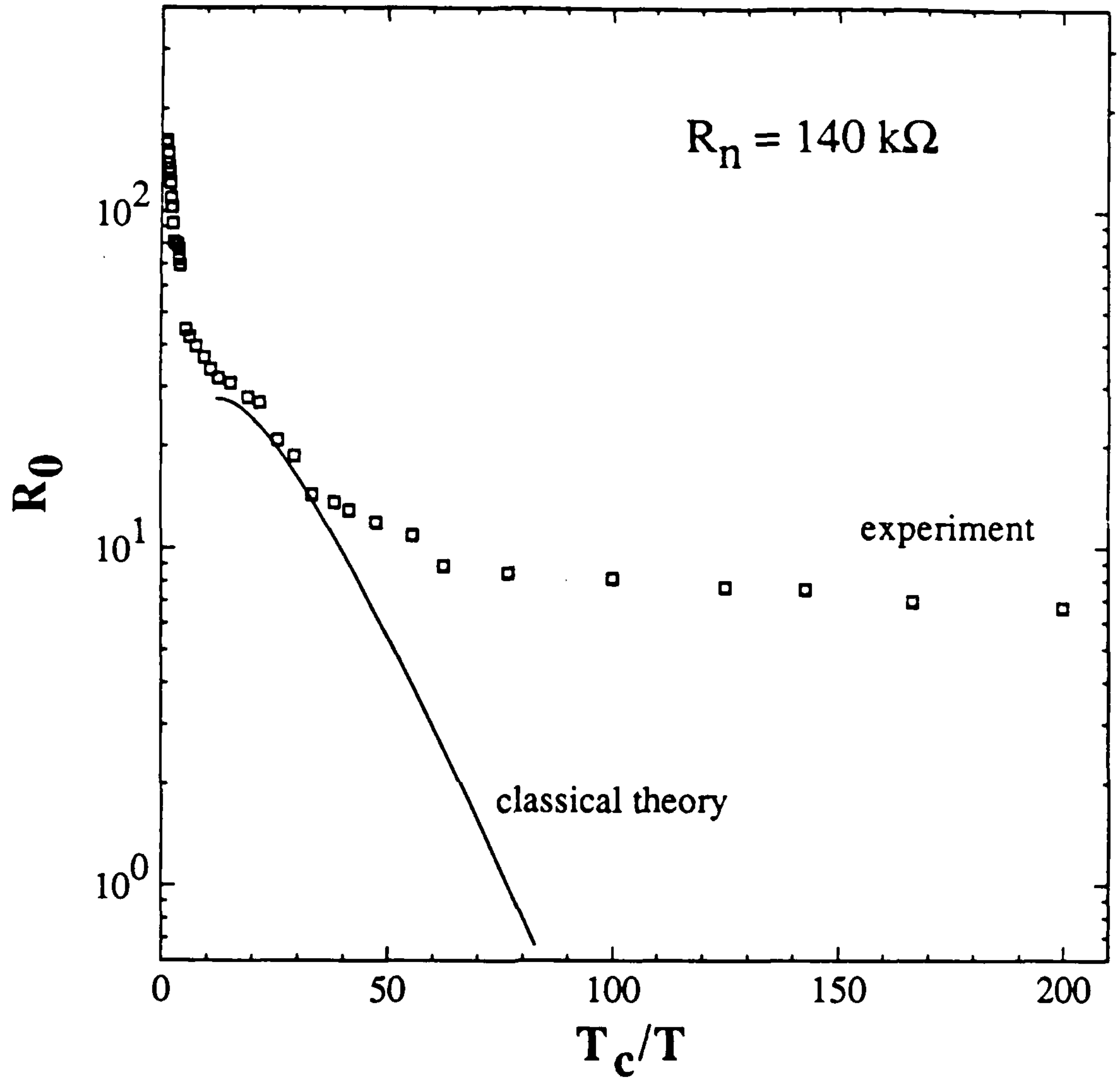

Fig. 1.4: R_0 vs. T_c/T, data and theory, for the sample with R_n = 140 kΩ. The data level off for large T_c/T, in contrast to classical prediction that R_0 vanishes exponentially.

When we reduce the Josephson coupling energy even further with a magnetic field, a new type of hysteretic IVC appears (Fig. 1.5). The voltage $V(I)$ increases rapidly for small currents, and then rolls over to a plateau at a voltage $V \approx e/2C$. There is a critical current I_c, at which the voltage rises discontinuously to $V = 2\Delta/e$. The IVC bears a strong resemblance to those predicted by fully quantum mechanical theories of φ.

In this report, we present our observations and their interpretation. Chapter Two is a discussion of the quantum theory of the Josephson junction. The theory of φ is qualitatively similar to that of an electron in a periodic crystal potential. We emphasize measurable predictions of this theory, in particular the shape of the IVC. We also describe the $T = 0$ phase transition predicted to occur as a function of R_n in Josephson junctions with quasiparticle tunneling dissipation.

In Chapter Three, we describe the experimental methods used in this work, concentrating on the technical advances which were crucial to its success: electron beam lithography and dilution refrigeration. The Technical Reports of Marco Iansiti [1988] and Walter F. Smith [1989] contain additional information about these two important resources.

Chapter Four is a summary of the data, along with preliminary interpretation. Our main probe of the junction's physics is the IVC and the derived quantities I_c, I_r, and R_0. We show IVCs in zero magnetic field, in intermediate field as the step-like feature of Fig. 1.5 develops, and in fields large enough to drive the junction normal. In the latter case, the data agree well with theories of N-I-N tunneling in the large charging energy limit.

With the data in hand, we present the major results of the "RCSJ-plus-line" model in Chapter Five. In this new model, we include the frequency-dependent impedance of the leads. As mentioned above, this accounts for the existence of $R_0 > 0$, as well as the non-zero minimum plateau of $I_r(T)$ as $T \to 0$. We develop a heuristic "two-frequency" model of the junction and the leads, which yields simple methods to predict I_r and I_c for a junction *without* the need for complex computer simulation. These predictions agree with our data, as well as that from other groups.

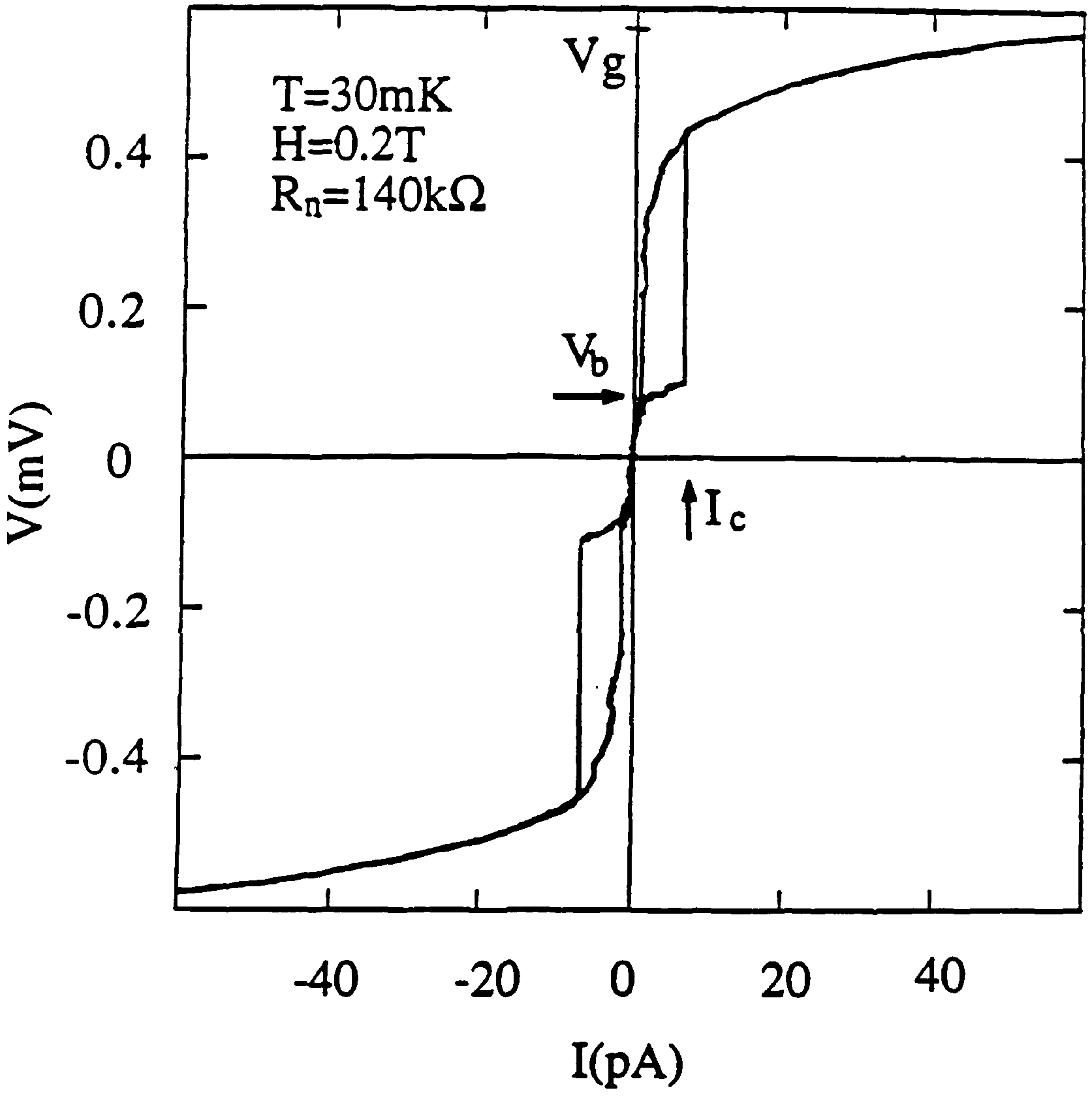

Fig. 1.5: An applied magnetic field reduces E_J, producing a new type of hysteretic IVC. The sample parameters are R_n = 140 kΩ, C = 1 fF, T = 30 mK, and H = 0.2 T. The voltage plateau occurs at V_b = 90±20 μV, while $e/2C$ = 80 μV.

Finally, we summarize our results and provide suggestions for future research in Chapter Six.

Chapter Two

The Quantum Mechanical Junction‡

In this chapter, we summarize the results of the quantum mechanical theory of a superconducting tunnel junction. We concentrate on predictions of measured quantities, specifically I-V characteristics (IVCs), which may be compared with experiment.

2.1 Quantizing the junction Hamiltonian

As discussed earlier, when $E_J << E_C$, it is possible that the classical junction model has broken down, and quantum fluctuations of the phase are significant. Consider first an isolated junction. As is the usual practice in quantum mechanics, we take the classical Hamiltonian and assume an appropriate commutator between the coordinate and its canonical momentum. This leads to

$$H = \frac{Q^2}{2C} - E_J \cos\varphi \ , \tag{2.1}$$

where $Q = (2e/i)\, d/d\varphi$. The complementarity principle between Q and φ is well known from BCS theory [Tinkham, 1975, p. 24]. An important and delicate question arises concerning proper boundary conditions for the problem, a point we address in section 2.5.

Ignoring this complication for the moment and assuming that φ is an extended variable, this Hamiltonian is familiar from solid state theory, admitting Bloch state eigenfunctions, $\psi(\varphi) = e^{iq\varphi/2e}u_q(\varphi)$, where $u_q(\varphi) = u_q(\varphi+2\pi)$. $E_n(q)$ is a band structure with period $2e$; the two limits of "tight-binding" ($E_J >> E_C \equiv e^2/2C$) and "nearly-free" ($E_J << E_C$) bands are portrayed in Fig. 2.1. In the former case, the low lying bands are nearly flat, made up of barely interacting harmonic oscillator states. The lowest band has width [Schön and Zaikin, preprint]

---

‡ The number of contributors to the understanding of this problem and papers they have produced precludes a complete accounting of the originator of each important idea. The work of K. K. Likharev deserves special mention, however, and we take the opportunity to do so here.

$$\Delta_0 = 16\left(\frac{E_J E_C}{\pi}\right)^{1/2}\left(\frac{E_J}{2E_C}\right)^{1/4} \exp\left\{-8\left(\frac{E_J}{E_C}\right)^{1/2}\right\} . \tag{2.2}$$

The first bandgap is $\hbar\omega_p$, and it remains at this value for all bands with $E_n << E_J$. In the nearly-free limit, the bands are parabolic ($E(q) \approx q^2/2C$) except near $q = e$, the edge of the Brillouin zone; the width of the lowest band is about $e^2/2C$, and the first bandgap has magnitude E_J, while the higher ones decrease rapidly. We call q the "quasicharge" (analogous to the crystal momentum in the band theory of solids), to differentiate it from the real charge across the junction, $<Q> = C<V> = CdE_n(q)/dq$.

The Hamiltonian for φ (2.1) is analogous to that of an electron in a one-dimensional, periodic crystal potential [Ashcroft and Mermin, 1976, Chapter 12]. In this related problem, an electric field E, which corresponds to a force in a classical treatment, causes the crystal momentum to evolve: $dk/dt = eE/\hbar$. Similarly, adding a current bias to (2.1), which would be a force (washboard tilt) in the classical limit, leads to an equation of motion for the quasicharge, $dq/dt = I$. We therefore associate q with the "external" charge, the charge supplied to the junction by an ideal current source $\{q = \int^t dt' I(t')\}$ or the charge polarization created by an external field [Büttiker, 1987].

To make this identification more obvious, consider the following Hamiltonian:

$$H = \frac{(Q+Q_x)^2}{2C} - E_J \cos\varphi \ , \tag{2.3}$$

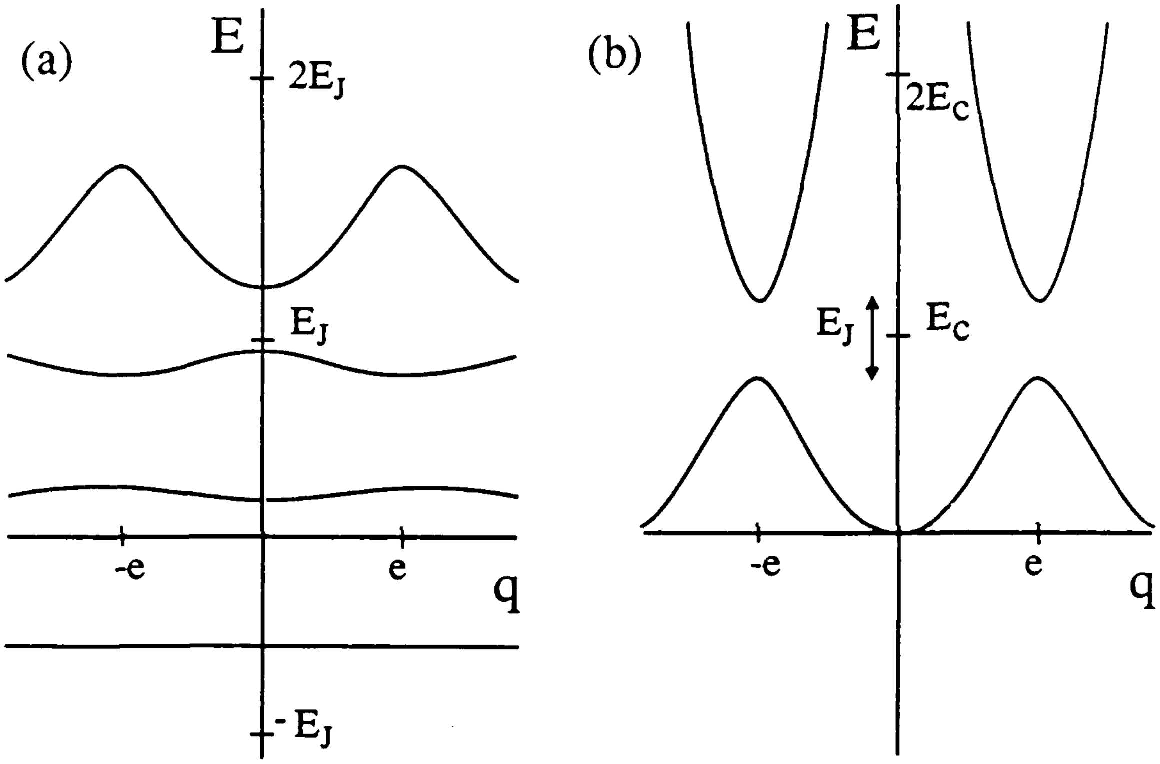

Fig. 2.1: Bandstructure for the Hamiltonian (2.1) with (a) $E_C/E_J = 0.1$, and (b) $E_C/E_J = 2.5$. These bandstructures are typical for junctions in the tight-binding and nearly-free limits, respectively.

where $Q = (2e/i)\, d/d\varphi$. We take Q_x to be a c-number, and only 2π-periodic states $\psi_n(\varphi)$ are allowed. The solutions to (2.3) are related to those of (2.1) by a gauge transformation, and here Q_x is clearly the external charge. The total charge across the junction is the sum of the external charge and the charge due to the junction response.

When Q_x changes adiabatically (i.e. no interband transitions), the system dynamics are simple. If the system begins in a given band, it remains in that band for all time. Charge accumulates on the junction until $Q_x = e$; at this point a Cooper pair tunnels across the junction. If $dQ_x/dt = I$ is a constant, there will be a series of charging and discharging events with frequency $f = I/2e$. These are known as "Bloch oscillations," because of their relation to the like-named phenomenon in solid state physics [Likharev and Zorin, 1985].

2.2 Ohmic dissipation

Weak dissipation may be included in this picture in a simple manner. For the moment, consider a linear shunt resistor R_s. In section 2.4, we present the case of a quasiparticle shunt with subgap resistance R_T, a more realistic scenario for our samples. If $R_s >> \hbar/e^2$ ($\approx$ 4.1 kΩ), we may use a perturbation treatment. The shunt provides a channel for charge flow as well as fluctuations. If the system begins in a state $\psi_n(Q_{x0})$, $Q_x(t)$ is governed by the Langevin equation,

$$\frac{dQ_x}{dt} = I(t) - \frac{V_n}{R_s} + I_n(t)\ , \tag{2.4}$$

The expectation value of the voltage in the state $\psi_n(Q_x)$ is $\langle V_n \rangle = dE(Q_x)/dQ_x$. $I_n(t)$ is the noise current associated with R_s, with power spectrum

$$S_I(\omega) = \frac{1}{2\pi}\int dte^{i\omega t}\langle I_n(t)I_n(0)\rangle = \frac{\hbar\omega}{2\pi R_s}\mathrm{ctnh}\frac{\hbar\omega}{2kT} \tag{2.5}$$

as required by the fluctuation-dissipation theorem.

The applied current I encourages a uniform evolution in Q_x, which is resisted by R_s. The noise current causes Q_x to diffuse within one band and also admits interband transitions that conserve Q_x (see Fig. 2.2). The transition rate is [Likharev and Zorin, 1985]:

$$\Gamma^s_{n,n'}(Q_x) = \frac{\Delta E_{n,n'}(Q_x)}{4e^2 R_s}\left|\varphi_{n,n'}(Q_x)\right|^2\left\{\exp\left(\frac{\Delta E_{n,n'}(Q_x)}{kT}\right)-1\right\}^{-1}, \tag{2.6}$$

where $\varphi_{n,n'} = <\psi_{n'}(Q_x) \mid \varphi \mid \psi_n(Q_x)>$ is an overlap integral, and $\Delta E_{n,n'}(Q_x) = E_{n'}(Q_x)-E_n(Q_x)$ is the energy difference between the initial and final states. Zener tunneling [Zener, 1934] may be included with a certain likelihood at each Q_x which, when integrated, yields the usual Zener tunneling result:

$$P^Z_{n-1\leftrightarrow n} = \exp\left[-\frac{\pi e E_g^2}{8\hbar n E_C I_x}\right] \tag{2.7}$$

per Brillouin zone boundary traversal [Averin and Likharev, 1987]. In (2.7) E_g is the interband energy gap (assumed small). It is convenient to define the Zener-breakdown current $I_Z = \pi e E_g^2/8\hbar E_C$, the current at which Zener tunneling through the first bandgap has probability $1/e$.

We obtain I-V curves (IVC) by simulating (2.4). The system is described by a master equation for $\sigma_n(Q_x,t)$, the probability that at time t the system is in the state $\psi_n(Q_x)$ [Likharev and Zorin, 1985]:

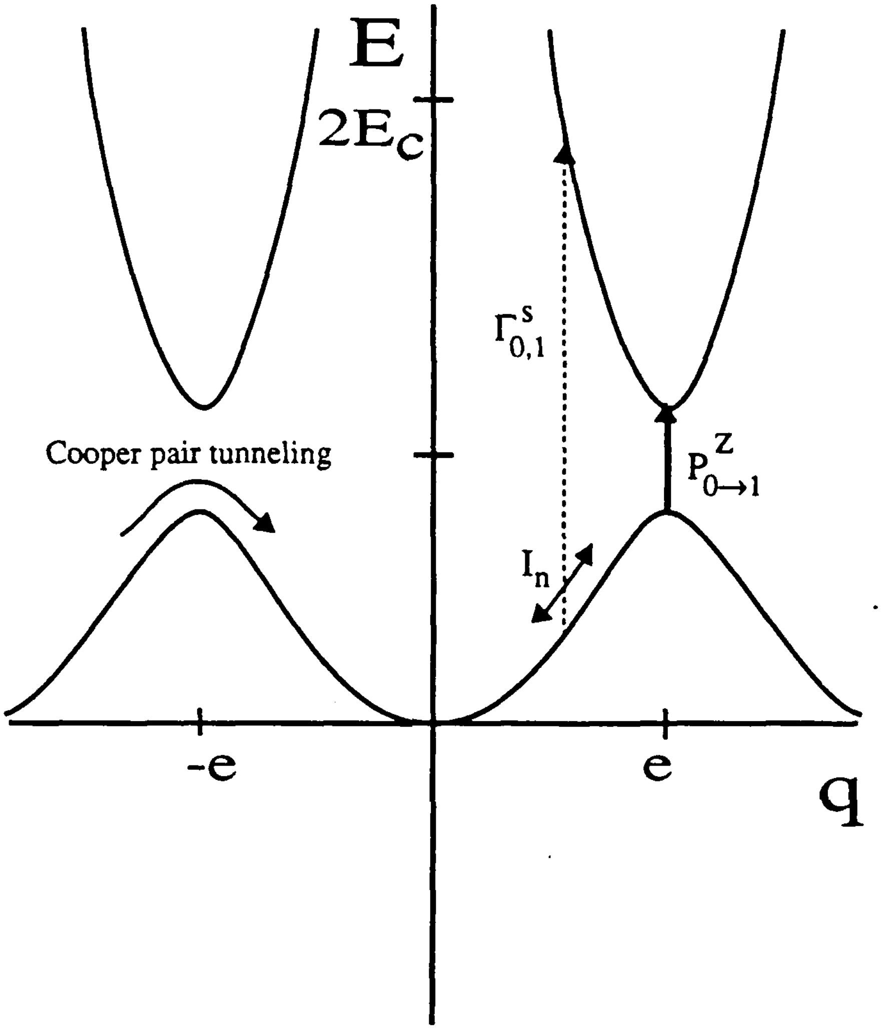

Fig. 2.2: A diagram of the bandstructure of a junction with $E_C >> E_J$ and an ohmic shunt showing allowed transitions in q-space. Crossing the zone edge corresponds to the transfer of a Cooper pair across the junction. At the zone edge, there also exists the possibility of Zener tunneling to the next higher or lower band ($P^{Z}_{0\to 1}$). Current fluctuations due to the shunt resistor cause diffusion within one band (indicated by the solid diagonal arrow near q = e/2), as well as transitions to higher (or lower) bands that conserve q (the dotted arrow labelled $\Gamma^{s}_{0,1}$). Adapted from Schön and Zaikin [preprint].

$$\frac{\partial \sigma_n(Q_x)}{\partial t} = -I\frac{\partial \sigma_n}{\partial Q_x} + \frac{1}{R_s}\frac{\partial(\sigma_n V_n)}{\partial Q_x} + \frac{kT}{R_s}\frac{\partial^2 \sigma_n}{\partial Q_x^2} \tag{2.8}$$

$$- \sum_{n'=0}^{\infty}\left\{\left[\Gamma^Z_{n,n'}(Q_x) + \Gamma^s_{n,n'}(Q_x)\right]\sigma_n(Q_x) - \left[\Gamma^Z_{n',n}(Q_x) + \Gamma^s_{n',n}(Q_x)\right]\sigma_{n'}(Q_x)\right\}$$

In (2.8) the first three terms on the r.h.s. account for the applied current, current flow through the shunt resistor, and intraband diffusion due to Johnson noise, respectively. The terms within the summation represent interband transitions, with the term containing the factor $\sigma_n(Q_x)$ accounting for transitions out of band n, and the other term for transitions into band n. The voltage is calculated using $<V(I)> = \sum V_n(Q)\sigma_n(Q)$, once an equilibrium form for $\sigma_n(Q,t)$ is reached.

This procedure will be inadequate if the properties of a single sample realization differ radically from those of the ensemble average. For example, an approach in this spirit would give a poor description of a classical, underdamped, RCSJ-model Josephson junction under the influence of thermal fluctuations. On any single current sweep up from zero, the junction switches from a $V = 0$ state to a $V > 0$ state at a stochastically reduced critical current [Fulton and Dunkleberger, 1974], while the ensemble average has a smoothly increasing $V > 0$ for all $I > 0$.

In Fig. 2.3 we show an IVC from a simulation of a junction with linear shunt resistor R_s and $E_C >> E_J >> kT$. There are two different regimes (labeled I and II) that persist through the variety of models that have been proposed for these samples.

Regime I occurs near the origin and is characterized by large $dV/dI = R_s$. Ignoring the noise term in (2.4), we see that if $V(Q_x) = IR_s$, then $dQ_x/dt = 0$, so that all the current flow is through R_s. The maximum current consistent with this configuration is $I_{max} = V_{max}/R_s$, where V_{max} is the maximum slope of $E(Q)$ for the first band, so that [Schön and Zaikin, preprint]:

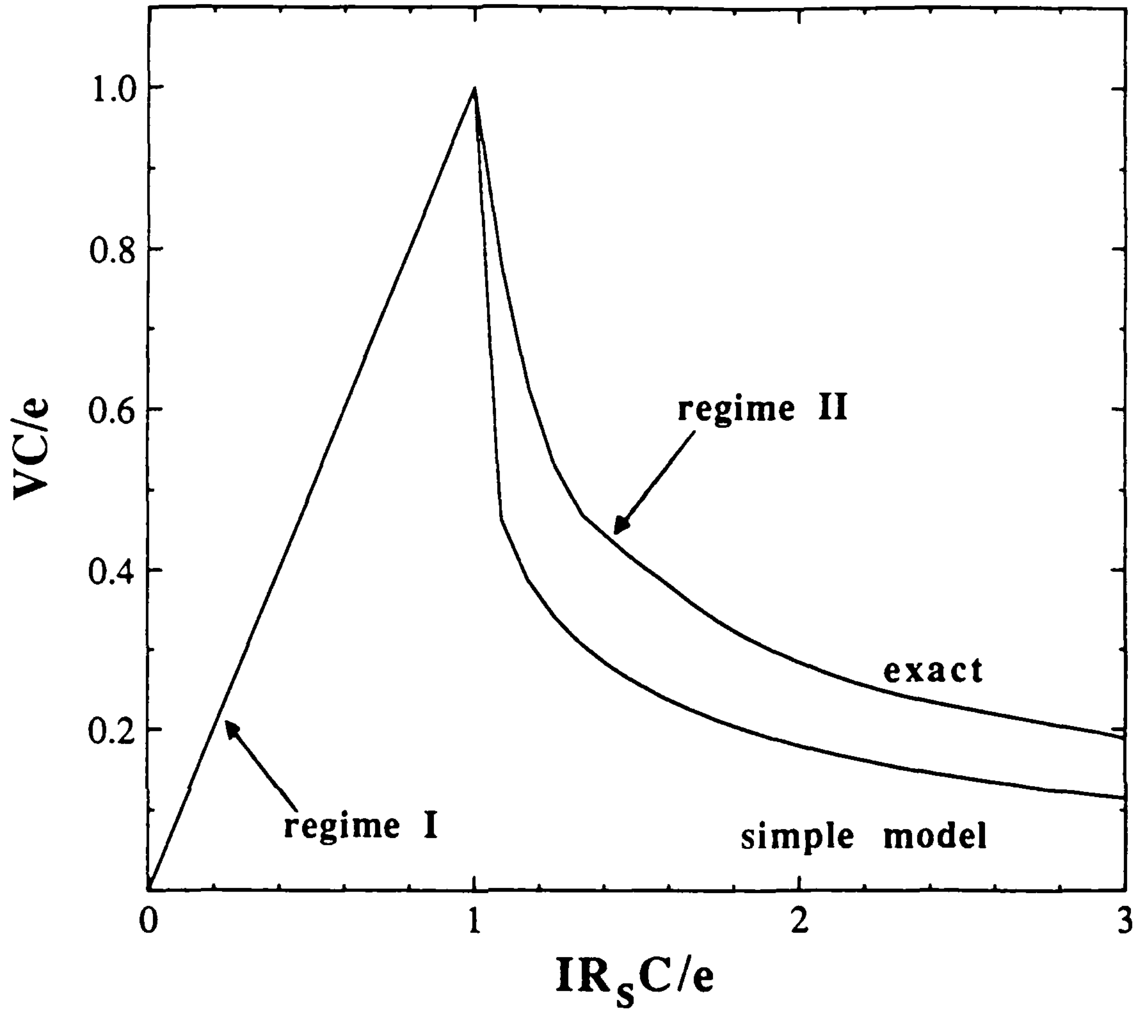

Fig. 2.3: IVCs for a junction with $E_C >> E_J$ and an ohmic shunt R_s, ignoring Zener tunneling. In regime I ($0 < I < e/R_sC$), $V = IR_s$. If we ignore Zener tunneling, as I increases from e/R_sC, more and more of the current is carried by Cooper pairs, so the voltage decreases monotonically (regime II). We show here the exact IVC (from Schön and Zaikin [1990]) and the IVC predicted by our simple model (section 2.3). The two differ because the simple model ignores the deviation of the lowest band from parabolic shape at the band edge.

$$I_{max} = \begin{cases} e / R_s C & \text{for } E_J << E_C \\ \pi\Delta_0 / eR_s & \text{for } E_J >> E_C \end{cases} \tag{2.9}$$

where Δ_0, defined in (2.2), is the width of the first band in the tight-binding limit.

In regime II ($I > I_{max}$), no static solution is possible, and Q_x cycles through the Brillouin zone. If we ignore interband transitions (a good approximation when $I << I_Z$ and R_s is large), this region has a negative differential resistance. At the zone edge, a Cooper pair is transfered, and Q_x goes from e to $-e$ and then begins to grow again. This current range is, therefore, host to Bloch oscillations. The voltage now varies in time through both positive and negative values, so that the time-averaged voltage is much less than in the static regime I. Finally at large currents (not shown in Fig. 2.3), Zener tunneling becomes common. The system is driven to higher bands, resulting in a large voltage.

2.3 A simple model

We now discuss a simple model that reproduces some of the qualitative features of the picture detailed above (see Fig. 2.4). We approximate the junction as an ordinary resistor R_s, shunted by a capacitor C and a Josephson channel which instantaneously transfers charge $2e$ whenever doing so reduces the system energy $U(Q) = Q^2/2C$, where Q is the charge on the capacitor, that is, whenever $|Q| = e$. This model should be most applicable in the limit $E_J << E_C$ and $T = 0$.

For currents $0 \leq I < I_{th} = e/R_sC$, all the current flows through R_s, and the charge on the capacitor is $Q = CV = IR_sC < e$. Cooper pairs cannot tunnel, since a $2e$ transfer would increase $U(Q)$. The IVC is linear with slope R_s; this corresponds to region I discussed above. When I exceeds I_{max}, the capacitor charges and discharges periodically. The average voltage is reduced from IR_s, since for some times $Q(t)$, and therefore $V(t)$, is negative. Simple calculations yield the oscillation frequency and $V(I) = \langle V(t) \rangle$:

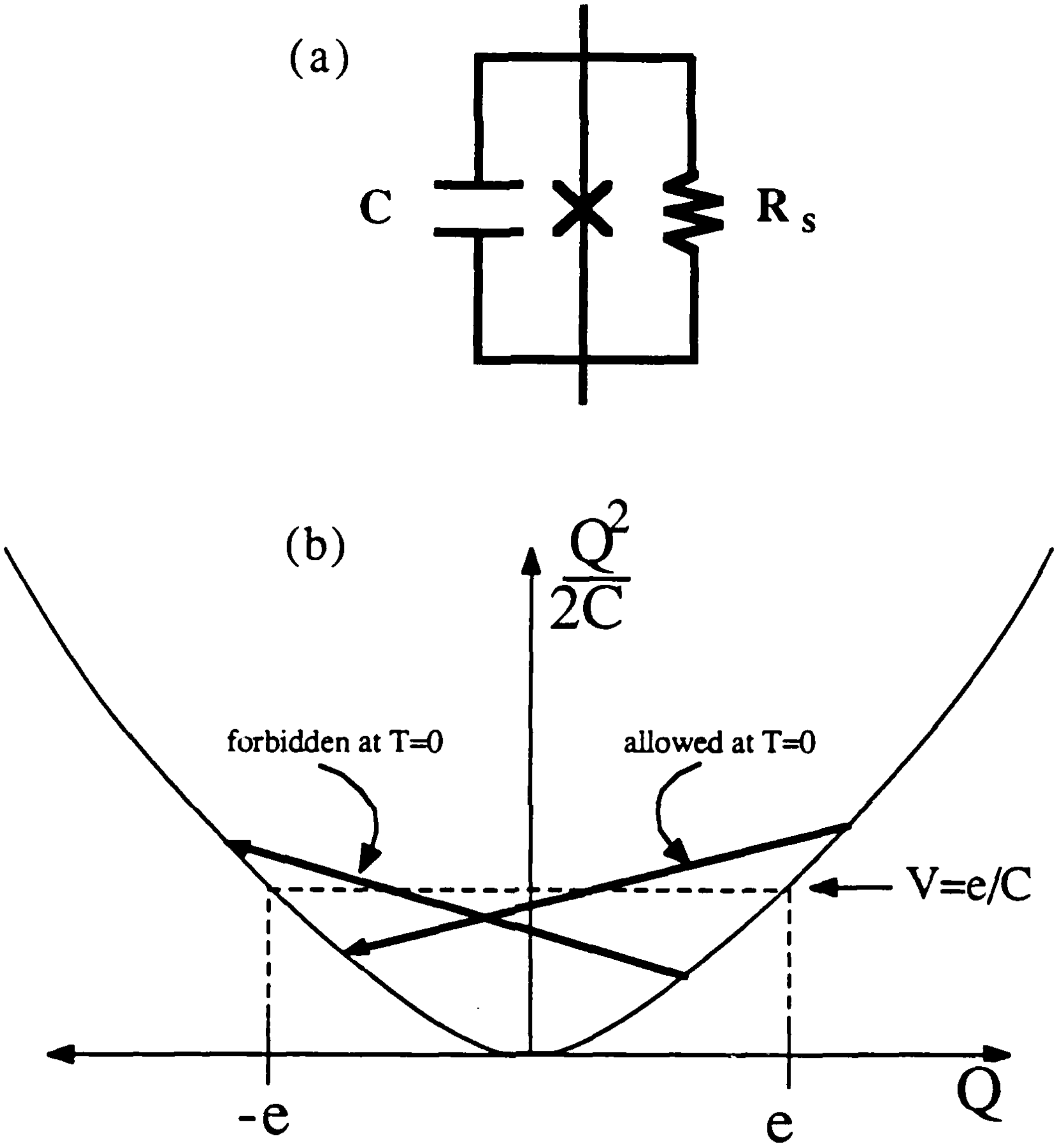

Fig. 2.4: A diagram of a simple model circuit and the operation of an idealized Josephson channel. (a) the circuit, which consists of a capacitor, an ohmic resistor, and the Josephson channel. (b) the energy of the circuit as a function of Q. The two bold arrows indicate changes in Q of magnitude 2e, corresponding to having a Cooper pair tunnel via the Josephson channel. For $-e<Q<e$, the transition causes the energy to increase and is therefore forbidden at T=0. This same type of reasoning, with a quantized tunneling charge e, underlies the Coulomb blockade of tunneling in an N-I-N junction.

$$f_B = \frac{1}{R_s C}\left[\ln\left(\frac{I+I_{th}}{I-I_{th}}\right)\right]^{-1} \tag{2.10}$$

$$V(I) = R_s\left\{I - 2I_{th}\left[\ln\left(\frac{I+I_{th}}{I-I_{th}}\right)\right]^{-1}\right\} \tag{2.11}$$

The expression for f_B given above is exactly that calculated using (2.4), while $V(I)$ differs by a factor of order one for currents $I_{th} << I << I_Z$ (see Fig. 2.3).

This model cannot account for the high current region mentioned above where the junction voltage grows, and the main physics is the competition between Zener tunneling (which, because of the decreasing bandgap with increasing band index, tends to drive the system to ever higher bands) and interband transitions due to current fluctuations from R_s (which, by (2.6) favor transitions to lower bands for which $\Delta E_{n,n'} < 0$).

2.4 Quasiparticle tunneling dissipation

We now consider how to account for a quasiparticle tunneling shunt in the master equation picture. In contrast to the continuous flow of charge in an ordinary shunt resistor, the current through this channel consists of independent tunneling events of charge e. If we assume that the tunneling current for a fixed voltage $I_t(V)$ is known, then $\Gamma^-(V)-\Gamma^+(V) = I_t(V)/e$, where Γ^- (Γ^+) is the tunneling rate with (against) the potential difference. Detailed balance yields $\Gamma^-/\Gamma^+ = \exp(\Delta E/kT)$, where ΔE is the (positive) energy gained in the forward tunneling event, in this case eV. Taken together, we find

$$\Gamma^{\pm}(V) = \frac{1}{e}I_t\left(\frac{\Delta E^{\pm}}{e}\right)\left\{\exp\left(\frac{\Delta E^{\pm}}{kT}\right)-1\right\}^{-1} \quad , \tag{2.12}$$

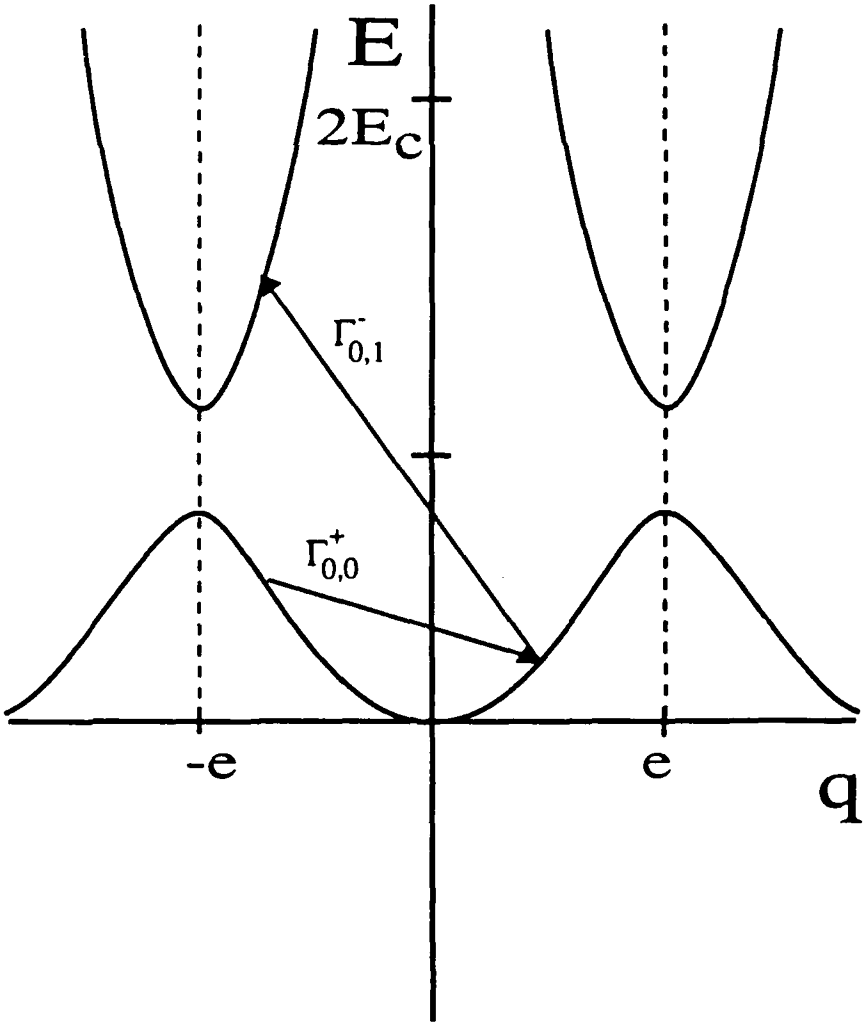

Fig. 2.5: A diagram of the bandstructure for a junction with a quasiparticle tunneling shunt at $T = 0$, showing allowed transitions in q-space. Cooper pair and Zener tunneling are as in Fig. 2.2. The quasiparticle tunneling events $\Gamma^{-}_{0,1}$ and $\Gamma^{+}_{0,0}$, which change q by $-e$ and e, respectively, are indicated by arrows. Note that all quasiparticle transitions keep q in the range $-e \leq q \leq e$, indicated by the dotted lines. Adapted from Schön and Zaikin [preprint].

where $\Delta E^{\pm} = \pm eV$ is the energy difference for the voltage-biased tunneling process, and we have assumed that $I_t(-V) = -I_t(V)$.

For a Josephson junction with capacitance C and a quasiparticle shunt subject to a *current* bias (in contrast to the voltage bias considered in the last paragraph), the relevant tunneling rate is $\Gamma^{\pm}(Q)$, and a tunneling event changes the charge state of the system from Q to $Q \pm e$. A microscopic analysis shows that the expression for $\Gamma^{\pm}$ is unchanged, but the energy difference is $\Delta E^{\pm} = E_{n'}(Q \pm e) - E_n(Q)$, the difference in the *band* energies that solve (2.1). $I_t(V)$ is the full quasiparticle tunneling characteristic [Ben-Jacob, et al., 1983; Schön, 1985]. Examples of allowed transitions are pictured in Fig. 2.5. In the following discussion, we assume that only the subgap region is relevant, and that in this region $I_t(V) \approx V/R_T$.

We show a number of IVCs in Figs. 2.6 and 2.7. These curves can be split into three distinct parts, and appear to differ only quantitatively from those for a junction shunted by a *linear* resistor presented in section 2.2. The physics behind the IVC features, however, has changed qualitatively, as described below for the case $E_J \ll E_C$ and $T = 0$.

In regime I ($I < 0.1e/R_TC$) the IVC has high differential resistance. For small currents, assuming the system starts out in the lowest energy band (band 0), Q increases until $E_0(Q) > E_0(Q-e)$, at which point, by (2.12), a single electron can tunnel. The tunneling is stochastic so there is a slight variable delay before it occurs (to be contrasted with coherent Cooper pair tunneling which occurs without a lag in this theory). This delay leads to a small positive time-averaged voltage $V(I) \propto I^{1/2}$, instead of the linear dependence found in section 2.2. When I is small, Q rarely reaches the edge of the Brillouin zone, the Josephson channel is inactive, and all the current is carried by the single-electron tunneling channel. In this regime, therefore, we find single-electron-tunneling (SET) oscillations [Ben-Jacob and Gefen, 1985; Averin and Likharev, 1986].

This part of the IVC is followed by a negative-differential-resistance region (Regime II, the "Bloch nose," $0.1e/R_TC < I \ll I_{cr} \approx \{I_Z e/R_TC\}^{1/2}$), as Q is driven more and more frequently over the edge of the Brillouin zone, and coherent Cooper pair tunneling carries an ever larger part of the current. Bloch oscillations gain importance in this current range, although SET oscillations are still present.

The nose is destroyed if, on the experimental timescale, the system is driven to other bands under the influence of Zener tunneling (favoring motion to higher bands) and quasiparticle tunneling (favoring transitions to lower bands). At $T = 0$, the transition rate from the second band to the first, at values of Q not too close to the band gap (so that $\Delta E^{\pm} \approx e^2/C$), is roughly $\Gamma^- = 1/R_TC$. We see in Figs. 2.6 and 2.7 that if the nose is well defined (e.g. the curve $kT/E_c = 0.001$ in Fig. 2.7), V has fallen to 50 % of its peak by $I \sim 0.2e/R_TC$. At this current, the system traverses the Brillouin zone in a time $5R_TC$. The probability of a quasiparticle tunneling transition from the second band to band 0 in this time, preventing Zener tunneling through the *second* bandgap, is roughly $1\text{-}e^{-5} \approx 0.99$, independent of R_T. The stability of the nose, then, is determined by the likelihood of Zener tunneling alone.

Figs. 2.6 and 2.7 show that the current scale of the nose is 0.1 e/R_TC, so we rewrite the Zener tunneling rate (from 2.7) as:

$$\Gamma_Z = f_B \exp\left\{ -\frac{1}{8}\left(\frac{E_J}{E_C}\right)^2 \frac{e}{IR_TC}\frac{\pi e^2 R_T}{2\hbar} \right\}, \tag{2.13}$$

where $f_B = I/2e$ is the Bloch frequency. Zener tunneling is negligible in the Bloch nose region ($I \geq 0.1e/R_TC$) if $R_T >> (E_C/E_J)^2 h/\pi^2 e^2$. Consider the case of a junction with realistic parameters $C = 1$ fF, $R_T = 100\ \text{M}\Omega$, and $E_J/E_C = 0.1$. At $I = 0.2e/R_TC =$ 320 fA, the heart of the nose, we find $\Gamma_Z \approx 10^{-98}\ \text{sec}^{-1}$. This hypothetical sample would be a good candidate for observation of the nose and Bloch oscillations.

In the master equation theory, Zener tunneling becomes important over a small current range δI ($\delta I \sim e/R_TC << I_{cr}$) around $I_{cr} \approx \{I_Z e/R_TC\}^{1/2}$ [Zaikin and

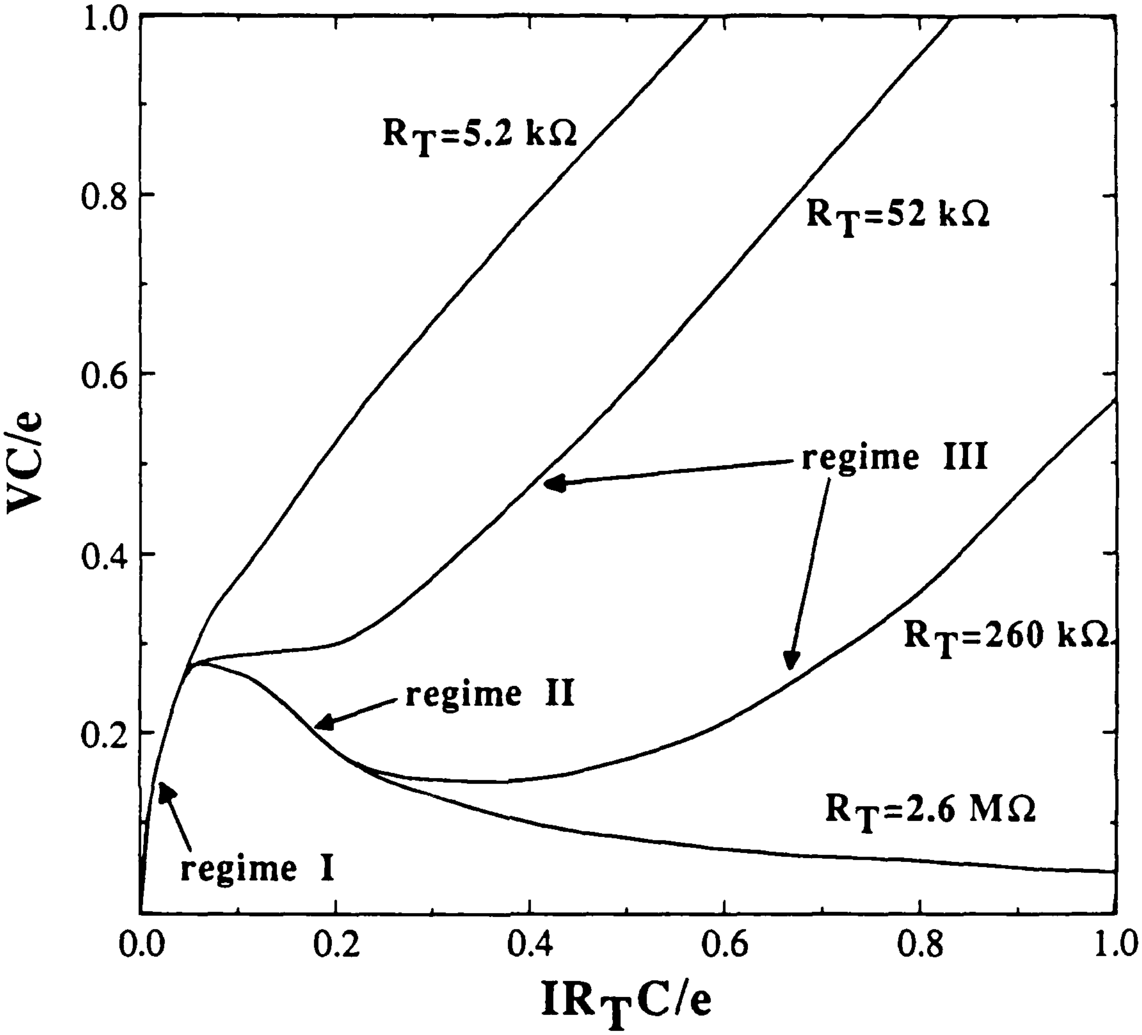

Fig. 2.6: IVCs for junctions with $E_J/E_C = 0.2$ and different levels of quasiparticle dissipation, at $T = 0$. At small currents there are SET oscillations, and the IVC has a high dV/dI (regime I). The "Bloch nose" (regime II) is sharpest in the absence of Zener tunneling and is washed out in junctions with small R_T. At large currents (regime III), Zener tunneling dominates and the IVC eventually nears that of a junction with $E_J = 0$ (about the same as the curve with $R_T = 5.2$ kΩ). Adapted from Schön and Zaikin [preprint].

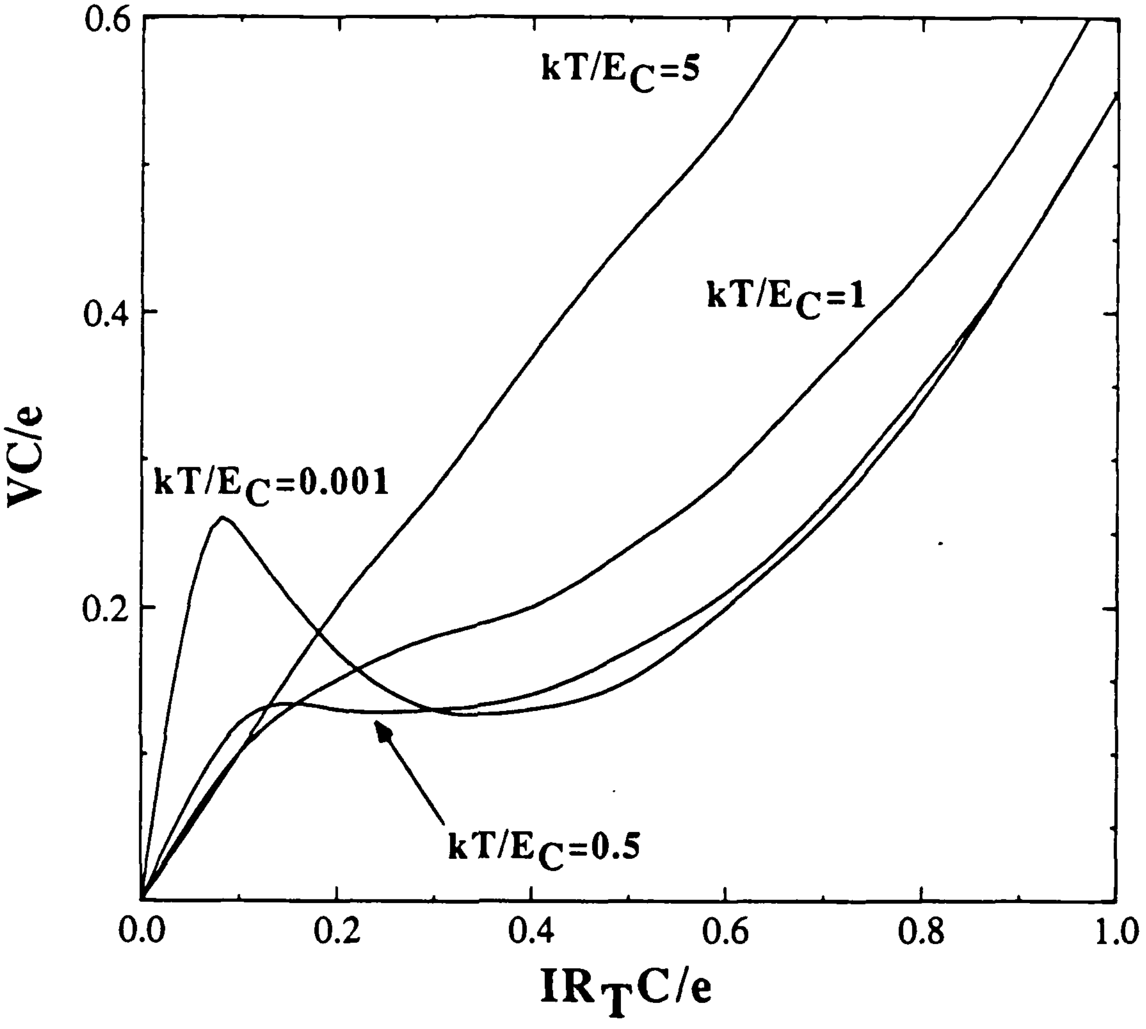

Fig. 2.7: IVCs for a junction with $E_J/E_C = 0.2$ and $R_T = 260\ \mathrm{k}\Omega$, at nonzero temperature. The effect of higher temperatures on the Bloch nose is similar to that of increased Zener tunneling (Fig. 2.6). Both phenomena cause transitions in q-space, destroying the Bloch oscillations whose onset create the nose. Adapted from Schön and Zaikin [preprint].

Kosarev, 1988]. The dc voltage rises rapidly here (regime III), from $V(I) << IR_T$ to close to the value which it would have in the absence of the Josephson effect, prompting some to identify it with the experimental I_c. At large currents, the junction IVC is the same as that for a normal tunnel junction with tunnel resistance R_T, $V(I) = IR_T + e/2C$, the second term being the voltage offset due to the Coulomb blockade.

2.5 The choice of wavefunctions

The choice of wavefunction symmetry is subtle for the Hamiltonian of (2.1), $H = Q^2/2C - E_J\cos\varphi$. Since $H[\psi(\varphi)] = H[\psi(\varphi+2\pi)]$, we have the following possibilities for boundary conditions on the eigenfunctions:

$$\begin{aligned} |\psi(\varphi+2\pi)|^2 &= |\psi(\varphi)|^2 && \text{"particle in an extended potential"} \\ \psi(\varphi+2\pi) &= \psi(\varphi) && \text{"particle on a ring"} \\ \psi(\varphi+4\pi) &= \psi(\varphi) && \text{"quasiparticle tunneling"} \end{aligned} \tag{2.14}$$

The first choice, familiar from the band structure of solids, admits all Bloch states, and applies if the sites φ and $\varphi+2\pi$ are equivalent. The second allows only Bloch states with $q = 2ne$, with n an integer, and entails the stricter assumption that φ and $\varphi+2\pi$ are *identical*. The third allows Bloch states with $q = ne$. It arises, as we discuss later, when quasiparticle tunneling is the source of dissipation. A term proportional to $\cos(\varphi/2)$ then appears in the effective Hamiltonian, allowing the possibility of 4π periodicity in $\psi(\varphi)$.

If we consider the Hamiltonian $H = (Q+Q_x)^2/2C - E_J\cos\varphi$ (see (2.3)) and make the substitution $\psi_{n,Q_x}(\varphi) = \exp(i\varphi Q_x/2e)\psi_n(\varphi)$, the second and third choices in (2.14) may be generalized. The three possibilities now allow states with all q, $q = -Q_x+2ne$, and $q = -Q_x+ne$, respectively, where n is an integer.

The appropriate boundary condition is dictated by the experimental set-up. If continuous charge flow may occur across the junction on the experimental timescale, then all values of Q_x must be admitted. If only quasiparticle tunneling contributes to charge relaxation, the 4π periodicity option is indicated. From the experimenter's point of view, the master equation approach generates IVCs with roughly the same shape, whether the dissipation is due to continuous or discrete charge transfer (see Figs. 2.3, 2.6, and 2.7). We also mention the fact that, for any *single* junction sample (i.e. a junction attached directly to leads), transmission line effects cause the leads to present a predominantly *real* (that is, resistive) impedance at high frequency, which acts, at these frequencies, as a channel for continuous charge transfer.

2.6 Phase transitions in the quantum junction

The master equation approach outlined in sections 2.2 through 2.5 incorporates dissipation perturbatively. A separate line of research incorporates non-perturbative damping by building on the pioneering work of Caldeira and Leggett (CL) [1981]. CL modeled dissipation by an ohmic resistor, R_s, in a Josephson junction as a coupling of φ to an infinite set of harmonic oscillators. The phase is coupled lightly to each *single* oscillator, but the effect of the coupling to all the oscillators may be an arbitrarily large dissipation level. The partition function of the system of junction *plus* oscillators is written as a path integral of the Lagrangian over all the relevant variables. For linear coupling between φ and the bath coordinates, CL noted that the latter may be integrated out exactly [Feynman and Hibbs, 1965, section 3.10]. The one-dimensional nature of the problem is thereby restored, but the new *effective* Lagrangian is nonlocal in time:

$$S_{eff}[\varphi(\tau)] = \int_0^{\hbar\beta} d\tau \left[\frac{C}{2} \left(\frac{h}{2e} \frac{\partial\varphi}{\partial\tau} \right)^2 - E_J \cos\varphi \right] \tag{2.15}$$

$$+ \frac{1}{2} \int_0^{\hbar\beta} d\tau \int_0^{\hbar\beta} d\tau' \alpha(\tau - \tau') [\varphi(\tau) - \varphi(\tau')]^2 \text{ , where}$$

$$\alpha(\tau) = \frac{\hbar^2}{8\pi e^2 R_s} \frac{(\pi / \hbar\beta)^2}{\sin^2(\pi\tau / \hbar\beta)} \ . \tag{2.16}$$

Starting from a microscopic theory, Ambegaokar, Eckern, and Schön [1982] considered a tunnel junction between two BCS superconductors. Assuming that the gap was much larger than all other energy scales [e.g. eV, kT, $\hbar/RC$], and that for $V << 2\Delta/e$ the quasiparticle characteristic was $I(V) = V/R_T$, they found a different effective Lagrangian,

$$S_{eff}[\varphi(\tau)] = \int_0^{\hbar\beta} d\tau \left[\frac{C^*}{2} \left(\frac{h}{2e} \frac{\partial\varphi}{\partial\tau} \right)^2 - E_J \cos\varphi \right] \tag{2.17}$$

$$+ \frac{1}{2} \int_0^{\hbar\beta} d\tau \int_0^{\hbar\beta} d\tau' \alpha_t(\tau - \tau') \left[1 - \cos \frac{\varphi(\tau) - \varphi(\tau')}{2} \right] \text{, where}$$

$$\alpha(\tau) = \frac{\hbar^2}{2\pi e^2 R_T} \frac{(\pi / \hbar\beta)^2}{\sin^2(\pi\tau / \hbar\beta)} \ . \tag{2.18}$$

Important aspects of the action in (2.17) are:

(i) the capacitance $C^* = C + \delta C$, where $\delta C = 3\pi\hbar/32\Delta R_n$, has been renormalized by quasiparticle tunneling. As illustrated in Fig. 2.8, this may be thought of as the imaginary part of the quasiparticle response, dictated by the Kramers-Kronig relations. The presence of the gap yields a real response which, taken alone, violates causality, in contrast to the frequency-independent response of an ordinary resistor [Hu, et al., 1990].

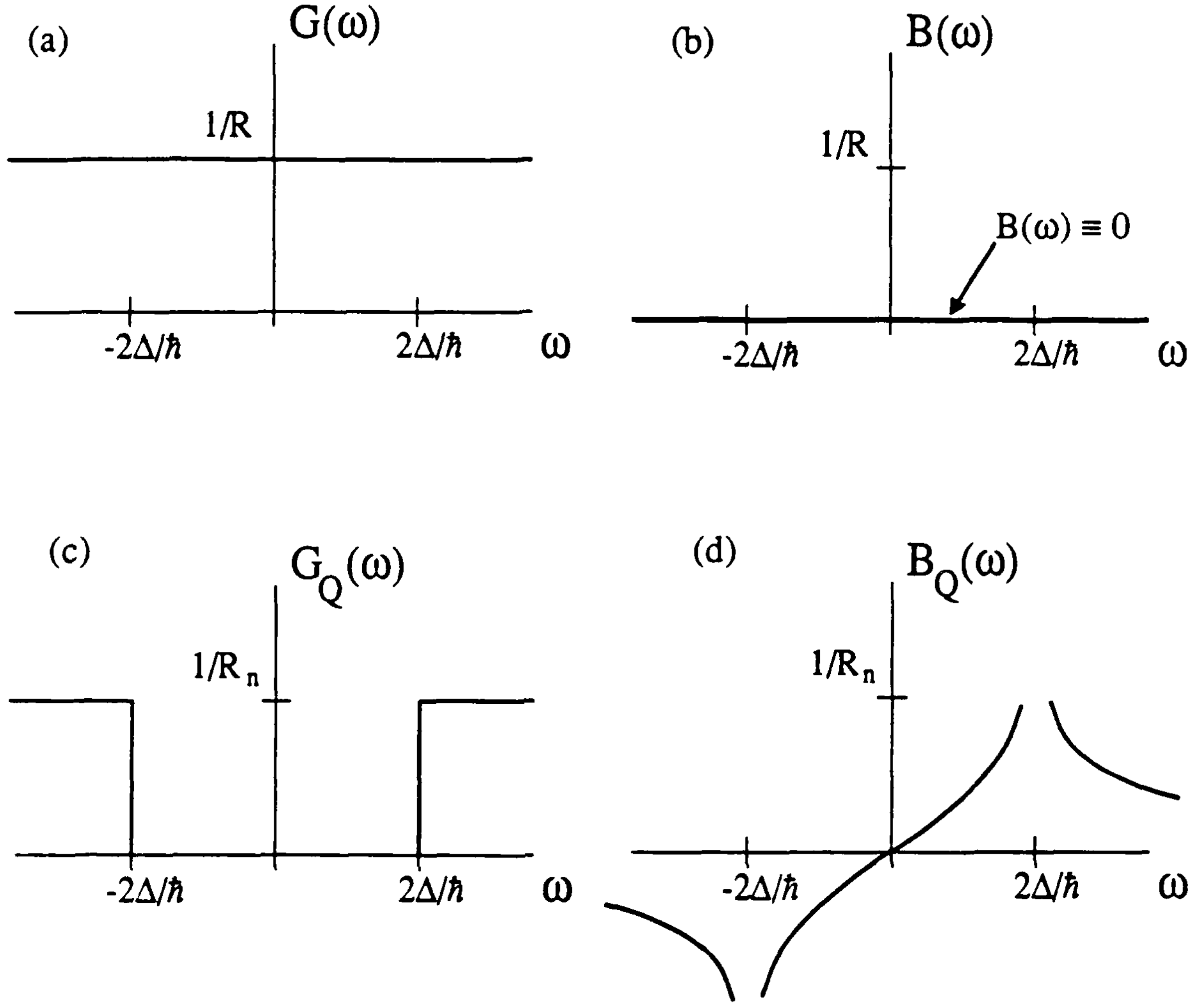

Fig. 2.8: The real and imaginary parts of $Y(\omega) = G(\omega)+iB(\omega)$, a causal small-signal response function, are related by the Hilbert transform [Bracewell, 1978, p. 272]:

$$B(\omega) = \frac{1}{\pi}\int_{-\infty}^{\infty}\frac{G(\omega')}{\omega'-\omega}d\omega' \text{ and } G(\omega) = -\frac{1}{\pi}\int_{-\infty}^{\infty}\frac{B(\omega')}{\omega'-\omega}d\omega' .$$

For a resistor, $G(\omega) = 1/R$ (a), so $B(\omega) = 0$ (b). A good approximation to the in-phase response of a quasiparticle tunneling channel at $T = 0$ is $G_Q(\omega)$, shown in (c). The Hilbert transform of this function (d) is linear near the origin, so the low-frequency response is capacitive, $B(\omega) = i\omega\delta C + \Theta(\hbar\omega/\Delta)^3$, where $\delta C = \hbar/\pi R_n\Delta$ in this approximation. A more thorough analysis [Eckern, Schön, and Ambegaokar, 1984] yields $\delta C = 3\pi\hbar/32R_n\Delta$.

(ii) the term in the action resulting from the coupling to the environment now goes as cos $\theta/2$, where $\theta = \varphi(\tau)-\varphi(\tau')$, instead of θ^2, as in (2.15). This new 4π periodicity in φ reflects the e-quantized nature of quasiparticle tunneling.

Both these effective Lagrangians have a phase transition at $T = 0$ as the dissipation level is increased from zero. For an ohmic shunt, the phase transition occurs at $R_s = h/4e^2 \approx 6.4$ kΩ, independent of E_J/E_C. When $R_s > h/4e^2$ (weak dissipation), φ can tunnel through the washboard potential barriers. Mathematically, $<[\varphi(\tau)-\varphi(0)]^2> \rightarrow \infty$ for large τ. When $R_s < h/4e^2$ (strong dissipation), quantum fluctuation are suppressed, and φ is localized in the potential: $<[\varphi(\tau)-\varphi(0)]^2>$ is finite for $\tau \rightarrow \infty$ [Schmid, 1983].

When quasiparticle tunneling provides the dissipation, the situation is more complicated. Since the action is periodic under shifts of 4π (instead of 2π, as is the case with Josephson tunneling only), the energy bands have the symmetry $E_n(Q_x+e) = E_n(Q_x)$. The Brillouin zone is now only half as large, extending from $Q_x = -e/2$ to $Q_x = e/2$, but the number of energy bands is doubled (see Fig. 2.9).

The energy bands are distorted by quasiparticle tunneling to a degree dependent upon $\alpha_t = h/\pi^2e^2R_T \approx 2.6\ \text{k}\Omega/R_T$. When $\alpha_t = 0$, the bands cross at $|q| = e/2$. Nonzero dissipation causes the bands to be tangent there. As α_t increases, the energy bands flatten, and at $\alpha_t = 2$ the bands are degenerate over a finite range of q, which starts at $q = \pm e/2$ and expands towards $q = 0$ as α_t grows. Fig. 2.10 shows how the value of α_t at which the bands become degenerate is a function of both q and E_J/E_C. The deformed energy bands may then be included in a master equation to predict IVCs for these junctions.

A flatter band structure leads to an IVC with a less-pronounced Bloch nose. Moreover, the size of the ac voltage produced by the Bloch oscillations (proportional to the maximum slope of $E_0(Q)$ is also decreased. Thus, strong quasiparticle dissipation destroys the features associated with the quantum mechanics of φ.

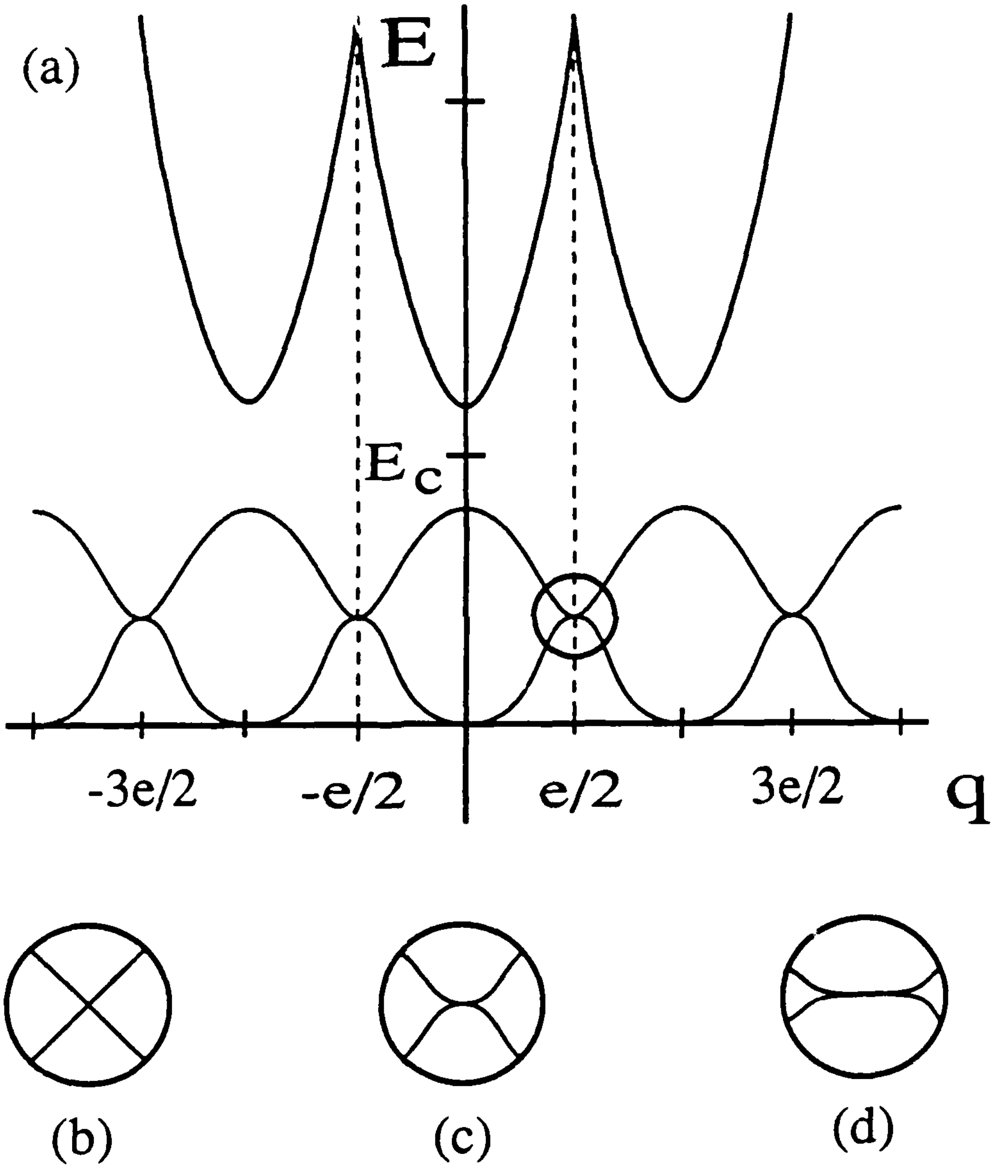

Fig. 2.9: Energy bands for a junction with quasiparticle tunneling dissipation. (a) the energy bands. The number of bands has doubled, and the Brillouin zone has collapsed to $-e/2 \leq q \leq e/2$ (dotted lines). The bands intersect at the zone edge, but are distorted to a degree dependent on the strength of the dissipation. (b), (c), and (d) are close-ups of the zone edge. (b) $\alpha_t = 0$. The bands cross at $|q| = e/2$. (c) $0 < \alpha_t < 2$. The bands are tangent at the zone edge. (d) $\alpha_t \geq 2$. The bands are degenerate over a finite region of the Brillouin zone, which grows with α_t. Adapted from Guinea and Schön, [1986].

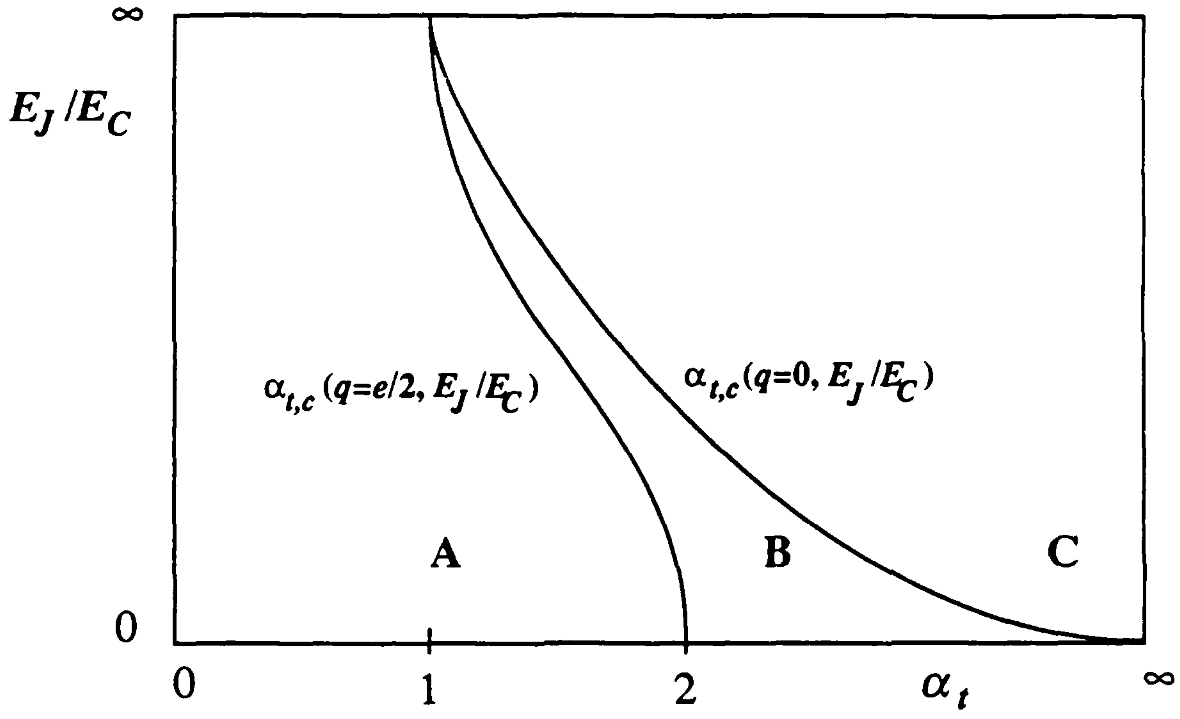

Fig. 2.10: The phase diagram for the superconducting tunnel junction with a quasiparticle tunneling shunt. The critical value of the quasiparticle dissipation, $\alpha_{t,c}$, depends on E_J/E_C and q. In region A, the lowest two energy bands are degenerate only at $|q| = e/2$. In region B, the two lowest bands are degenerate in a finite range of q, near the Brillouin zone edge. Finally, in region C the two lowest bands are degenerate over the full Brillouin zone, $-e/2 \leq q \leq e/2$. The two curves show how $\alpha_{t,c}$ varies with E_J/E_C for the fixed values $q = e/2$ and $q = 0$. The like curves for intermediate values of q lie between these two, in region B. Adapted from Schön and Zaikin [preprint].

2.7 Summary

In this chapter, we have outlined some of the consequences of quantum mechanical fluctuations of the phase in superconducting tunnel junctions. The important results are:

(i) the IVC is strongly altered from that when the phase is governed by the classical RCSJ model. Specifically, the "Bloch nose" develops for currents $I < e/R_T C$. The voltage scale of the nose is

$$V_n \approx \begin{cases} e/4C & E_J << E_C \\ \Delta_0/e & E_J >> E_C \end{cases} \tag{2.19}$$

when the effects of dissipation, Zener tunneling and temperature may be ignored. Here, Δ_0 is the width of the first tight-binding band, defined in (2.2). Bloch oscillations exist in the region of negative differential resistance, and, when the dissipation is due to quasiparticle tunneling, SET oscillations occur for small currents.

(ii) in the presence of sufficiently strong ohmic or quasiparticle-tunneling dissipation, the junction undergoes a phase transition. For dissipation larger than a critical level, quantum fluctuations are suppressed, smearing the Bloch nose and reducing the ac voltage associated with the Bloch oscillations.

Chapter Three
Experimental Techniques

This chapter describes how the samples used in this work were made and measured. Section 3.1 outlines the lithography and deposition processes [fully described in Appendix 1] used to fabricate 0.04 μm^2 junctions, while in section 3.2 we present the techniques used to measure the samples at dilution refrigerator temperatures.

3.1 Sample Fabrication

By the summer of 1984, it was clear that a technical advance was needed to continue the Tinkham lab research into the physics of ever smaller superconducting tunnel junctions. Danchi's work on junctions with 1 μm dimensions [1983] pushed optical lithography near its intrinsic limit due to the wavelength of the exposing light. Fortunately, research into submicron patterning techniques had been conducted by workers at many laboratories. Hatzakis' investigations of PMMA electron beam resists [1971, 1975] had shown the feasibility of linewidths below 100 nm, representing a potential decrease in junction area by two orders of magnitude. Junctions of this size had been fabricated [Howard, 1979], but systematic research into their properties had yet to be done.

Theoretical considerations indicated that novel physics would be found in samples of area (300 nm)^2, where $E_J \approx E_C \approx 1$ K for a typical critical current density and dielectric constant. Hints of these phenomena appeared in the pathbreaking work of Akoh, et al. [1986], the first to observe the R_0 and reentrant I_c phenomena. Excited by these developments, we set out to build a submicron fabrication capability at Harvard.

3.1.1 Contact pads

We found it convenient to pattern the gross structures on the chip with photolithography before moving to electron beam lithography (EBL) for the submicron features. The contact pads frame an area of about (80 μm)^2, matched well to the field of view of the SEM at a magnification of 1000x. The pads need to have high electronic (and thereby thermal) conductivity, adhere well to the oxidized silicon substrate and form no oxide even after prolonged exposure to atmosphere.

The combination of Au pads with a thin Cr underlayer has all these attributes. The Cr acts to improve the adhesion of the pads. They routinely survive a vigorous cleaning prior to EBL, including 30 minutes in boiling photoresist stripper and a total of 20 minutes ultrasonic cleaning in various solvents. The choice of Au is prompted by its high conductivity and lack of a natural oxide. We evaporated about 50 Å Cr followed immediately by 450 Å Au. Thinner layers of Cr were used by other members of this group; it appears that even 25 Å Cr forms a relatively smooth film. When making the pads, it was essential to fill the cold trap in the diffusion-pumped evaporator; the Au peeled away from the Cr in bilayers made with the cold trap empty. We believe that when the cold trap is not used, pump oil contaminates the Cr surface during the time between evaporations, leading to poor Au-Cr adhesion.

When using such a two part process, it is of great importance that the edges of the contact pads be smooth, so that the film evaporated after EBL will not break as it passes from the contact pad onto the bare Si. To achieve this, some undercut is needed in the photoresist pattern which defines the contact pads (see Fig. 3.1). We used a simple chlorobenzene technique [John Clarke, private communication] that gave undercut too small to see with an optical microscope, but sufficient to give easy liftoff and edges smooth enough for the Sn films. We should point out, however, that the Sn films were rather thick (two layers of about 700-1000 Å each). It may be that our pads were not suitable for use with extremely thin films. Due to this concern, Walter Smith of this group used a three-

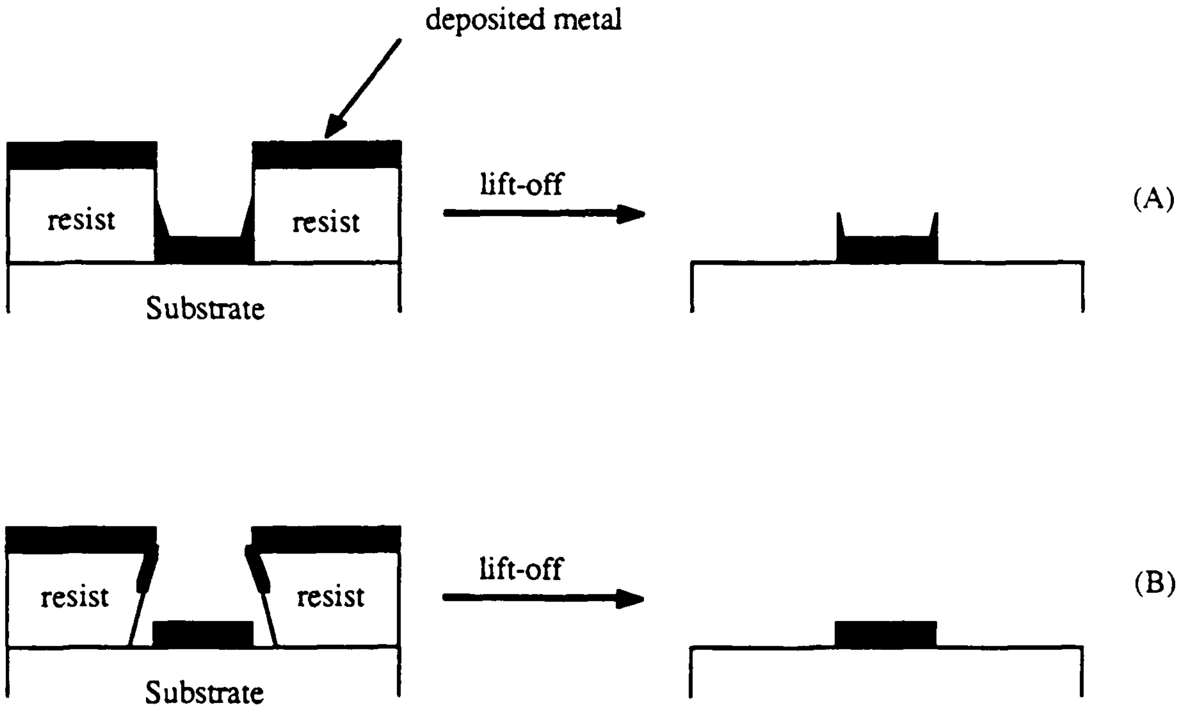
deposited metal
resist
resist
lift-off
(A)
Substrate
resist
resist
lift-off
(B)
Substrate

Fig. 3.1: A vertical resist profile (A) can be coated by metal if the deposition process is not fully collimated, leading to a film with rough edges. This can tear a film deposited later. The undercut profile (B) gives a smoother edge.

layer photolithographic process to pattern pads for his research on quantum conductance fluctuations in 200 Å thick Pd-Si wires [1989].

When making pads, we found that some masks, which showed no obvious imperfections, could be unsuitable for patterning even such large structures (minimum feature size 40 μm). The use of one particular mask led to well reproduced pad sets interspersed with pad sets that were severely flawed, even when the mask was thoroughly cleaned and extreme care taken to achieve good contact when using the mask aligner. Eventually we discovered that using a different mask resulted in essentially perfect pad sets over the entire surface of a 2" wafer with little special effort. This problem was probably caused by a large scale warp in the original mask. Presumably, the mask had this imperfection when delivered by the supplier.

We also experimented with methods to pattern the contact pads in the electron resist that would eventually define the sample as well. We used a deep ultraviolet (DUV) source [Oriel, 500 W] to expose the contact pad pattern in the bilayer electron resist. We then developed the sample and rinsed it thoroughly. We could continue with EBL after this, using the edge of the resist as an alignment mark in the SEM. Eventually, this method would lead to both pads and sample made of Sn.

This method had the advantage of needing only one evaporation to make the sample. DUV lithography is relatively simple, the only major changes from photolithography being the use of a DUV source [~$15,000], and quartz masks instead of standard soda lime glass which absorbs at DUV wavelengths. This second difference involves a cost increase from $3 to $60 per mask. An additional complication is the danger of DUV radiation. Although any pair of glasses will protect the eyes by attenuating the DUV, this wavelength region damages human skin; even the small amount of light that leaks out through a crack in the lamp housing once the protective cover is removed can cause a "sunburn" after about 10 minutes exposure at close range.

To provide good contact between mask and sample during DUV exposure, we used a vacuum chuck designed by Martin Forrester and built by the Harvard shop. The chuck (Fig. 3.2) is simple, and provides excellent contact; with it we can achieve 2 μm linewidth, although there is no alignment ability.

3.1.2 Electron beam lithography: resist considerations

Once we have successfully fabricated a set of contact pads, EBL is used to create the superconducting tunnel junction itself. We use an angle-evaporation technique pioneered by Dolan [1977], forming the junction with two evaporations at proper angles to the substrate. The technique demands an undercut resist profile with a "suspended resist bridge" (Fig. 3.3). This requirement is a stringent one which results in larger-than-optimal linewidth, as discussed below.

Sn tends to ball up on oxidized Si, forcing the use of moderately thick (70 nm or greater) films to produce continuous lines. The rule of thumb for reliable lift-off is that the resist structure be three times as thick as the deposited metal; a PMMA system of about 500 nm thickness is necessary. We used a bilayer with PMMA(MAA), a PMMA copolymer, as the lower layer (about 500 nm thick), and PMMA (about 100 nm thick) as the top layer [see Appendix 1]. As usual, the top ("imaging") layer should be as thin as possible, since the minimum linewidth achievable in a resist is roughly the layer thickess.

In this resist system, the lower layer is more sensitive to electrons, that is, in a threshold model of resist development (where a volume with more than some exposure level is totally disolved by the developer, while one with less is totally unaffected), the minimum energy dose needed to produce 100 % resist loss is smaller for the lower layer than for the top layer. If the exposure profile due to the incident beam is roughly Gaussian, then a wider hole will be made in the lower layer than in the imaging layer (see Fig. 3.4). This sensitivity-gradient trick is often used in multilayer resist schemes for obtaining an

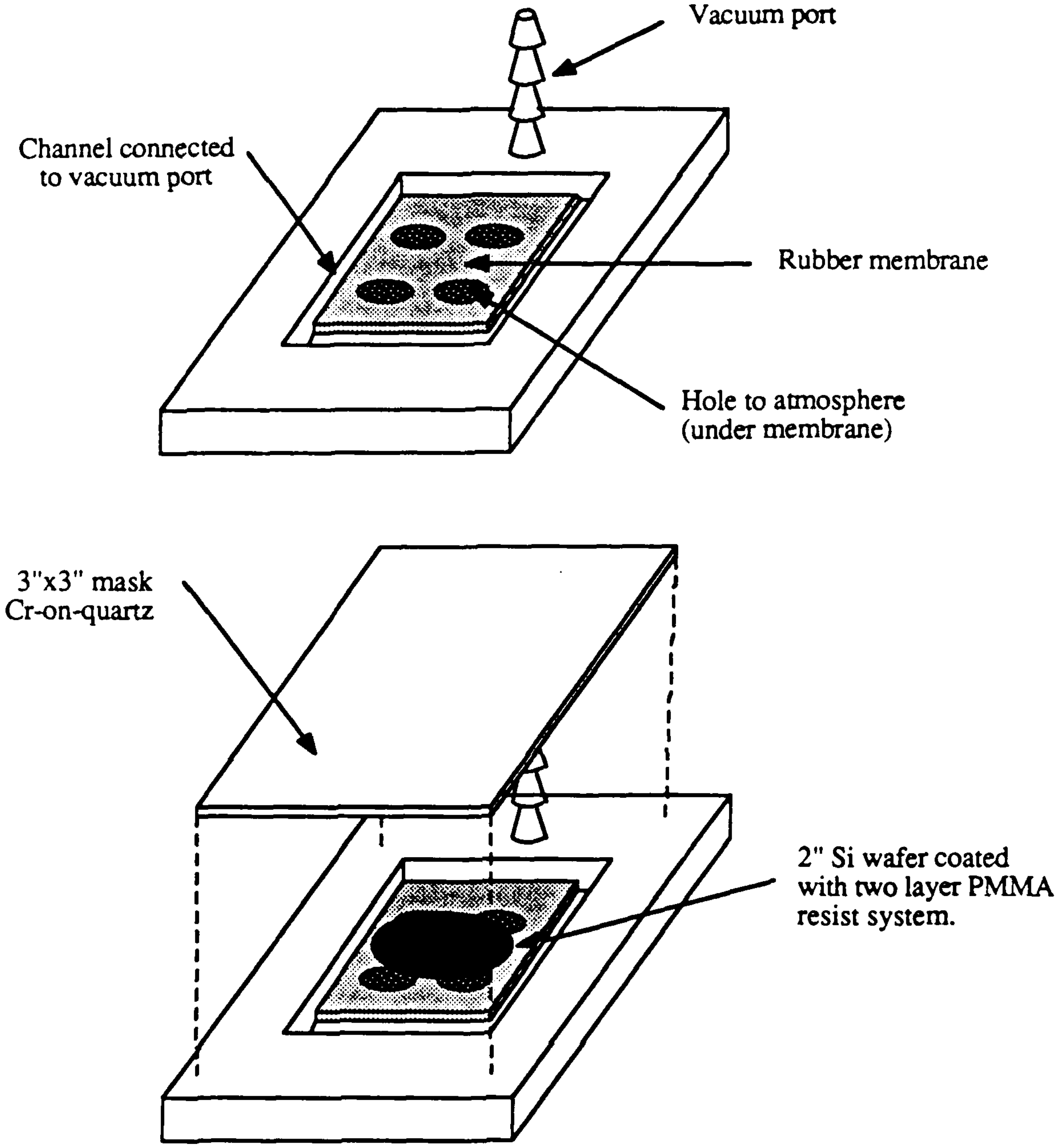
Vacuum port
Channel connected to vacuum port
Rubber membrane
Hole to atmosphere (under membrane)
3"x3" mask Cr-on-quartz
2" Si wafer coated with two layer PMMA resist system.

Fig. 3.2: The DUV contact printing chuck.
Top: The chuck. Bottom: Mask and chuck with wafer in position for exposure.
A vacuum space between the mask, the baseplate, the channel, and the rubber membrane is evacuated via the hose barb. The pressure difference between this volume and atmosphere drives the membrane into the wafer, and the wafer into good contact with the mask.

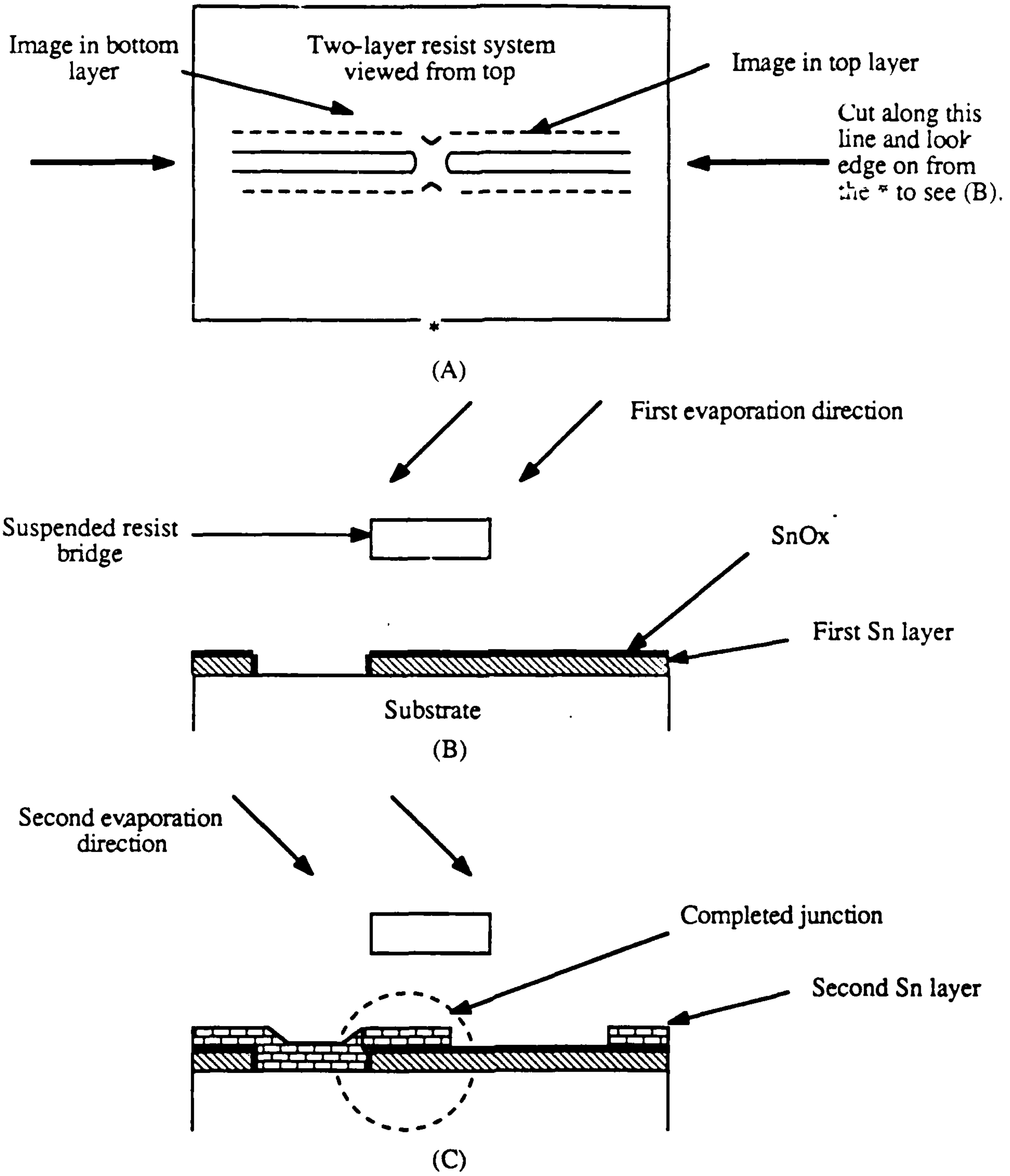
Image in bottom layer
Two-layer resist system viewed from top
Image in top layer
Cut along this line and look edge on from the * to see (B).
*
(A)
First evaporation direction
Suspended resist bridge
SnOx
First Sn layer
Substrate
(B)
Second evaporation direction
Completed junction
Second Sn layer
(C)

Fig. 3.3: (A) Exposing a line with a gap in the top layer (solid line), leaves a continuous channel in the lower layer due to its extra sensitivity (dotted line), creating a suspended resist bridge. If we cut along the line of the arrows in (A) and look at the substrate edge on, we see the bridge (B). Two evaporations at angles to the substrate create the tunnel junction (C).

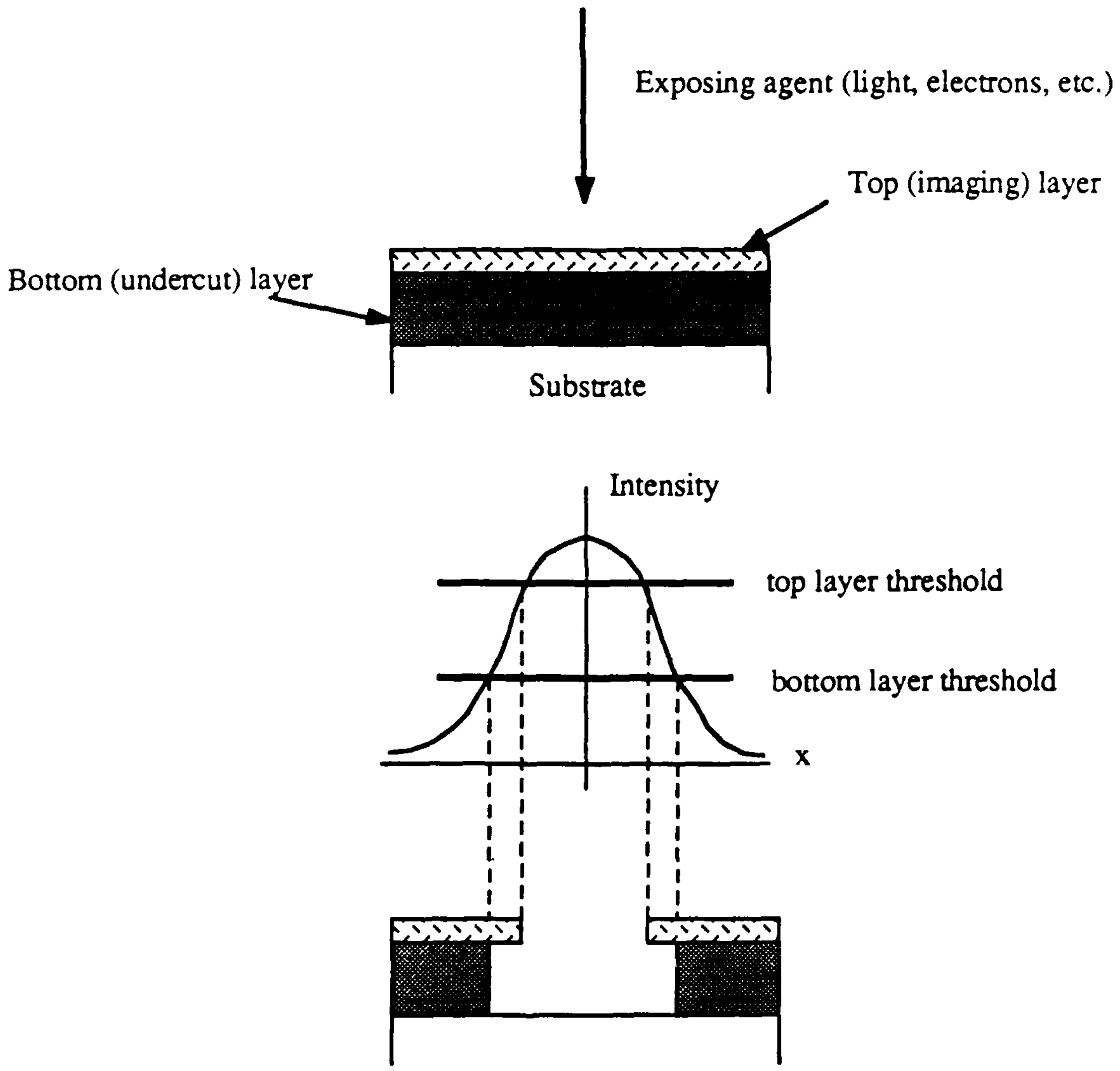
Exposing agent (light, electrons, etc.)
Top (imaging) layer
Bottom (undercut) layer
Substrate
Intensity
top layer threshold
bottom layer threshold
x

Fig. 3.4: The combination of a more sensitive bottom layer and a Gaussian exposure profile leads to an undercut resist profile. Any region in the top (bottom) layer exposed more than the top (bottom) layer threshold is dissolved by the developer. The opening in the bottom layer is therefore larger than the opening in the top layer.

undercut profile, but it is not the only approach. For an alternative, see the discussion of "canyon lithography" in section 3.1.4.

If we could expose an electron resist at a single point, there would be a "proximity effect," i.e. energy deposited in regions which were nominally unexposed. Electron scattering in the resist itself generates this cross exposure. As the electron beam enters the resist, it creates a forward beam of secondary electrons which exposes surrounding regions. We model this as a slight increase in the beam diameter. A second important process is backscattering of electrons from the substrate, which can be suppressed by using a substrate that is transparent to electrons, such as a SiN membrane [Broers, et al., 1978]. The combined effect of these two processes is a current density J, a distance r from the exposure point, modeled as a double-Gaussian [Wittels, 1980]:

$$J(r) = \frac{I}{\pi}\left\{\alpha^2 e^{-\alpha^2 r^2} + b\beta^2 e^{-\beta^2 r^2}\right\}. \tag{3.1}$$

In (3.1), $1/\alpha$ and $1/\beta$ are the width of the incident and backscattered beams respectively, b is the fraction of electrons backscattered, and I is the beam current. As the electron energy increases, both $1/\beta$ and b increase. The net effect is to *reduce* the effect of backscattering with increasing incident energy, since although the total number of backscattered electrons increases, the total area exposed increases more, and the dose (energy/cm^2) decreases.

Ordinarily we decrease the backscattering to minimize the linewidth. In our samples, however, backscattered electrons help create the undercut. An incident beam energy of 35 keV, optimal for the electron optics of our SEM, led to insufficient undercut. 12 keV electrons produced an undercut profile that could be inspected with an optical microscope. This allowed junction yields approaching 90 %. Using a 12 keV source, however, increased the minimum linewidth to 200 nm from the 100 nm obtained at 35 keV.

3.1.3 Electron beam lithography: the EBL system

The SEM beam is controlled with two voltages, one for the X direction and one for Y. When imaging, these voltages are provided by the scan generator module on the SEM control panel. Most SEMs have a three-pin port where an outside source can provide these two voltages whenever the third pin is in some specified voltage state (e.g. grounded). We use just this capability to do the EBL.

The system used to control the electron beam of the SEM is sketched in Fig. 3.5. We use an IBM Instruments 9000 computer§ and homemade digital-to-analog conversion (DAC) electronics to drive the electron beam of a JEOL 35U scanning electron microscope. The computer also controls the beam blanker. The DACs have 16 bit resolution, of which 15 are used for beam writing. At a magnification of 1000x (standard for high resolution writing) the pixel size is about 50 Å, significantly less than the size of the beam. The minimum linewidth made in PMMA on a Si substrate at Harvard is 100 nm. We have also written photolithographic masks with 2 μm critical dimension at a magnification of 100x, corresponding to a 1 mm^2 field of view [Forrester, 1988].

The heart of the system is the EXPOSE program, written by Dr. Horst Rogalla, a visitor to the Tinkham group, now at the University of Twente, The Netherlands. The distinguishing feature of this program is that only after exposing one point are the coordinates of the next point calculated; most other systems calculate the coordinates of all the points, load them into a fast access memory, and only then expose the pattern. The program has a maximum output rate of 1 MHz. The maximum exposure rate is currently limited by the beam deflection coils in the microscope, rather than the software.

Clearly, the weak link in this system is the computer itself. IBM Instruments no longer exists, and there is no service support for the machine. The change to an IBM PC

[§] This machine is obsolete, but uses a Motorola 68000 processor as does the more modern Macintosh.

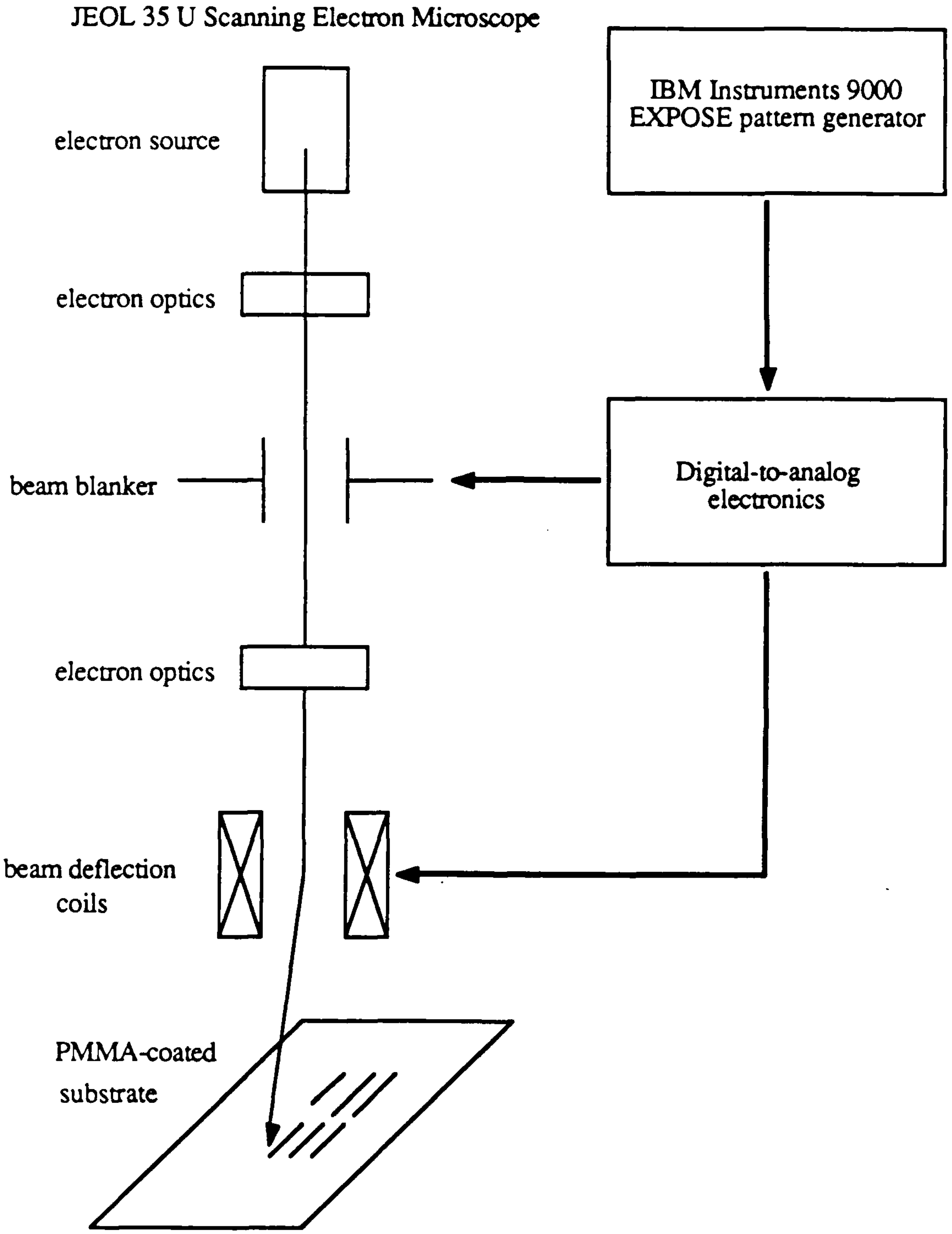
JEOL 35 U Scanning Electron Microscope
IBM Instruments 9000 EXPOSE pattern generator
electron source
electron optics
beam blanker
Digital-to-analog electronics
electron optics
beam deflection coils
PMMA-coated substrate

Fig. 3.5: The Harvard electron-beam lithography system. The IBM Instruments 9000 computer drives DAC circuitry that controls both the beam position and the beam blanker.

or Macintosh should be a high priority. Today the lab is vulnerable to a failure of the IBM Instruments computer, which could bring several research projects to a standstill.

When patterning with the EBL system, proper focusing of the SEM near the writing region is crucial. A useful trick exploits the natural contamination of the vacuum system by the diffusion pump to image the electron beam. If the beam is placed in "spot mode" for several minutes at a high magnification (e.g. 60,000x), a white dot is visible when the full area scan is restored. This object is "contamination resist," pump oil carbonized by the electron beam [Broers, 1976]. When the beam is focused well, this spot is about 100 nm in diameter and circular. If the astigmatism is poorly adjusted, the spot is an ellipse. The spot can even have three lobes, indicating very poor astigmatic adjustment indeed. If no spot forms at all, the beam is probably not focused on the resist surface. An added benefit of this process is that the small, round spot can be used to improve the focus further.

It is unclear how the size of the spot compares to the true beam size. The longer the beam remains in one place, the larger is the resultant spot. The spot is imaged easily, which seems impossible if it is the same size as the beam. The specifications of the SEM, moreover, give the optimum beam diameter as 7.5 nm. Our inability to pattern lines smaller than 100 nm could indicate that the beam is not ideal, since other groups report lines as small as 40 nm in PMMA on thick substrates [Mackie, 1985; Rooks, 1987]. It is likely that the purchase of a new SEM will lead to better EBL at Harvard.

3.1.4 Tin deposition

The evaporation process is detailed in Appendix I. All the samples in this report were made of Sn, largely for historical reasons; this material has been a mainstay for junction fabrication by this group for 15 years. Tin has several advantages for the fabrication of small geometric capacitance tunnel junctions. First the native oxide has a relatively small dielectric constant, $\varepsilon = 6\varepsilon_0$ [Wang, 1978; Danchi, 1983], to be compared with that of NbOx ($\varepsilon = 30\varepsilon_0$) [Basavaiah, 1976] and Al_2O_3 ($\varepsilon = 8\varepsilon_0$) [Gurvitch, 1983].

Secondly, since $T_c = 3.8$ K, we can measure these junctions in a standard helium cryostat and still reach temperatures as low as $T_c/3$.

The major disadvantage of Sn is its inability to cycle thermally. The samples were invariably shorted out after the second cooling. Samples that sat at room temperature for periods longer than a day also were shorted, so we cooled the samples as quickly as possible once the evaporation was finished, typically within 12 hours. We infer that Sn is under stress after evaporation, and that this stress is relieved by thermally-activated needling, puncturing the fragile oxide barrier. Samples were stable for weeks at liquid nitrogen temperature and indefinitely below 4 K.

It is clear that Al is a better material for continued research. Its slightly higher dielectric constant is offset by its ability to cycle and to form continuous films at smaller thicknesses, allowing thinner resist structures and better minimum linewidth. Once EBL at Harvard is capable of $(70\text{nm})^2$ junctions, even a Al_2O_3 barrier will result in $C \approx 0.2$ fF, so that $E_C \approx 5$ K.

3.1.5 Areas for future work

We take a moment to consider promising avenues for improving lithography at Harvard. Lift-off samples with 40 nm linewidth have been obtained using a two-layer structure with 150 K molecular weight (MW) PMMA as the bottom layer and 496 K PMMA as the top layer [Mackie, 1985; Rooks, 1987]. As usual, the bottom layer is more sensitive to electron exposure. The entire structure is extremely thin (less than 200 nm total thickness), and would require the use of Al as the junction material. Due to its parallel nature, X-ray lithography would be useful for more complicated structures like large tunnel junction arrays.

With the help of some talented undergraduates, we investigated fairly deeply a novel form of patterning known as "Canyon lithography" (C-L). Most conventional schemes for generating undercut have the weakness that both the image line and the undercut are produced by the same physical process in layers with similar material properties. Therefore, the goals of minimum linewidth and maximum undercut are at cross purposes. As noted above, this limitation led to the compromise of 12 keV electrons and the consequent linewidth doubling. C-L, detailed in Appendix 1, avoids this problem by using a metal imaging layer and polymer undercut layer, whose vastly different properties allow linewidth and undercut to be independently optimized [Dolan, 1983].

The best results with C-L include a 30 nm Au line and $(60\ \mathrm{nm})^2$ Au-Au "junctions." These were all made without electrical contacts, however, precluding measurement of their transport properties. The technique is clearly promising, but has the drawbacks of more complexity than the standard expose-develop-metallize process (the angle evaporation and reactive ion etch steps), and lack of good reproducibility. This latter problem is due to the short exposure times in C-L, used to achieve intentional *under*exposure of the resist. This requires an EBL system with adequate "settling time" and "blanking" capability to ensure accurate, reproducible exposure. Our system has a programming bug in the "settling time" subroutine, so that only the first point of any exposure has a settling time, and the blanker is an inductive device rather than the faster electrostatic (capacitive) variety.

Finally, we note that Al structures as small as 20 nm have been made using AlF_3, a self-developing metallic resist [Kratschmer and Isaacson, 1986]. Still in its infancy, this technology will certainly be exploited for transport research in the near future.

3.2 Measurement at Dilution Refrigerator Temperatures

Using a dilution refrigerator for the measurements presented opportunities and technical challenges. The ability to reach temperatures as low as 20 mK held the possibility of observing new phenomena, and the need to be well below $E_C/k \approx 1$ K argued against a standard pumped-liquid-helium system or even a ^{3}He system. We could also investigate the normal state properties of the junctions with the 7 T superconducting magnet attached to the mixing chamber.

These advantages come at a price. The difficulties of achieving such low temperatures, measuring them accurately, and controlling the temperature to an acceptable precision are well known. As described below, measures not needed in ^{4}He cryostats are demanded. The small critical currents of the junctions and the low voltage levels on the R_0 branch of the I-V curve also call for careful noise reduction techniques.

For additional discussion of the dilution refrigerator shared by the Tinkham and Westervelt groups at Harvard, the reader is referred to the Technical Reports of Marco Iansiti [1988] and Walter F. Smith [1989].

3.2.1 Top-loading

An added convenience of the refrigerator is its top-loading ability. We mount the sample on the loading slug (shown in Fig. 3.6), with electrical contact made via pressed indium dots. The slug is screwed with a left-hand thread onto the end of the top-loading dipstick, a long metal tube made of two coaxial tubes joined at the end where the slug is attached. The dipstick is introduced into the inner vacuum region surrounding the mixing chamber. Liquid helium may be pumped from the refrigerator's helium reservoir, down the dipstick's central tube and back out the outer tube, thus cooling the slug to near 4.2 K. The bottom of the slug is a right-hand screw. Turning the dipstick clockwise screws the slug into the bottom of the copper tail fastened to the mixing chamber. Once the slug is tight, it is unscrewed from the dipstick by continuing to turn the latter clockwise. Eight spring-loaded contacts provide electrical continuity. With this setup, we can remove one sample, introduce a new one and cool to millikelvin temperature, all within a few hours.

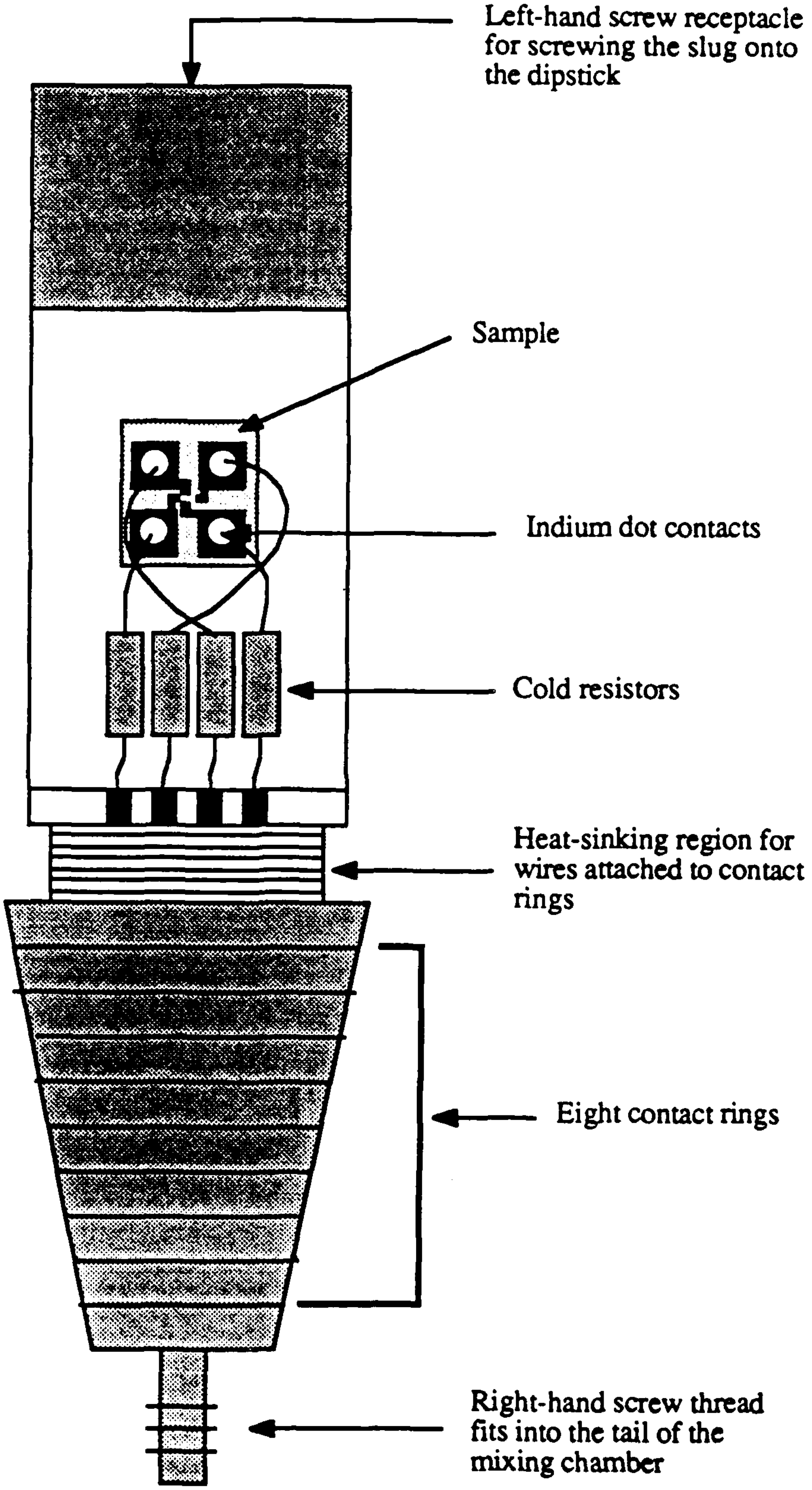
Left-hand screw receptacle for screwing the slug onto the dipstick
Sample
Indium dot contacts
Cold resistors
Heat-sinking region for wires attached to contact rings
Eight contact rings
Right-hand screw thread fits into the tail of the mixing chamber

Fig. 3.6: The top-loading slug.

3.2.2 Temperature measurement and control

For a detailed overview of the temperature measuring system in the shared dilution refrigerator at Harvard, the reader should see the Technical Report of Walter F. Smith [1989]. Two thermometers cover the temperature range 10 mK-6 K. The first is a commercially calibrated germanium resistance thermometer (Lake Shore Cryotronics), used for temperatures between 6 K and 250 mK. Below 250 mK, we use Speer carbon resistors, heat-sunk to the mixing chamber by milling a flat to expose bare carbon, which is pressed firmly against the mixing chamber with a piece of greased cigarette paper between the two to provide electrical isolation. The leads to all resistors are wrapped around heat-sinking spools at the mixing chamber, as well as the 50 mK, 600 mK, and 1.2 K stages of the refrigerator. The carbon resistors are calibrated at the start of each run with a National Institute of Standards and Technology (NIST) fixed point thermometer consisting of 5 superconductors with known T_c.

Despite the precautions taken to heatsink the carbon resistors to the mixing chamber, we noticed a slow upward drift in their resistance (i.e. a slow downward drift in the electronic temperature) with the mixing chamber held at a constant low temperature. For example, we used the center of the NIST 23 mK superconducting standard as a regulation point and found that overnight the resistance of one Speer thermometer increased from 35 kΩ (after about 30 minutes of equilibration) to 63 kΩ, corresponding to an error of 5-10 mK. An initial, fast settling to *near* thermal equilibrium was followed by a much slower relaxation to a true 23 mK state.

We solved this problem by using a new type of ruthenium oxide (RuO_2) resistor thermometer [Li, 1986; Love, 1987] which has the dual advantages of easy, reliable heatsinking and small magnetoresistance. All thermometers are mounted in the cancellation region of the 7 T magnet which is centered on the mixing chamber, but there is still uncertainty about their reliability in high field. The RuO_2 thermometer is covered by a thin insulating glass. Once leads were attached to the resistor and covered with GE varnish, we placed the resistor on the mixing chamber and slathered silver paint over all its exposed surfaces and the nearby part of the mixing chamber to make thermal contact. The resistor comes to equilibrium in 15 minutes at 23 mK, and its resistance does not change in the overnight test. In addition, its resistance at a given temperature is extremely stable from run to run: the calibrations of two runs differed by less than 10 % for $T < 100$ mK, and less than 3 % for $100\ \mathrm{mK} < T < 300$ mK.

The mixing chamber temperature is regulated with an Oxford Instruments temperature controller with proportional-integral-derivative [PID] feedback. One innovation of this research is a high-temperature regulation scheme found to work well up to 6 K. This technique extends the dynamic range in temperature to nearly 3 orders of magnitude.

For $T > 1$ K, the refrigerator has, in some sense, *too much* cooling power. If all the ^{3}He in the mixture is circulated through the dilution path, so much heat must be applied to the mixing chamber to reach 1 K that the mixture is vaporized, resulting in unstable operation. Above 0.8 K, ^{3}He and ^{4}He do not phase-separate in the mixing chamber, so no dilution occurs; the cooling is provided by ^{3}He gas (and at higher temperatures ^{4}He gas) cooled to 1 K by the condenser. The trick at high temperature is to have enough mixture circulating to provide adequate cooling power, but not so much cooling power that the temperature oscillates wildly.

To accomplish this, we extract nearly all the mixture from the unit (both ^{3}He and ^{4}He), and then add mixture back in "pipefuls," using a segment of pipe that connects the dumps to the dilution path. About 10 pipefuls (roughly 50 cm^3 at 500 mbar and room temperature) provides 1 mW of cooling power and regulation to 10 mK at 1.5 K. The 6 K maximum temperature is only where the GRT calibration becomes unreliable. With proper thermometry, it might be possible to extend the useful temperature range in the refrigerator to 20 K, a factor of 1000 from minimum to maximum.

3.2.3 Electrical set-up

The measuring set-up in the refrigerator was designed to minimize extraneous electrical noise. The leads were 40 gauge copper wire made into ribbon cables. The cables were wrapped around heatsinking posts at the mixing chamber, and the refrigerator's 50 mK, 600 mK and 1.2K stages. Each lead was interupted at the loading slug by a 5 kΩ metal film resistor, which combined with the roughly 1 nF distributed capacitance of the leads to form a low-pass filter with measured cut-off frequency below 1 kHz. Shielded twisted-pair cables were used at room temperature to minimize pick-up further. All current supplies were homemade and battery powered, and the data were taken using X-Y chart recorders to reduce electrical noise. PAR 113s were used to amplify all dc signals. The dV/dI measurements were taken with a PAR 124 lock-in amplifier.

We made no special effort to reduce noise at frequencies above 1 GHz; in particular, we did not install microwave filters [Martinis, et al., 1987]. The measured attenuation at high frequency is still relatively high, a minimum of 60 dB for $f > 1$ GHz and more than 90 dB for $f > 10$ GHz.

Chapter Four

Experimental Results

In this chapter, we discuss our measurements of small-geometric-capacitance, large-normal-resistance Josephson junctions. We start with a description of the current-voltage characteristics (IVCs) in zero magnetic field. We present in section 4.2 the temperature dependence of the critical current I_c, the retrapping current I_r, and the anomalous low-voltage resistance R_0. In section 4.3, there is a discussion of novel IVCs that appear when a magnetic field, alone or in combination with an ac signal, is applied to the sample, and the Coulomb blockade effects that arise when the junction is driven normal by a large magnetic field. Finally, we summarize our major discoveries.

4.1 Current-voltage characteristics (IVCs)

Our main probe of the physics of the junctions in this report (see Table 4.1) is the current-voltage characteristic (IVC). We therefore begin this chapter by presenting an IVC typical of those we measured in our samples, and describing how our IVCs resemble and differ from those of "classic" junctions of larger dimensions.

Figs. 4.1 and 4.2 show the IVC for the sample with $R_n = 140\ \mathrm{k\Omega}$ at $T = 20$ mK, and definitions of the quantities used to characterize the IVC. At first glance, there is little to distinguish the curve from those of other high quality junctions. The IVC has a well defined critical current, I_c, where, as the magnitude of the bias current is increased, the voltage rises discontinuously from near zero to $2\Delta/e$, Δ being the superconducting energy gap. After this jump, as the current is increased further, the voltage remains at $2\Delta/e$ for a time, and then smoothly rolls over to a linear dependence, $V = IR_n$. The only hint of novelty in Fig. 4.1 is that $I_c \approx 400$ pA is greatly reduced below its unfluctuated value, $I_{c0} = 6.5$ nA.

Table 4.1: Parameters for various samples. R_n is the normal resistance. T_{min} is the lowest temperature at which data was taken for the sample. A is the area, measured by scanning electron micrograph. C is the geometric capacitance, determined by multiplying the area by the specific capacitance 25 fF/μm^2. E_J is tne Josephson coupling energy at $T = 0$, $h\Delta/8e^2R_n$. E_C is the charging energy, $e^2/2C$. N_{JJ} is the number of junctions in the sample.

Samples 1, 4, 14, and 16 had two junctions in series, one of which was much smaller than the other. The R_n and C listed are those of the smaller junction. Samples 7 and 8 were on the same substrate and shared a common electrode, but could be measured separately; samples 9 and 10 likewise. Sample 15 is one junction of a three junction sample, arranged as shown in Fig. 4.19.

Sample	R_n [kΩ]	T_{min} [K]	A [μm^2]	C [fF]	E_J [K]	E_C [K]	N_{JJ}
1	0.52	1.4	0.1	2	40	0.45	2
2	1.1	0.02	4	100	21	0.01	1
3	3.4	1.8	0.15	3	6.2	0.3	1
4	6.5	0.85	0.4	7	3.2	0.15	2
5	8.3	0.02	0.15	3.2	2.7	0.3	1
6	14.8	0.02	0.1	2.5	1.5	0.35	1
7	15.1	0.02	0.1	2.9	1.5	0.3	2
8	16.5	0.02	0.08	2	1.4	0.44	2
9	21.3	0.02	0.1	2.6	1.05	0.36	2
10	26	0.02	0.07	1.8	0.9	0.5	2
11	30	1.3	0.025	<1	0.7	>0.9	2
12	~30	0.02	0.1	2	0.7	0.45	11
13	34	0.02	0.1	2	0.6	0.45	1
14	70	0.02	0.04	1	0.3	0.9	2
15	74	0.02	0.04	1	0.3	0.9	3
16	110	0.02	0.05	1	0.19	0.9	2
17	140	0.02	0.05	1	0.15	0.9	1

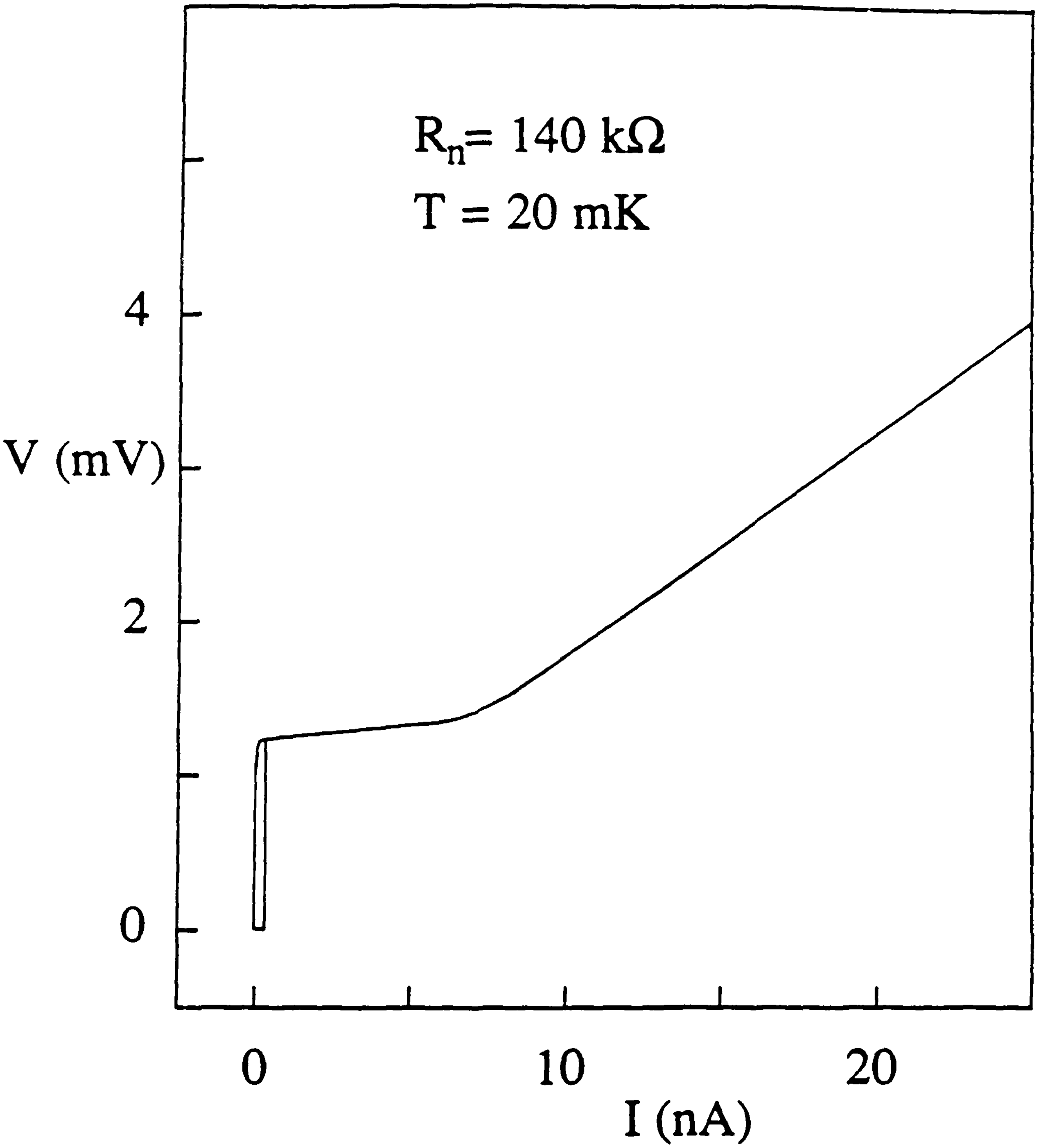

Fig. 4.1: Low temperature IVC for the sample with R_n = 140 kΩ. At this scale, the IVC appears the same as that for a large area junction, except for the strong suppression of I_c from its theoretical value $I_c(T = 0)$ = 6.5 nA.

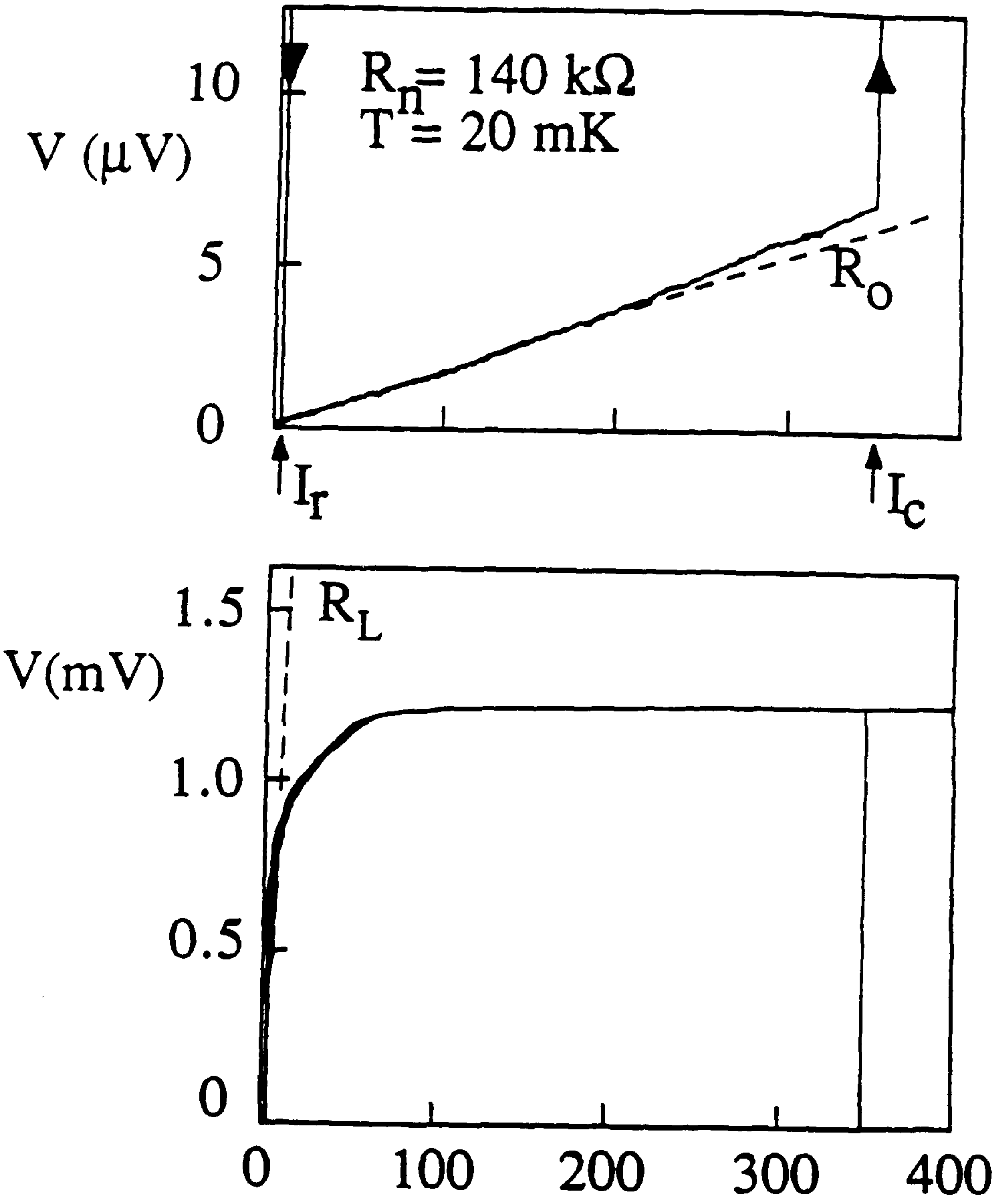

Fig. 4.2: Two IVCs for the sample with $R_n = 140\ \text{k}\Omega$, with the same current axis, but different voltage axes. The top voltage axis is expanded about 100 times relative to the bottom, revealing the low-voltage branch. The quantities I_c, I_r, R_O, and R_L are defined.

As shown in Fig. 4.2 (bottom), the IVC is hysteretic, with two stable voltage states when $I_r \leq I \leq I_c$. I_r is known as the "retrapping current," since, in the usual RCSJ washboard model, it is at this current that the motion of the phase point changes from the running state, with $d\varphi/dt = 2eV/\hbar > 0$, to the trapped state, in which φ is pinned by the washboard potential, and the voltage is zero. Once again, the hysteresis and the existence of the retrapping current are typical of the underdamped junctions of prior investigations.

The quasiparticle tunneling branch of the IVC is nearly ideal, with a sharp gap structure and large leakage resistance, R_L (Fig. 4.2, bottom). In fact, as we discuss in section 5.1, R_L in our junctions exhibits an ideal temperature dependence, $R_L \propto e^{\Delta/kT}$, as reflected by $I_r(T)$, until the combination of high-frequency loading of the junction and the dramatic onset of quasiparticle tunneling at $V = 2\Delta/e$ causes the retrapping current to become temperature-independent, making it impossible to infer the size of R_L.

How this IVC deviates from those of larger junctions, however, is apparent with closer inspection. Most dramatically, in Fig. 4.2 (top) we see, upon expanding the voltage scale 100 times, that our superconducting tunnel junction is not superconducting at all!

For currents $-I_c \leq I \leq I_c$, when an underdamped Josephson junction usually has V identically zero, our junctions have an observable $|V| > 0$. We call this part of the IVC a "low-voltage branch", to differentiate it from the "zero-voltage branch" of classic Josephson junctions. For small currents, we observe a linear $V(I)$, which we characterize by R_0, the differential resistance at $I = 0$. This new feature is now recognized as typical of small-geometric-capacitance, large-R_n junctions [Iansiti, et al., 1987a, 1987b, 1989a, 1989b; Ono, et al., 1987; Martinis and Kautz, 1989], and, as discussed in section 5.2, it has profound implications for potential models of the physics of these samples. In particular, the co-existence in the IVC of hysteresis and phase evolution on the low-voltage branch is incompatible with the standard RCSJ model, where the Josephson channel is shunted by a capacitor and a frequency-independent resistor.

4.2 Junction Characterization

We continue with a discussion of measurements of the main characteristic quantities of the junctions: I_c, I_r, and R_0.

4.2.1 The critical current I_c

The temperature dependence of I_c for a number of junctions is presented in Fig. 4.3. Starting from zero at T_c, I_c increases with decreasing T and reaches a maximum around $T = 3$ K. $I_c(T)$ then becomes reentrant and decreases to a degree which increases with increasing R_n. Finally, at roughly $T = 1.5$ K, I_c starts to increase again, at first gradually, but then at an increasing rate as the temperature drops below 300 mK. For most of the samples, the value of I_c at 20 mK is somewhat lower than its maximum value at high temperature. It is important to note that our junctions become non-hysteretic at high temperatures, as the IVC approaches that of a normal tunnel junction, $V = IR_n$. When the junction is non-hysteretic, we *define* the critical current as the point of intersection between the current axis and the line tangent to the IVC at its subgap inflection point.

Earlier work in this lab on large area junctions demonstrated that the ideal Ambegaokar-Baratoff relation [1963],

$$I_{co}R_n = \frac{\pi\Delta}{2e}\tanh\frac{\Delta}{2kT} \ , \tag{4.1}$$

holds to within 10 % for our samples, and, therefore, that $I_{c0}(T)$ is a monotonically decreasing function. In the RCSJ model, neglecting fluctuations, I_c, the *measured* critical current, is equal to I_{c0}, the "unfluctuated" critical current. Previous measurements by this group of $I_c(T)$ in large area junctions displayed this monotonic temperature dependence [Danchi, et al., 1984], even when $I_c(T)$ was suppressed below $I_{c0}(T)$ by thermal

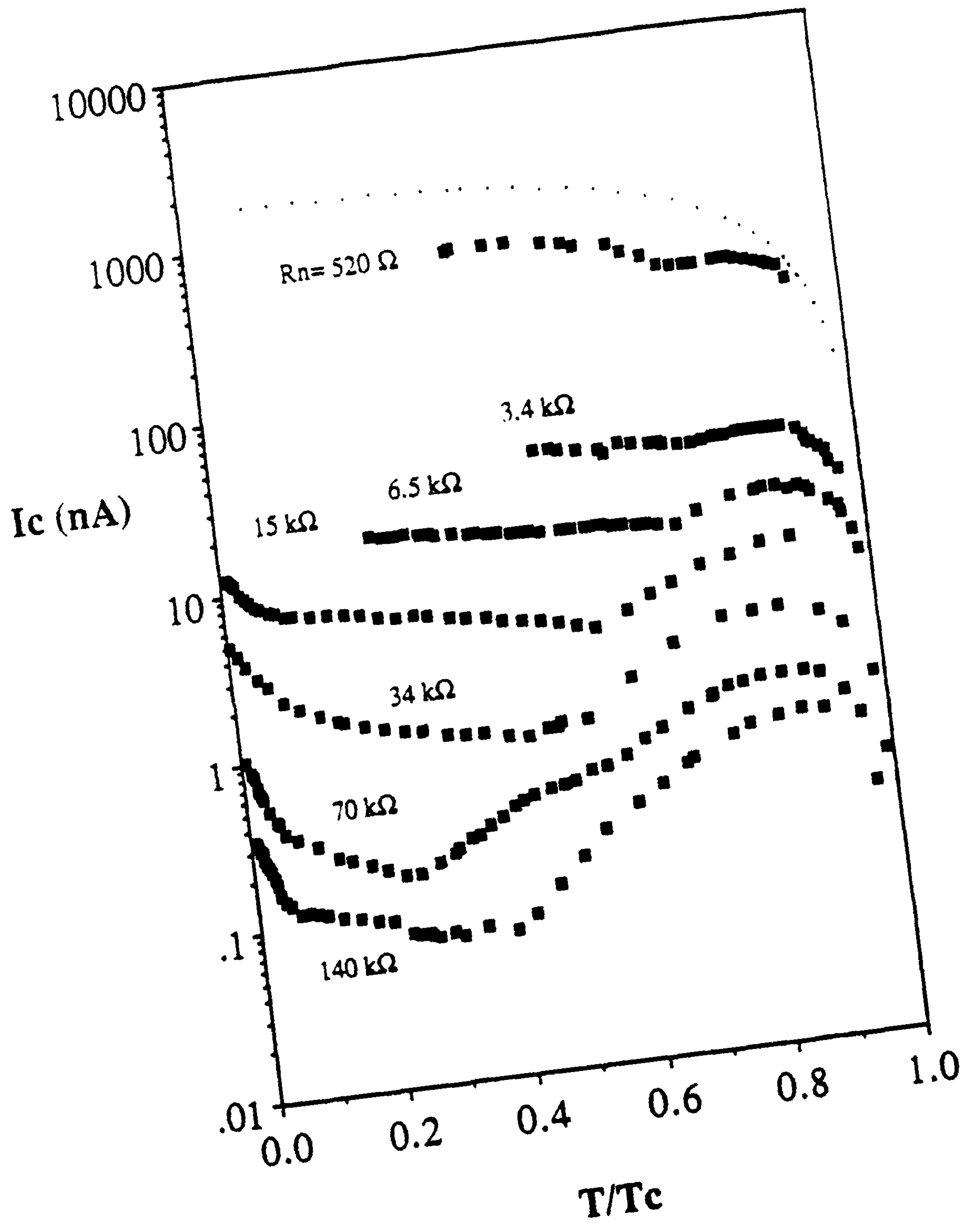

Fig. 4.3: $I_c(T/T_c)$ for seven samples of different normal resistance. The data are reentrant to a degree which grows with R_n. The dotted curve is $I_{c0}(T/T_c)$ for the sample with R_n = 520 Ω.

fluctuations [Fulton and Dunkleberger, 1974]. By contrast, $I_c(T)$ is reentrant for our samples, and more markedly so as R_n increases.

Finally, we note that the existence of phase evolution on the low-voltage branch of the IVC implies that I_c is determined by damping, which prevents runaway by the phase point (that is, switching to the gap voltage), despite the latter's frequent activation from the potential well. This is different from the case in larger junctions (with $R_0 = 0$), where I_c is determined by *fluctuations*, which activate the phase point from the potential well *once*, causing the junction to switch to the voltage state.

4.2.2 The retrapping current I_r

$I_r(T)$ for four samples is displayed in Fig. 4.4. Although there is not the regular dependence on R_n observed in the I_c data, the I_r data all behave similarly. As discussed below, aspects of this behavior are qualitatively different from those observed in measurements of large area junctions.

At high temperature, our junctions are non-hysteretic; I_c and I_r are identical. Starting from zero at T_c, both I_c and I_r increase, reaching a maximum around 3 K. Both then decrease dramatically. The junctions become hysteretic at 1.5-2 K. After this, as I_c increases, I_r continues to decrease rapidly (see Fig. 4.5). Finally, at $T \approx 0.9$ K, I_r reaches a minimum plateau.

Consider the data at temperatures where the IVC is non-hysteretic. Our junctions have damping parameter $Q_L = (2eI_{c0}CR_L{}^2/\hbar)^{1/2} > 1$ for all temperatures except very close to T_c, where $I_{c0}(T)$ is still nearly zero. For example, the sample with $R_n = 140$ kΩ has $T_c = 3.75$ K, and $Q_L > 1$ for all $T < 3.7$ K. In the absence of fluctuations, the IVCs would be hysteretic. The IVCs are non-hysteretic because of thermal fluctuations, which nearly continuously activate the phase out of the potential well.

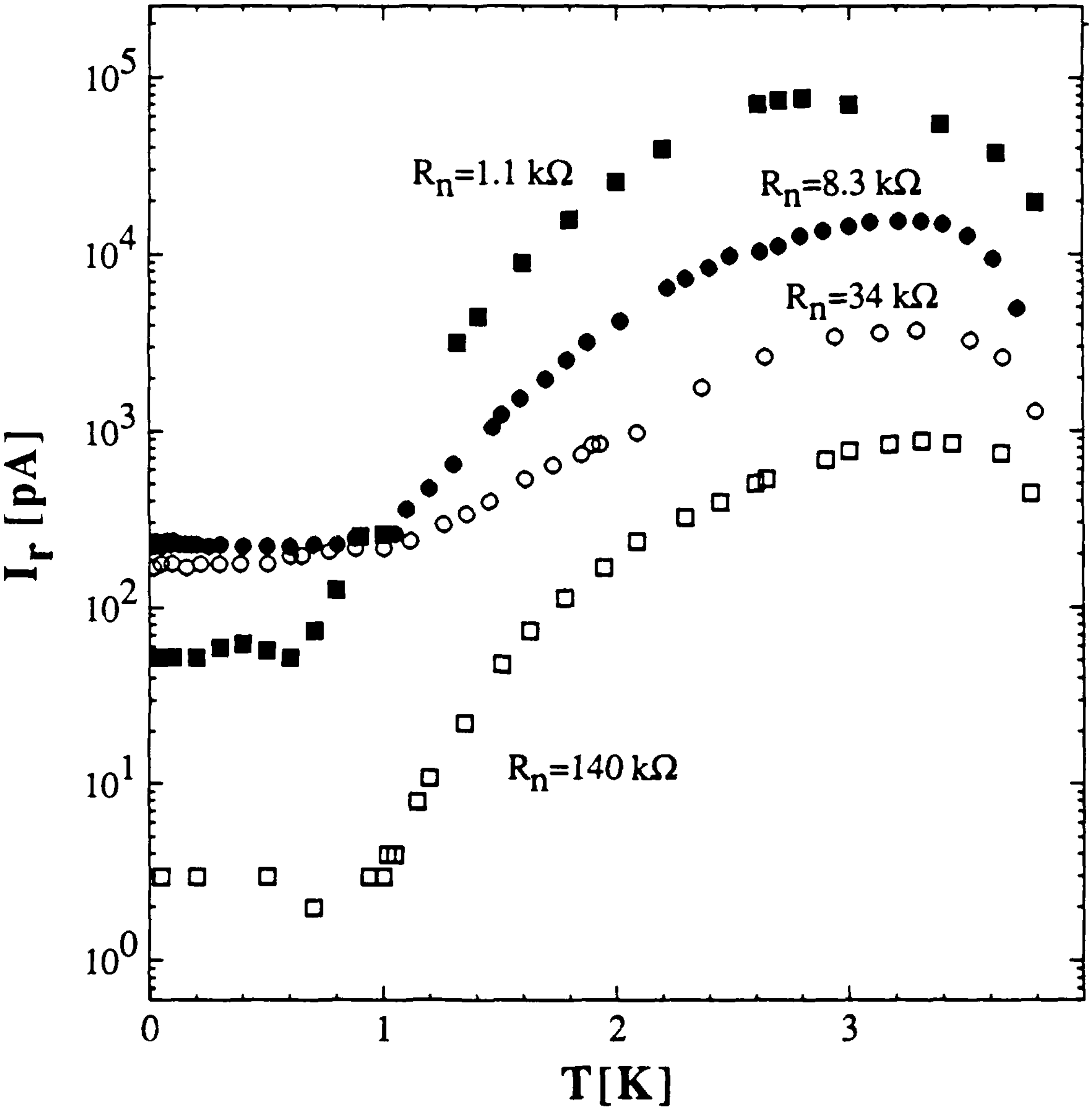

Fig. 4.4: $I_r(T)$ for four samples. The dependence of this data is less systematic with R_n than the $I_c(T)$ data (Fig. 4.3). In particular, note that the low-temperature limit of I_r is not a monotonic function of R_n.

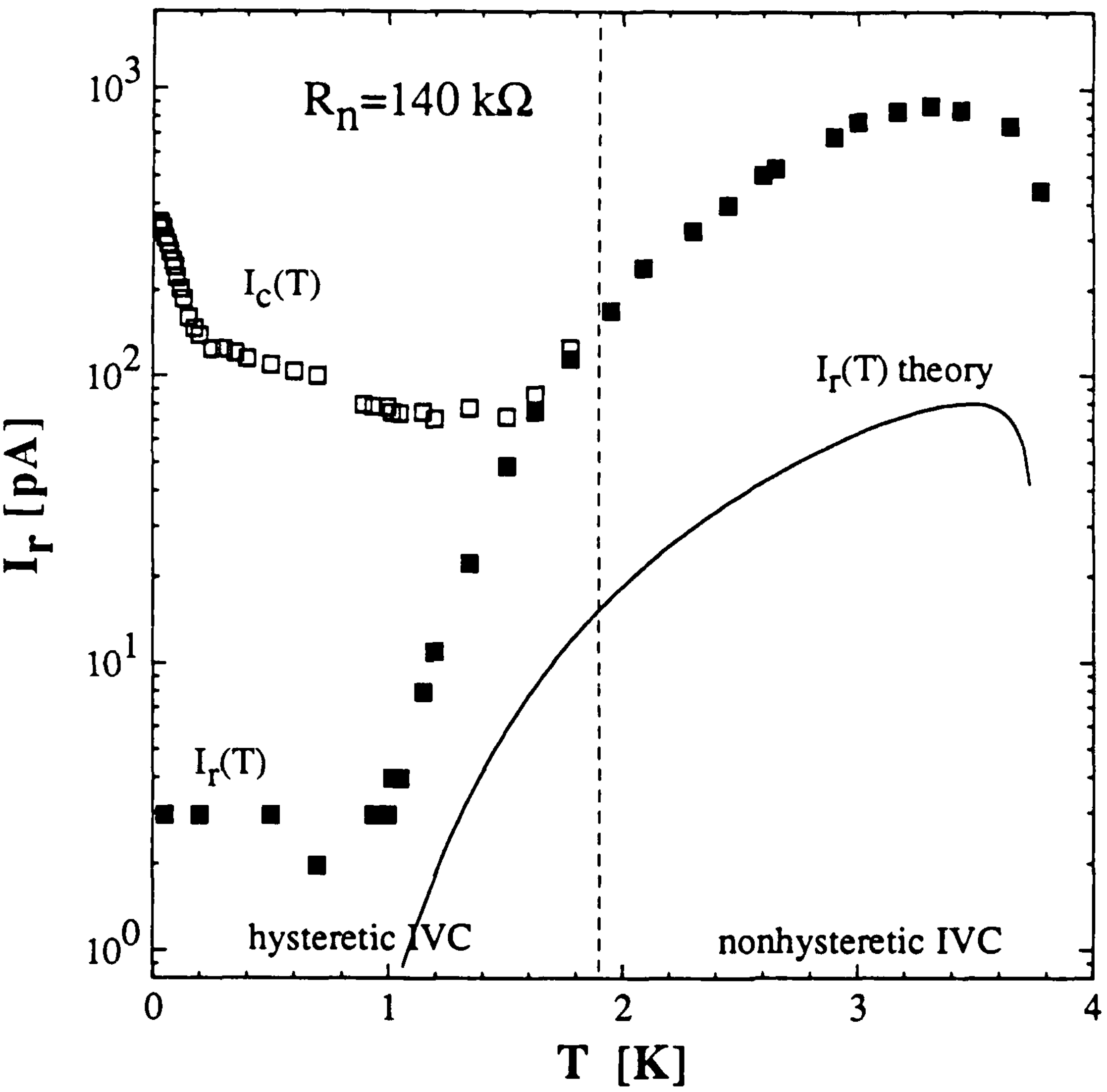

Fig. 4.5: $I_c(T)$, $I_r(T)$, and theory for the sample with R_n = 140 kΩ. The theory deviates from the data for reasons explained in the text. The theory's proper T dependence for 2 K < T < T_c indicates that it is the physics of I_r that determines both I_c and I_r in the non-hysteretic region (to the right of the dashed line).

Fig. 4.6 (a) shows schematically the IVC predicted by the RCSJ model for an underdamped junction in the absence of fluctuations. The addition of large fluctuations‡ changes the IVC in the following manner. For $I < I_{r0}$, the unfluctuated retrapping current, the running state does not exist. If the phase point is activated out of the well, it will be retrapped after traversing some (usually small) number of wells. There will be a dc voltage, since $d\varphi/dt > 0$, but it will be small.

Once I exceeds I_{r0}, however, the situation changes dramatically. The running state now exists. If φ is activated from a potential well, it may be retrapped or escape to the running state. Activation from the running state to the trapped state is also possible [Ben-Jacob, et al., 1982]. The voltage will be an average of the running-state voltage and zero, the voltage of the trapped state, weighted by the amount of time spent in each state. Before I is significantly greater than I_{r0}, it is plausible that the phase point will be in the running state most of the time, and that the voltage will be nearly $2\Delta/e$. The measured "critical current" in this case, i.e. the current at which the voltage rises most sharply, will be roughly I_{r0}. This value is a lower bound; the precise value will depend upon details of the lifetimes of the running and trapped states as functions of I.

When the junction IVC is non-hysteretic, then, the physics of the retrapping current determine both I_c and I_r. If we can understand I_r in this temperature range, then we understand I_c as well. Our samples' measured maximum in $I_r(T)$ is, in fact, in accord with the standard RCSJ model. Clearly, $I_r(T_c) = 0$. As we review in the next paragraph, I_r decreases with decreasing T at low T. Therefore, $I_r(T)$ must have a maximum at some intermediate temperature.

---

‡ The fluctuations need to be large enough to destroy the hysteresis, but not so large that the picture of a system evolving in phase space with noise as a perturbation upon its dynamics is inapplicable. The presence of extremely large fluctuations, for example, makes a discussion of trapped and running "attractors" moot. The influence of the potential in that case is negligible.

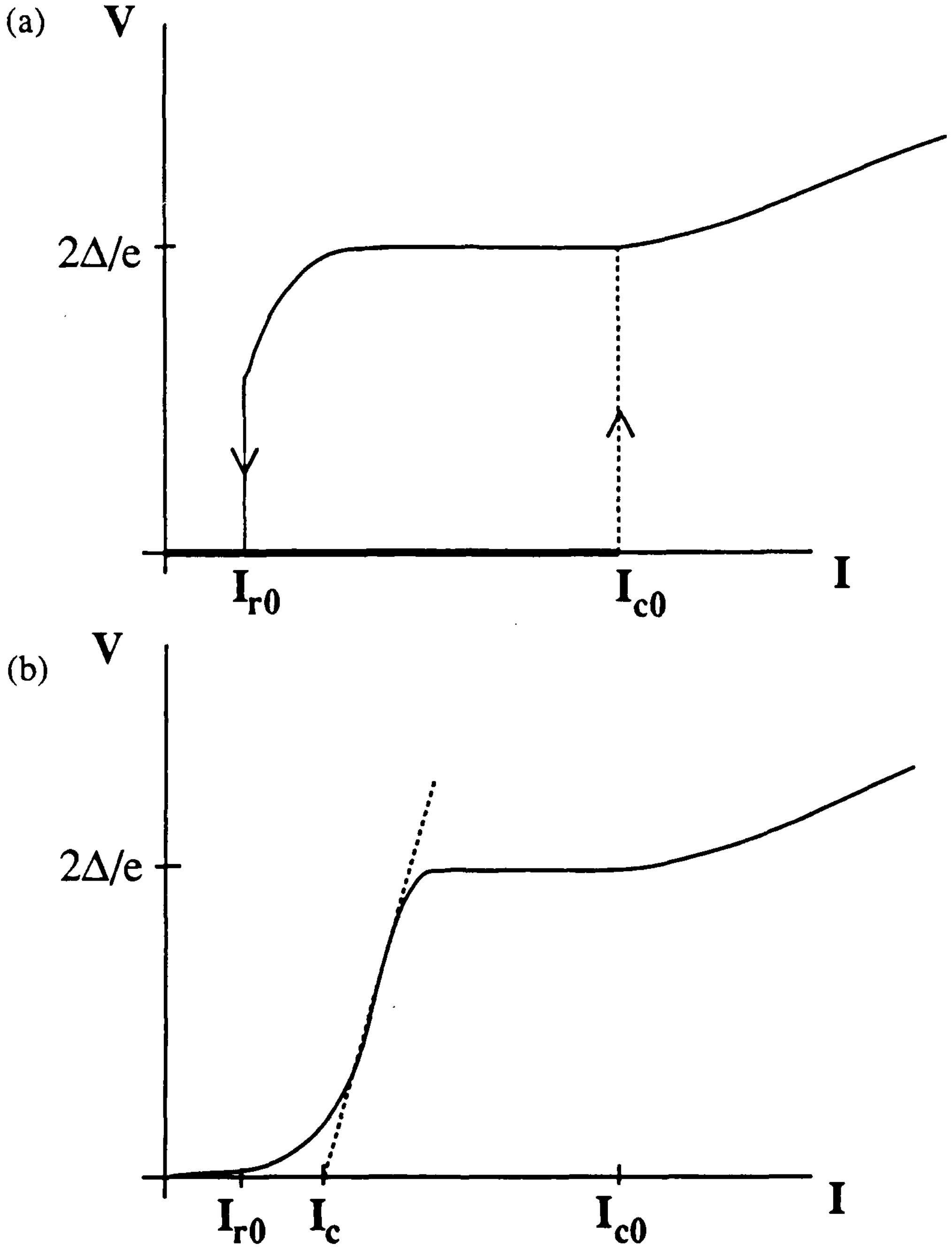

Fig. 4.6: A diagram of the effect of large fluctuations on the IVC of an underdamped junction in the RCSJ model. (a) the IVC in the absence of fluctuations. The voltage rises discontinuously to the gap at I_{c0}, and returns to zero at I_{r0}. (b) large fluctuations smear out the IVC. As discussed in the text, the maximum in dV/dI occurs at a current equal to or greater than I_{r0}. Using our definition of I_c for a nonhysteretic IVC, described in the text, we find a value of I_c not too different from I_{r0}.

In the standard RCSJ model, I_r depends upon the resistor in parallel with the Josephson channel, $I_r \propto 1/R$. The shunting resistor in our junctions is a quasiparticle tunneling channel. As T decreases, quasiparticle excitations freeze out in the superconducting electrodes. The effective resistance presented by this channel, inversely proportional to the number of quasiparticles available to tunnel, should increase at low temperature as $e^{\Delta/kT}$ [Iansiti, et al., 1985], and $I_r(T)$ should decrease accordingly.

Along with the $I_c(T)$ and $I_r(T)$ data, Fig. 4.5 shows the retrapping current predicted by the standard RCSJ model in the absence of fluctuations, $I_{r0}(T) = 4I_{c0}(T)/\pi\omega_p R_L C$ [Ben-Jacob, et al., 1982]. Although the absolute agreement with the data is poor, the *shape* of the theory is correct for $T > 1$ K. In this temperature range, the data clearly display the $e^{\Delta/kT}$ dependence of the leakage resistance. This resemblance is evidence that, in the nonhysteretic region, $I_c(T)$ is determined by the physics of $I_r(T)$, that is the onset of bistability in the system's unfluctuated dynamics.

The data in Fig. 4.5 are systematically greater than the predictions of theory, due to two effects that are neglected. The first, discussed briefly above, is that in the non-hysteretic regime, I_{r0} is only a lower bound for I_c. The second is the low impedance presented by the leads at high frequency, which, we argue in section 5.1, increases I_{r0}, the unfluctuated retrapping current.

What is truly novel about the $I_r(T)$ data is the low-temperature minimum plateau. As described above, the standard RCSJ model predicts that $I_r \propto 1/R$, so that we expect I_r to vanish exponentially as $T \rightarrow 0$, due to the freeze-out of the quasiparticle shunt. The observed plateau is a marked deviation from this prediction.

This unexpected plateau is the focus of section 5.1. We argue there that to understand these data, we must add to the RCSJ model the onset of pair-breaking quasiparticle tunneling at $V = 2\Delta/e$ and the low impedance presented by the leads at high frequency. A typical transmission line impedance is 100 Ω, much less than R_L for our junctions at low T. This has little influence upon the IVC of large area junctions, since the line impedance is shorted out by the junction's capacitance and its low resistance, except at very low T, where R_L is large. In high resistance samples, the effect of the low line impedance at high frequency is to increase I_r and V_r, the voltage at retrapping, above their values in the absence of leads. Eventually, as T decreases, freezing out ever more quasiparticles, the junction retraps from $V_r \approx 2\Delta/e$. In section 5.1, we present an argument based on energy conservation, that once the junction retraps from this level, and V_r is unable to rise any higher because of the large current onset at $2\Delta/e$, I_r is constant for any lower temperature. The combination of the low impedance presented by the leads at high frequency, and the onset of pair-breaking tunneling at the gap voltage is, therefore, responsible for the plateau in $I_r(T)$.

4.2.3 The low-voltage branch resistance R_0

We show $R_0(T)$ for a number of samples in Fig. 4.7. For all the samples, R_0 is a monotonically increasing function of temperature. However, the samples may be divided into two catagories based on the behavior of R_0. In samples 1, 2, and 3 ($R_n = 500\ \Omega$, 1.1 kΩ, and 3.4 kΩ, see Table 4.1), $R_0(T)$ decreases rapidly below our experimental resolution once $T < T_c$. They are identical to the "classic" samples of earlier work.

Samples with large R_n behave differently. R_0 is non-zero down to the lowest temperatures attainable by our dilution refrigerator. The samples with the largest normal resistance (samples 16 and 17) have R_0 roughly equal to R_n over a large range of T, and show a sharp decrease in R_0 only at low temperatures. The onset of rapid decrease occurs roughly at the temperature where E_J becomes equal to kT (see Fig. 4.8).

This marked difference between samples of low and high R_n, with a crossover value of $R_n \approx$ 1-10 kΩ, is similar to that observed in studies of superconducting granular films. In those experiments [Orr, et al., 1986], samples with $R_n > 6$ kΩ were insulating at low temperature, while those with $R_n < 6$ kΩ were superconducting. Our data are evidence for the $T = 0$ phase transition predicted to occur in Josephson junctions as the

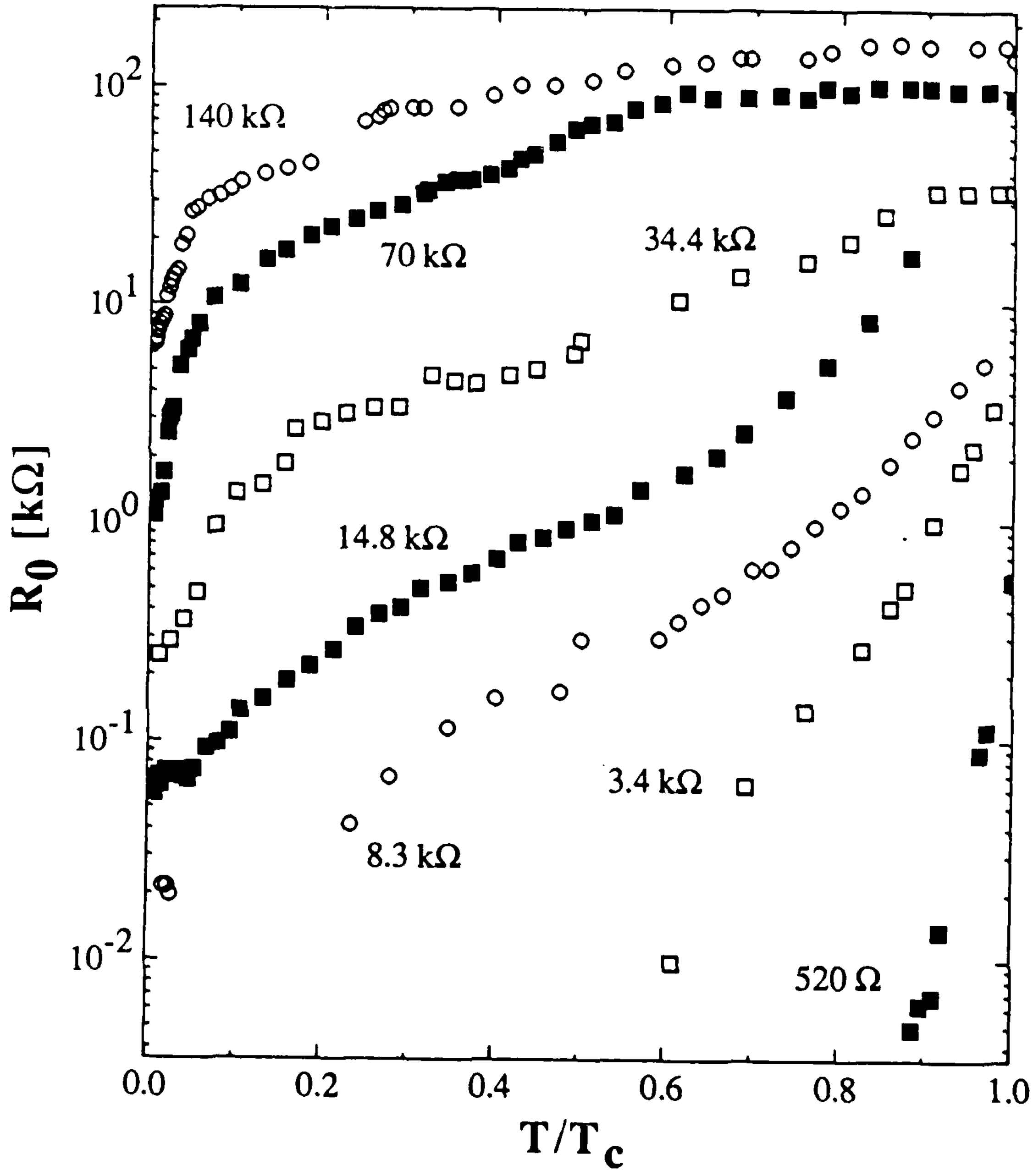

Fig. 4.7: $R_0(T/T_c)$ for seven samples. The low temperature R_0 for the samples with $R_n = 520\ \Omega$ and 3.4 kΩ is below the sensitivity of our instruments.

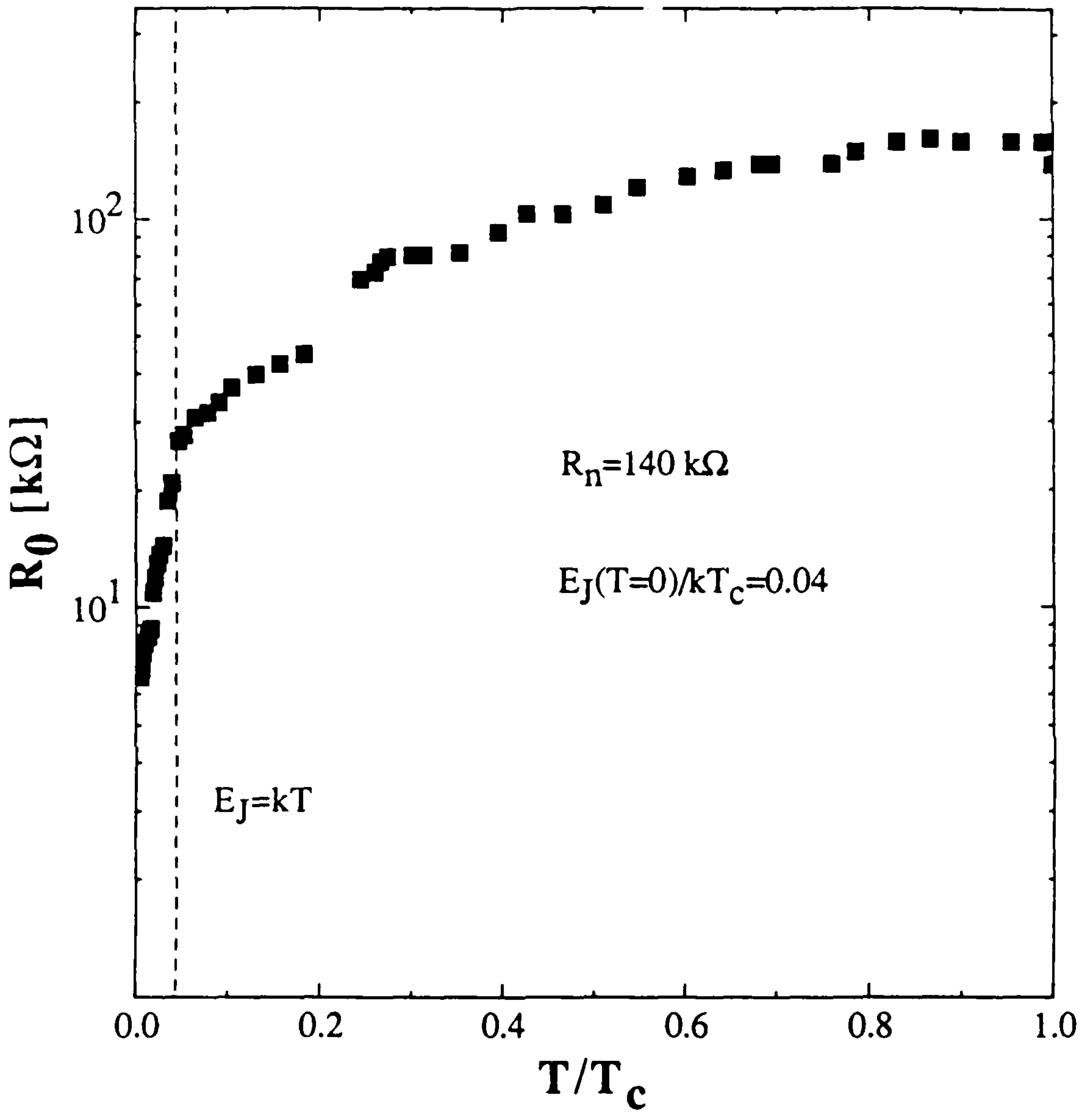

Fig. 4.8: $R_0(T/T_c)$ for the sample with R_n = 140 kΩ. The sharp break in the data occurs roughly when $kT = E_J(T)$, marked by the dashed line.

quasiparticle dissipation increases. According to the theory outlined in section 2.6, quasiparticle tunneling flattens the junction's energy band structure (see Fig. 2.9). As the bands become flatter, the voltage expectation value, $<V> = (2e/\hbar)<d\varphi/dt> = dE/dq$, decreases, leading to a lower R_0.

4.3 Effect of applied magnetic field

As discussed in Chapter 2, quantum mechanical fluctuations of the phase are predicted to be most evident in samples with $E_J/E_C << 1$. Our samples (see Table 4.1) have E_J/E_C ranging from 0.2 to 200. A magnetic flux parallel to the oxide barrier of a tunnel junction modulates the maximum supercurrent [Tinkham, 1975, p. 199]. In a junction with uniform critical current density, and at fields so small that the energy gap is unaffected, I_{c0} varies as

$$I_{c0}(H) = I_{c0}(0)\frac{\sin(\phi / \phi_0)}{\phi / \phi_0} , \tag{4.2}$$

where ϕ is the flux threading the barrier and $\phi_0 = h/2e$ is the superconducting flux quantum. Changing the field, therefore, tunes the Josephson coupling energy, letting us cover a range of E_J/E_C with a single sample. This technique has been used in experiments studying MQT and chaos in Josephson junctions [Devoret, et al., 1985; Hu, et al., 1987].

In Fig. 4.9, we show $I_c(H)$ for sample 5, $R_n = 8.3$ kΩ. The data have several local minima, whose period implies that $2\lambda+t = 140$ nm, where λ is the penetration depth and t is the barrier thickness. Assuming $t = 2$ nm yields $\lambda \approx 70$ nm, a reasonable value. The field dependence is not the ideal one given in (4.2). One reason is the reduction of the energy gap caused by the large field needed to thread one flux quantum through the junction. A second is that our overlap junctions are not strictly planar, so the field is not

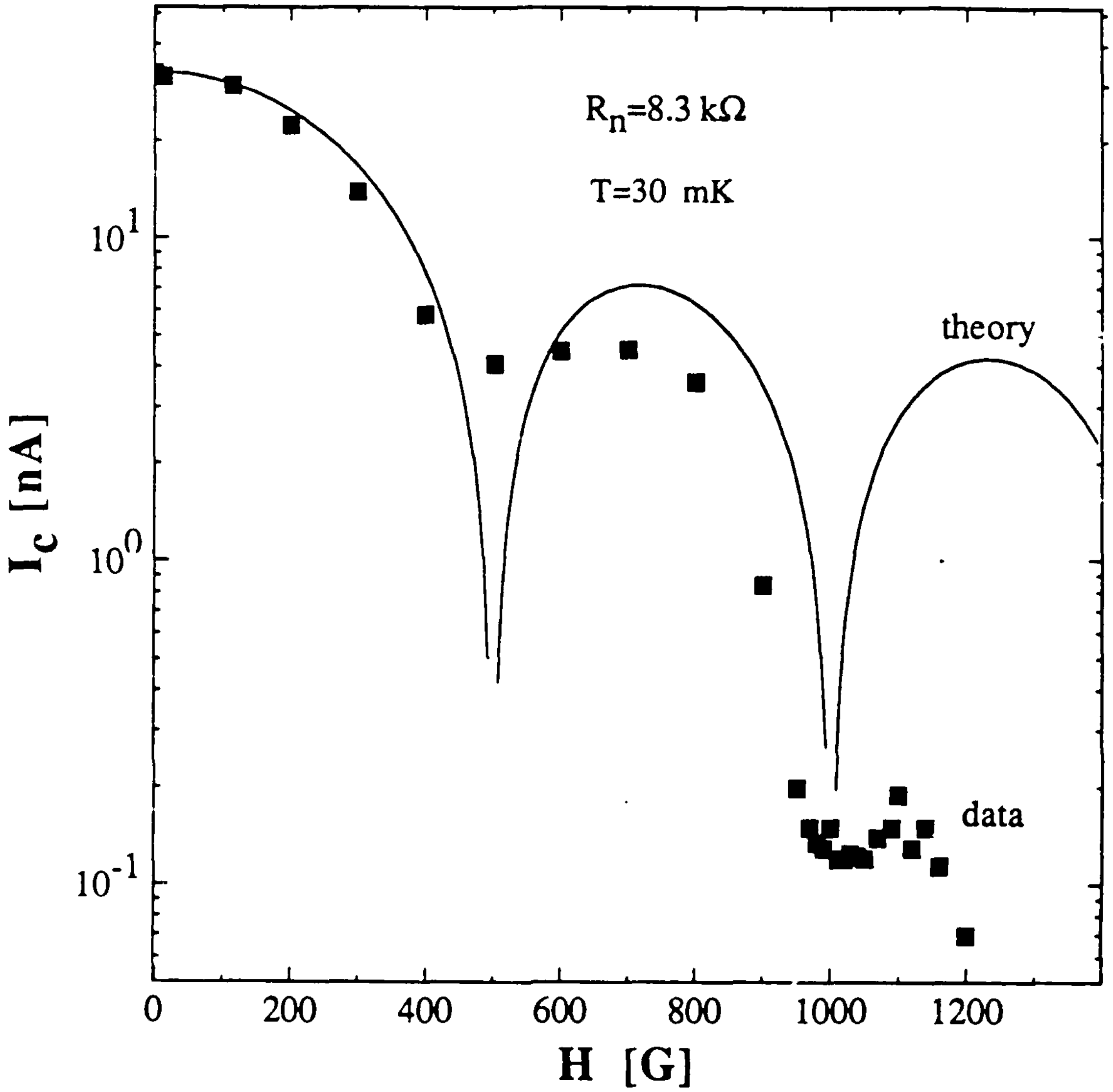

Fig. 4.9: A graph of $I_c(H)$, data and theory, for the sample with R_n = 8.3 kΩ. The reasons for the poor fit are discussed in the text.

parallel to the barrier over the whole junction area. Third, in these small samples, the measured I_c is related to, but not equal to, the unfluctuated critical current I_{c0}. If the ratio $I_c(H)/I_{c0}(H)$ is a function of field, then the measured $I_c(H)$ will deviate from the $\sin x/x$ theory. Finally, some degree of non-uniformity is expected in the barrier, leading to a non-ideal $I_c(H)$.

4.3.1 Intermediate fields: novel IVCs

We have observed several novel IVCs in junctions with E_J reduced by an applied magnetic field.

The first example of a surprising, field-induced feature on an IVC is the curve labeled "0.175 T" in Fig. 4.10. The curve is hysteretic, and the low-voltage branch displays a non-linear structure first reported by Iansiti, et al. [1988], and which strongly resembles a feature observed in IVCs of arrays of superconducting tunnel junctions in experiments done elsewhere [Geerligs and Mooij, 1988].

Starting at $I = 0$, the voltage rises quickly, appearing to follow the quasiparticle branch, and then rolls over to a gentle ramp with dV/dI of order megohms. As in samples measured in zero field, the IVCs are hysteretic, with a discontinuous switch to the field-reduced gap voltage.

At low field, the IVC is identical to that in Figs. 4.1 and 4.2. The first evidence of new behavior is a region near I_c where a voltage step develops just before the jump to the gap (the IVC labeled "H = 0.143 T" in Fig. 4.10). Once this occurs, the step moves in to the origin over a mere 300 G. Whenever the step appeared, its height was roughly equal to $e/2C$ for that junction, suggesting the influence of charging energy effects. Increasing the field further causes the hysteretic region to shrink. Finally, the hysteresis disappears, and the step is absorbed in the quasiparticle characteristic.

A similar evolution occurs when the temperature is used to change E_J. A progression of IVCs at different temperatures is shown in Fig. 4.11. The field has

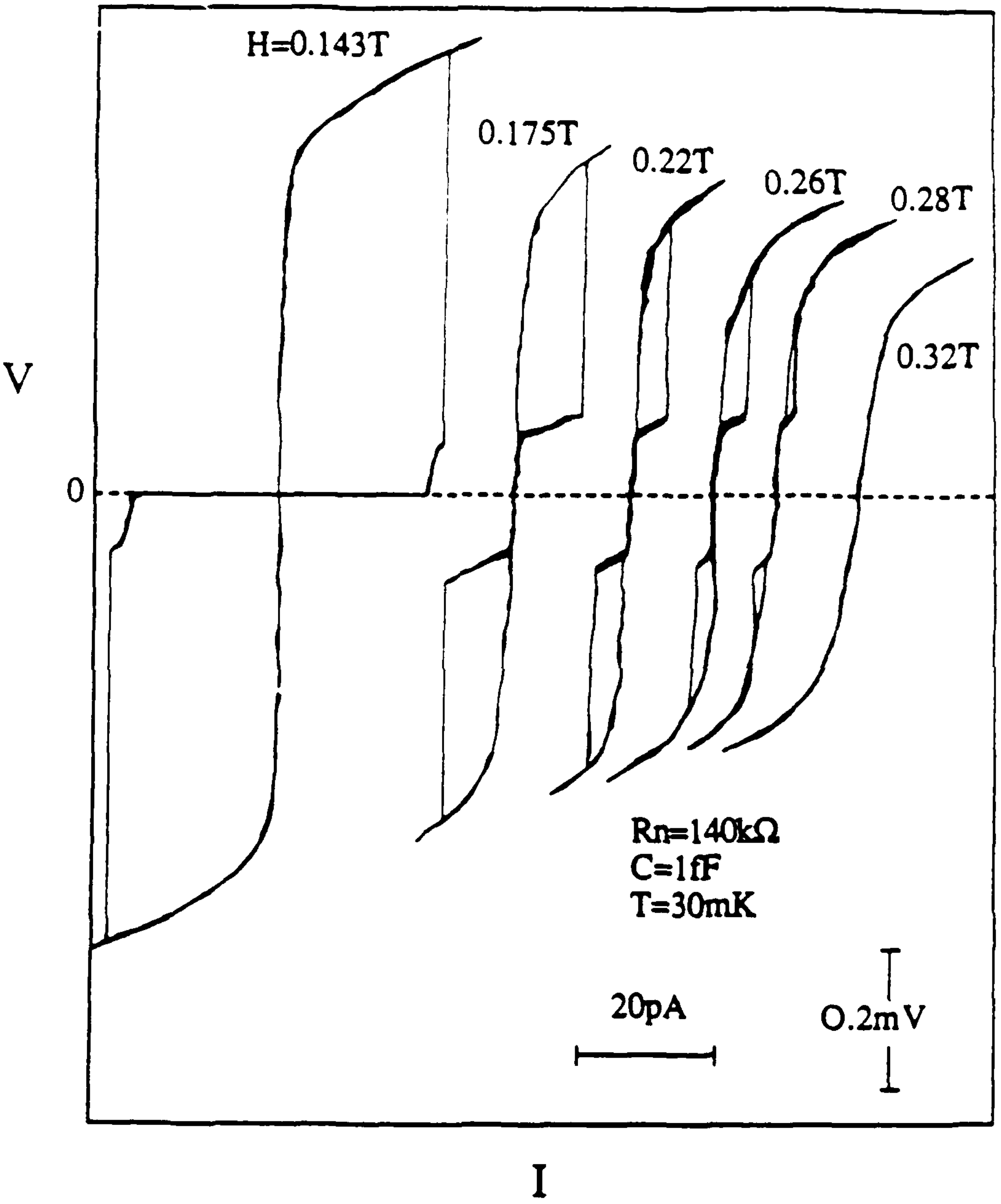

Fig. 4.10: Six IVCs of the 140 kΩ sample taken at constant temperature and different magnetic fields. The step that develops on the low-voltage branch has a height of 100 ± 20 μV, roughly equal to $e/2C = 80\ \mu V$ for this junction.

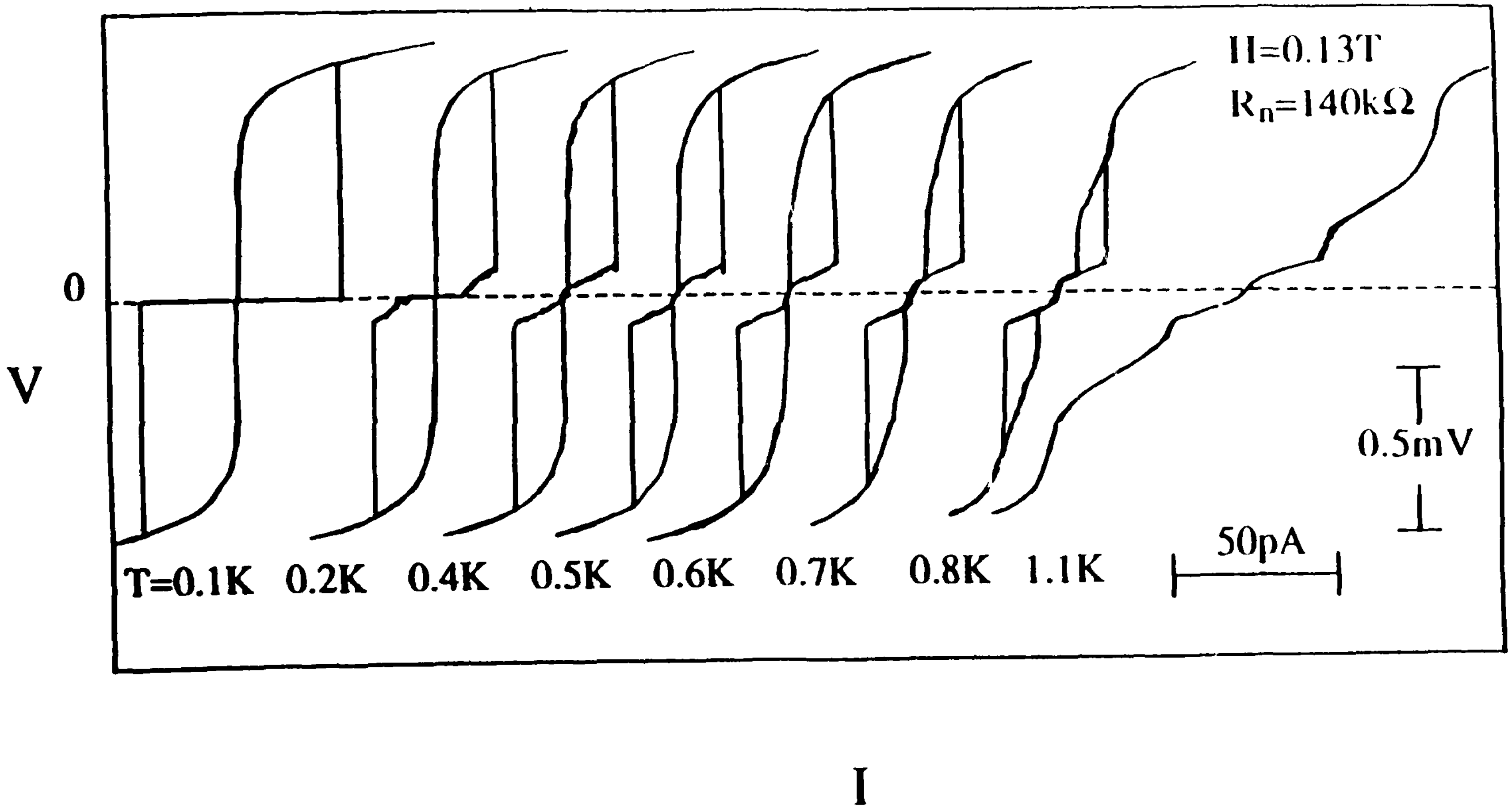

Fig. 4.11: IVCs for the sample with R_n = 140 kΩ, at constant magnetic field and different *T*. The height of the step on the low-voltage branch is independent of *T*.

suppressed this junction's T_c to about 1.5 K, so $I_{c0}(T)$ changes drastically over the temperature range covered. The size of the voltage step does not change with temperature. For this series of curves, in contrast to Fig. 4.10, we have not only a declining E_J, but also increasing fluctuations, as T is increased. Tuning E_J with the field avoids this complication.

4.3.2 Intermediate fields and an applied ac signal

In chapter 2, we described the Bloch oscillations predicted to occur in junctions where quantum mechanical fluctuations of the phase are not negligible. Likharev and Zorin [1985] predicted that these oscillations could phase lock to an applied ac field, producing current steps on the IVC, just as voltage steps are created by phase-locking of Josephson oscillations. With this inspiration, we took IVCs in the presence of an ac electric field. As detailed in the next few paragraphs, we did *not* observe current steps.

We applied an ac signal to the junction by exciting a wire, which ended in a copper plate beneath the sample substrate. This wire is part of the ribbon running down the refrigerator which also contains the junction current and voltage leads. The ac coupling is through the fields produced by the plate and also the capacitance between the signal wire and the junction leads. This capacitance is probably around 100 pF, which at the frequencies used (100-800 MHz) has an impedance of 2-20 Ω. R_n, R_L, $1/\omega C$ and $\omega L_J = \hbar\omega/2eI_{c0}$ are all far larger than this, so the sample is probably ac voltage-biased.

This coupling scheme is uncalibrated. All power values given in Figs. 4.12, 4.13, and 4.14 are measured at the source and are, therefore, only significant relative to one another. Due to losses in the ribbon, the power delivered to the junction was small, and the IVC of the sample in zero magnetic field barely changed. Because of this, we combined the ac field with a dc magnetic field. The latter reduced E_J to the point where the small ac signal had a significant impact upon the IVC. As pictured in Fig. 4.12, the effects were dramatic.

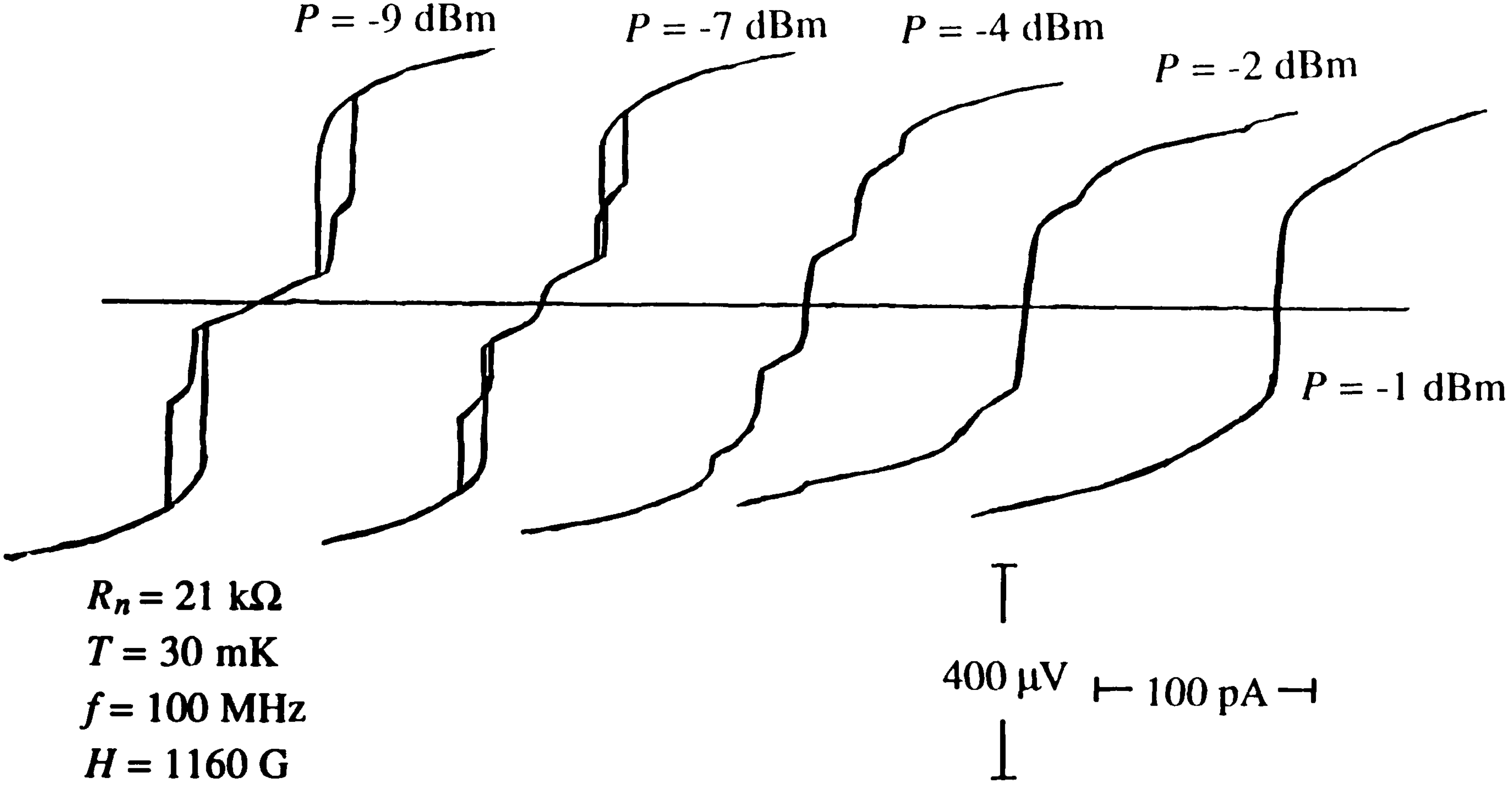

Fig. 4.12: IVCs from the sample with $R_n = 21$ kΩ, at constant T and H, but different applied 100 MHz power. First, a voltage step appears near I_c (in contrast with Fig. 4.1, where the step begins at the origin). As the ac power increases, another step is created at the origin. This second step moves to larger voltage with increasing ac power. Eventually both steps are absorbed by the gap structure (P = -1 dBm).

At low power levels, the ac signal decreased the hysteresis in the IVC and increased R_0, the slope of the low-voltage branch. At -9 dBm input power, the still-hysteretic IVC develops a "step" near I_c. The curve is similar to that observed in the case of an applied dc magnetic field only (Fig. 4.10, "$H = 0.143$ T"). Upon increasing the power further, rather than having the step move in to the origin as in Fig. 4.10, a second step appears at the origin and grows. The first step is pushed to larger currents and voltages and is eventually absorbed into the gap structure. At still higher power levels, the second step grows, to the point where it too is absorbed into the gap structure.

For other samples, the progression was slightly different (see Fig. 4.13). A step would appear at the origin and then begin to grow, without having the stage where one was present near I_c. A second, smaller step would appear near I_c at higher power levels ($P \approx -1$ dBm).

If we interpret these as "current" steps, they have a spacing of about 25 pA. Steps due to phase-locking to Bloch or SET oscillations at 100 MHz should appear at $I = 2ef = 32$ pA or $I = ef = 16$ pA, respectively. Although these do not differ greatly from the observed value, we can be certain that the steps are not due to Bloch oscillations, since they do not depend upon the frequency of the ac field. This is demonstrated in Fig. 4.14, where the source frequency is now 800 MHz, compared to 100 MHz in Figs. 4.12 and 4.13, but the scale of the steps is unaffected. The lack of a frequency dependence also rules out the possibility that these are Shapiro steps. The steps move in response to the ac *power*. The only difference between the evolution in Figs. 4.12 and 4.14 is that more power is needed in the latter to produce a curve of the same shape. This is probably due to less efficient coupling of the 800 MHz signal down the refrigerator to the sample.

4.3.3 Large magnetic fields: N-I-N tunneling

A large magnetic field drives the junction electrodes normal. We can then compare the properties of the samples with predictions from theories of tunneling in low-capacitance

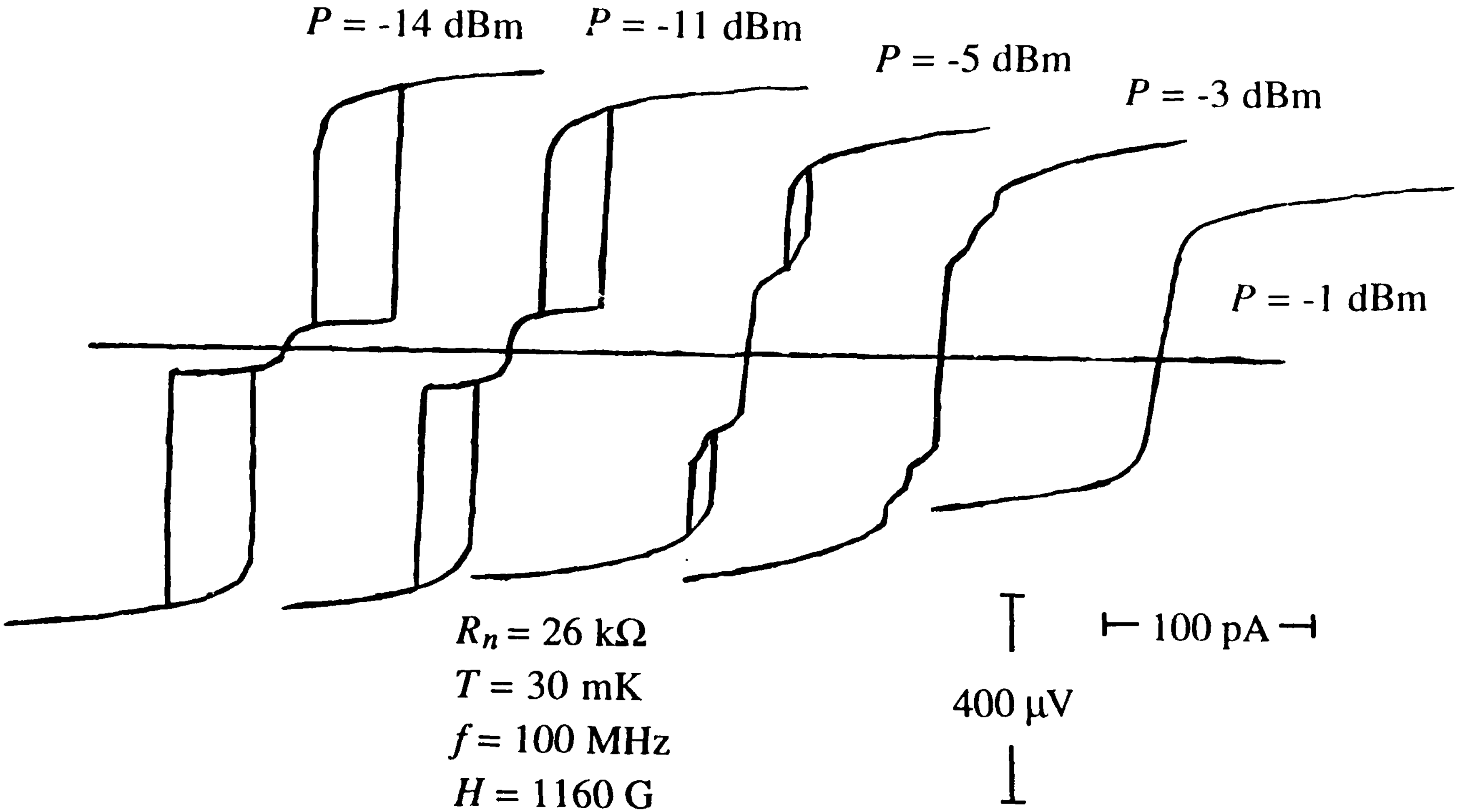

Fig. 4.13: IVCs for the sample with $R_n = 26$ kΩ, at constant temperature and dc magnetic field, and different applied 100 MHz power. A voltage "step" appears near the origin, and moves to larger voltage as the ac power increases. This is in contrast to the step that appears near I_c in Fig. 4.12. A hint of a second step is evident in the IVCs with $P = -5$ dBm and $P = -3$ dBm.

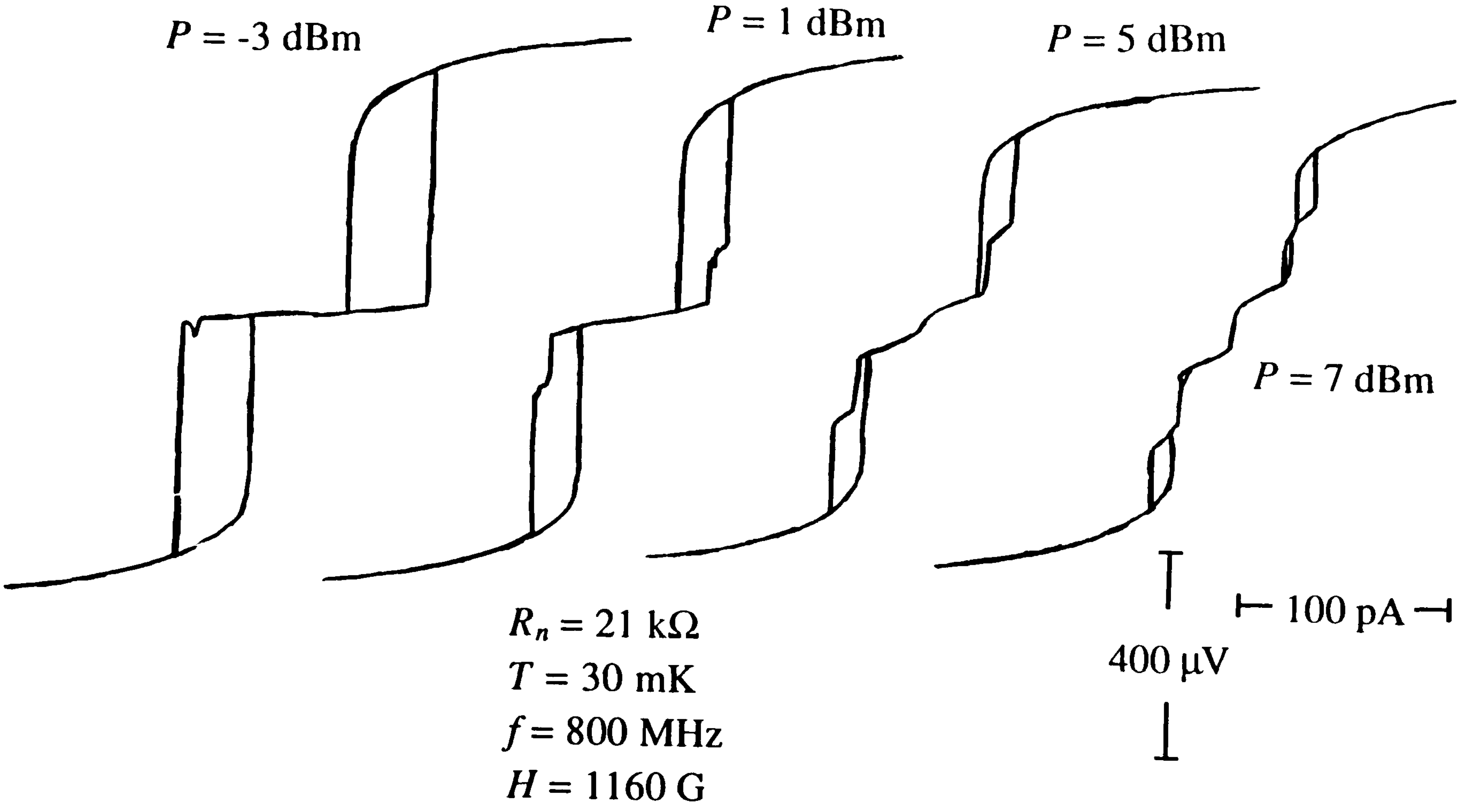

Fig. 4.14: IVCs for the sample with $R_n = 21$ kΩ, at constant temperature and dc magnetic field, and different levels of applied 800 MHz power. The IVCs look similar to those in Fig. 4.12, where the junction is driven with a 100 MHz field.

normal junctions. As detailed in the next few paragraphs, we see qualitative agreement with these theories.

The parallel critical field $H_{c\parallel}$ of a superconducting film can be greatly enhanced relative to the bulk H_c. Ginzburg-Landau theory yields [Tinkham, 1975, p. 124]:

$$H_{c\parallel} = 2\sqrt{6}\frac{\lambda}{d}H_c \ , \tag{4.3}$$

where λ is the penetration depth and d is the film thickness. The bulk critical field of tin is $H_c = 305$ G, while the samples had $d \approx 70$ nm and $\lambda \approx 70$ nm as determined from the minima in the measured $I_c(H)$. From (4.3), $H_{c\parallel} = 1500$ G, in reasonable agreement with the observed parallel critical field of roughly 3000-5000 G.

At large fields, our IVCs display slight deviations from the linear form predicted for a normal junction in the $C = \infty$ limit. As shown in Fig. 4.15, the curves had an increased value of dV/dI at small currents, and an excess voltage when extrapolated back to the origin from large currents and voltages. Fig. 4.16 is a plot of the extrapolated gap voltage V_g versus magnetic field for a sample with $C = 3.2$ fF ($R_n = 8.3$ kΩ). For small fields, $V_g(H)$ has the strong field dependence appropriate for the superconducting energy gap. At higher fields, $V_g(H)$ is independent of H, due to a crossover to the Coulomb blockade. The residual gap, 22 μV, is in good agreement with the theory of Averin and Likharev [1986], $V_g = e/2C = 25$ μV.

In a single junction connected directly to leads, the Coulomb blockade should be washed out even at $T = 0$ compared to the $I \propto V^2$ dependence predicted in the absence of long leads [Averin and Likharev, 1986], although the total excess voltage is preserved. The quantum mechanical nature of the electromagnetic environment causes charge fluctuations on the junction capacitor, even at $T = 0$ [Cleland, et al., 1990; Devoret, et al., 1990]. These fluctuations allow electrons to tunnel at low applied voltage, a process

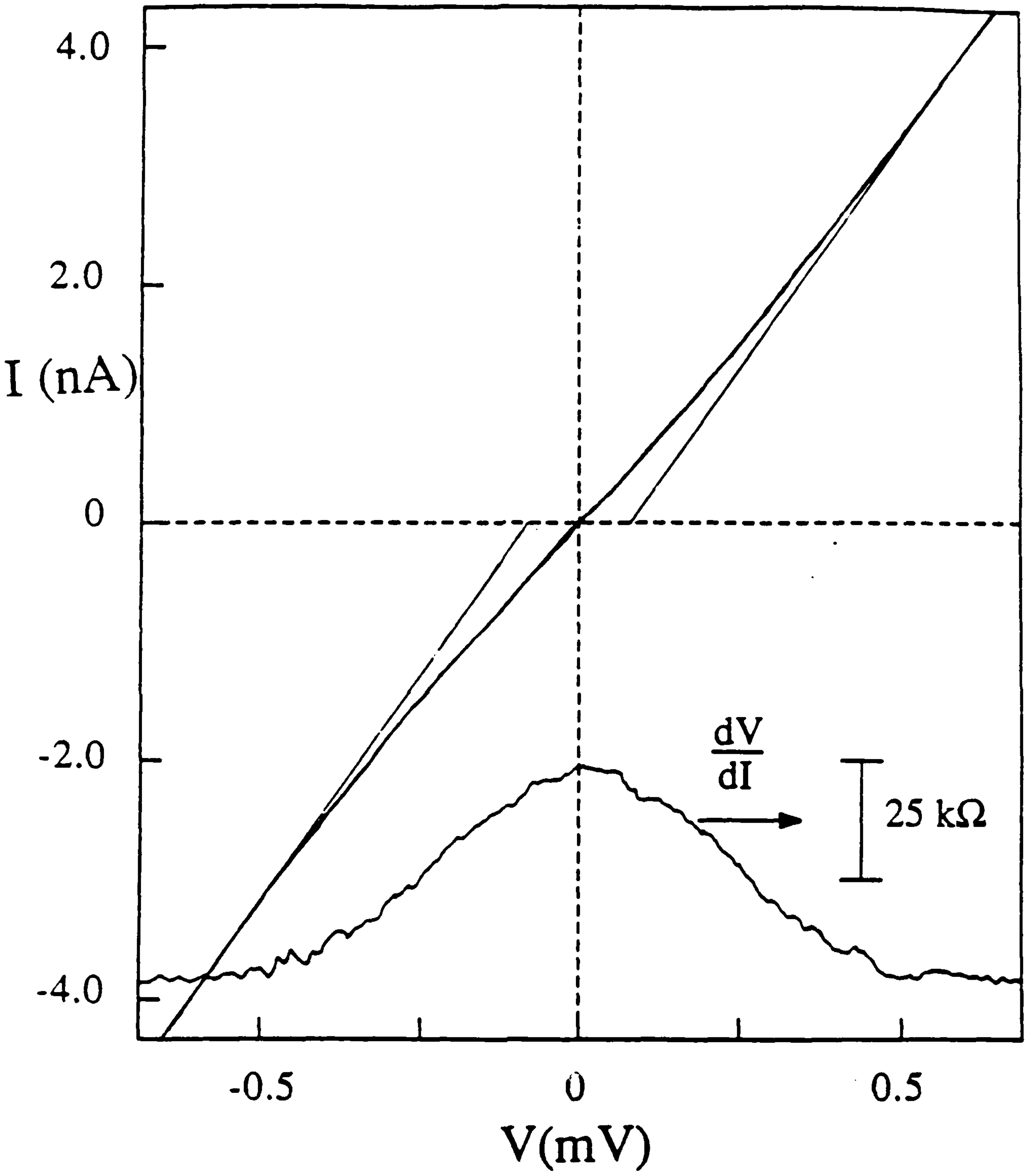

Fig. 4.15: I-V characteristic and its derivative for the sample with R_n = 140 kΩ in an applied magnetic field of H = 1.2 T at T = 30 mK. The increased dynamic resistance for small voltages and the voltage offset in the extrapolation from high currents and voltages are due to the Coulomb blockade.

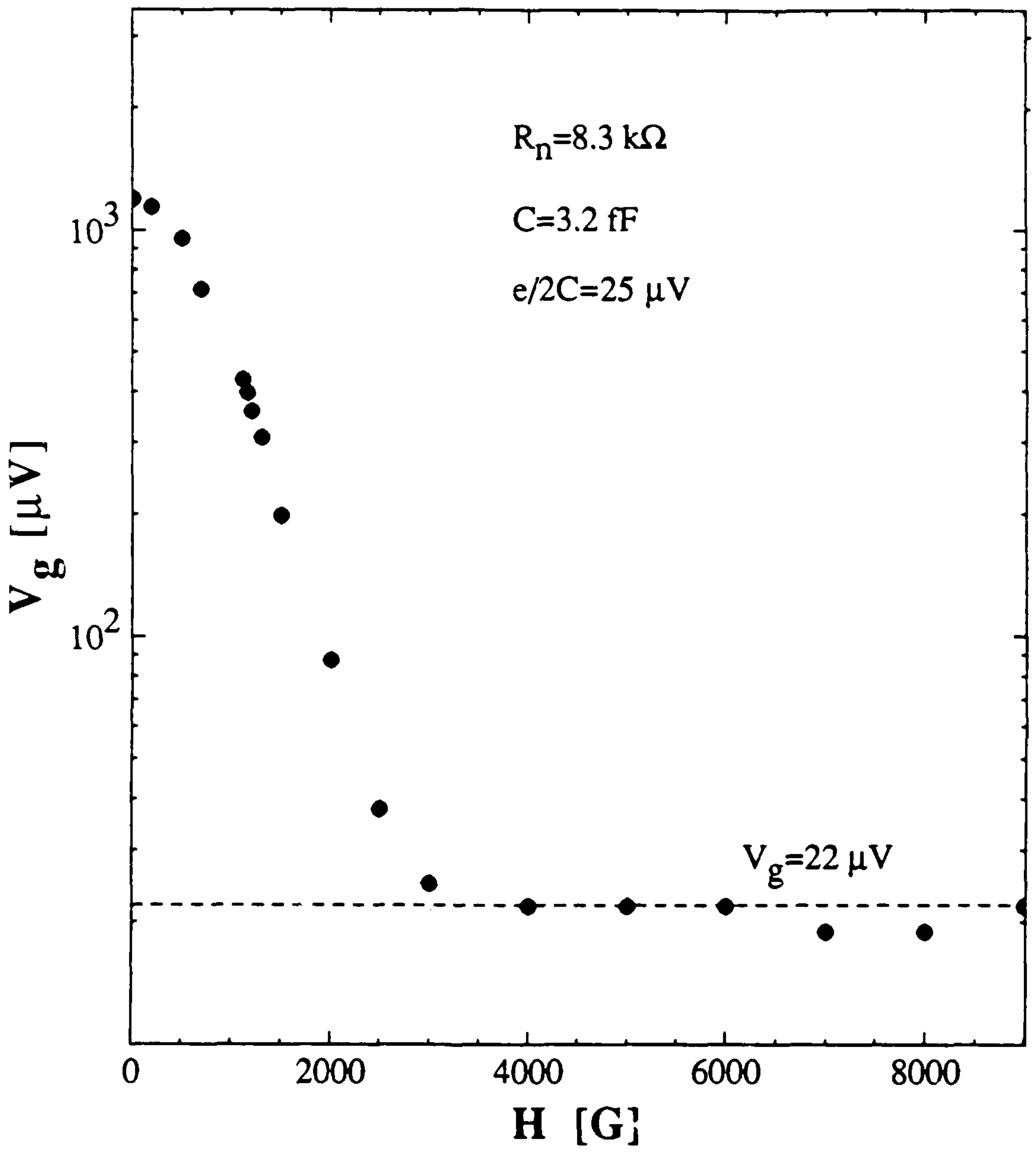

Fig. 4.16: Gap voltage $V_g(H)$ as a function of magnetic field for the sample with R_n=8.3 kΩ. V_g diminishes rapidly at low H, as the superconducting energy gap is decreased, and then reaches a field-independent level at large H, reflecting the presence of the Coulomb blockade. The blockade in this case is 22 μV, shown by the dashed line.

energetically forbidden for $q < e/2$. In a series array, the environmental coupling of each junction is decreased by the presence of the other. Put another way, a single junction connected to leads is shunted at high frequency by a line impedance of 50-100 Ω. Each junction of a double-junction series array sees a higher line impedance, due to the large blocking impedance of the other junction. The smaller current fluctuations, associated with the larger impedance, give smaller charge fluctuations, and a smaller smearing of the Coulomb blockade.

We see evidence for this effect in our samples. In Fig. 4.17, we show dV/dI vs. V for the single junction sample with $R_n = 140\ \mathrm{k}\Omega$ in several magnetic fields, all large enough to drive the sample normal. The blockade is fairly weak. The excess voltage is $e/2C \approx 80\ \mu\mathrm{V}$, but it has not developed fully by $V(I) = 500\ \mu\mathrm{V}$. In Fig 4.18, we show curves for one junction of a sample, sketched in Fig. 4.19, with three junctions, each decoupled from the continuous leads by one other small capacitance junction. The blockade in this case is noticeably sharper. Other experiments showing the blocking effect of tunnel junctions in the leads have been done by Delsing, et al. [1989a].

A second interesting effect is the pronounced weakening of the blockade in single junctions in a large magnetic field (see Fig. 4.17). Spin-flip scattering in the presence of the field was originally proposed as a source of wavefunction dephasing and level broadening, which weakens the Coulomb blockade [Iansiti, 1988]. This weakening, however, does not exist for the multi-junction sample (Fig. 4.18), which shows a strong blockade up to 6.5 T, the limit of our superconducting magnet. If spin-flip scattering were the cause of the blockade smearing, it would also occur in the multijunction sample. The source of the broadening, then, remains a mystery.

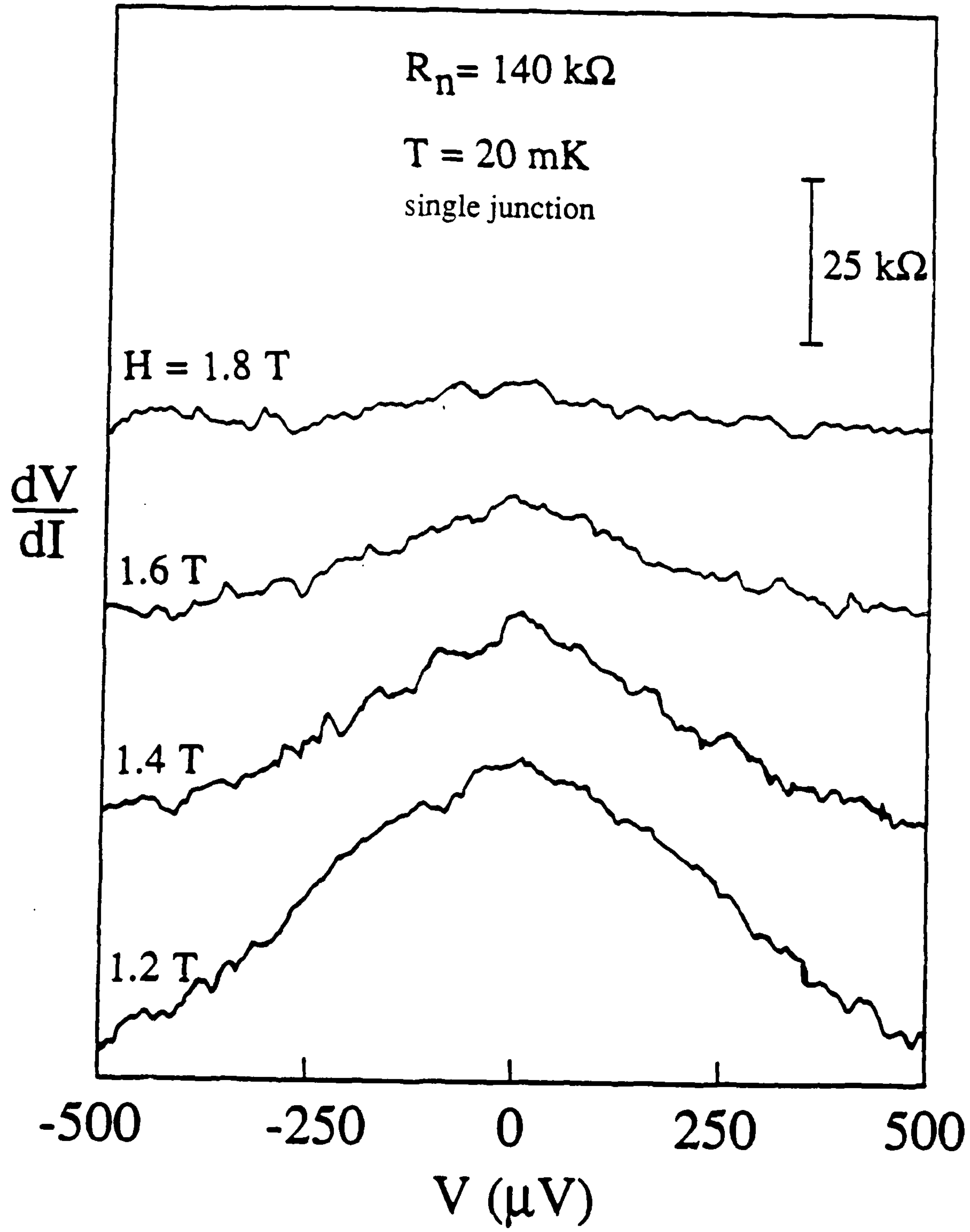

Fig. 4.17: *dV/dI* vs. *V* for the sample with R_n = 140 kΩ, at several magnetic fields. The Coulomb blockade for this single junction sample becomes weaker as the field increases, in contrast to the multi-junction sample in Fig. 4.18.

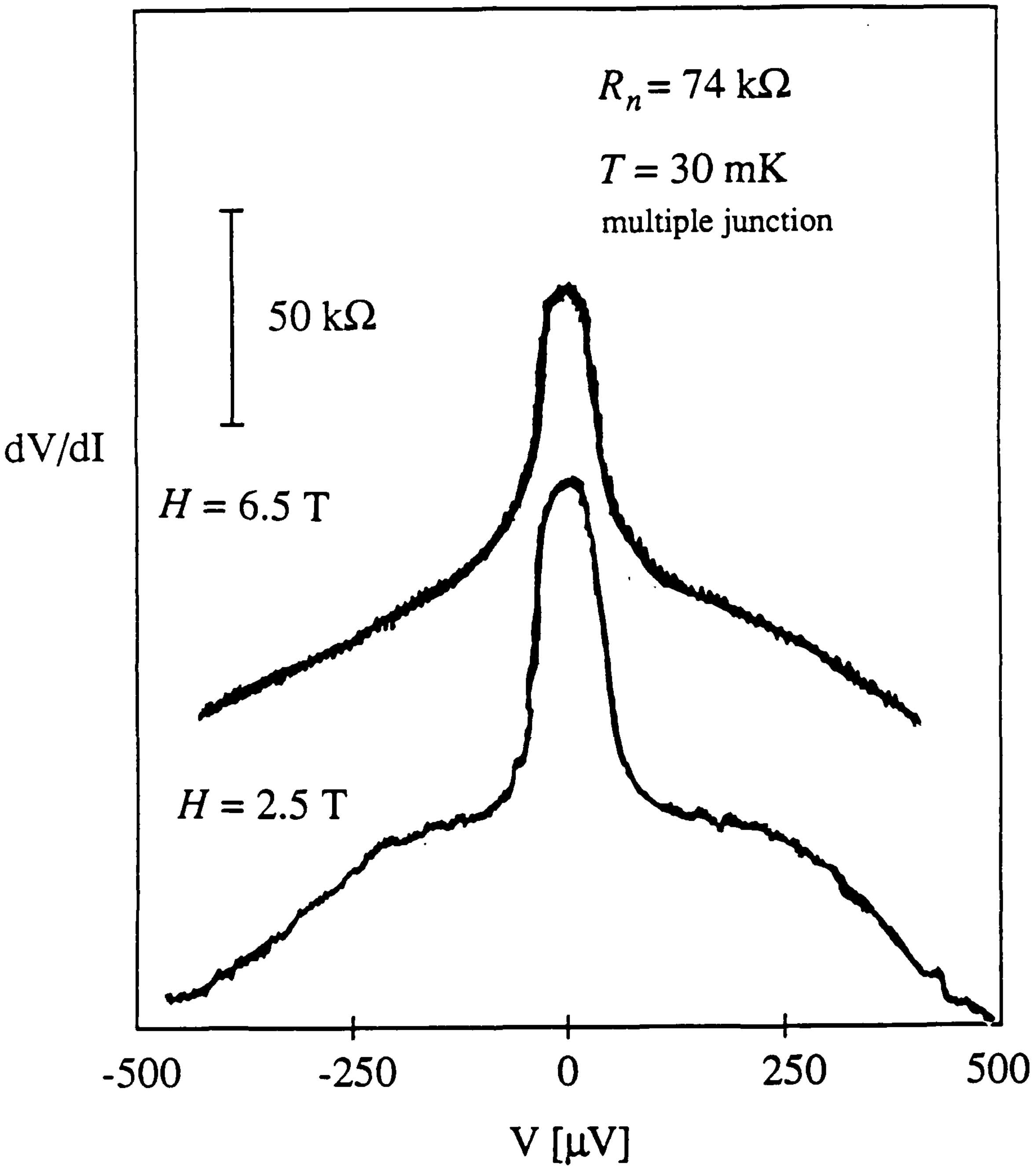

Fig. 4.18: *dV/dI* vs. *V* for the sample with $R_n = 74$ kΩ, at two different large magnetic fields. This junction is isolated from the leads by other small-capacitance junctions (see Fig. 4.19). The sharp Coulomb blockade is to be contrasted with the one in Fig. 4.17.

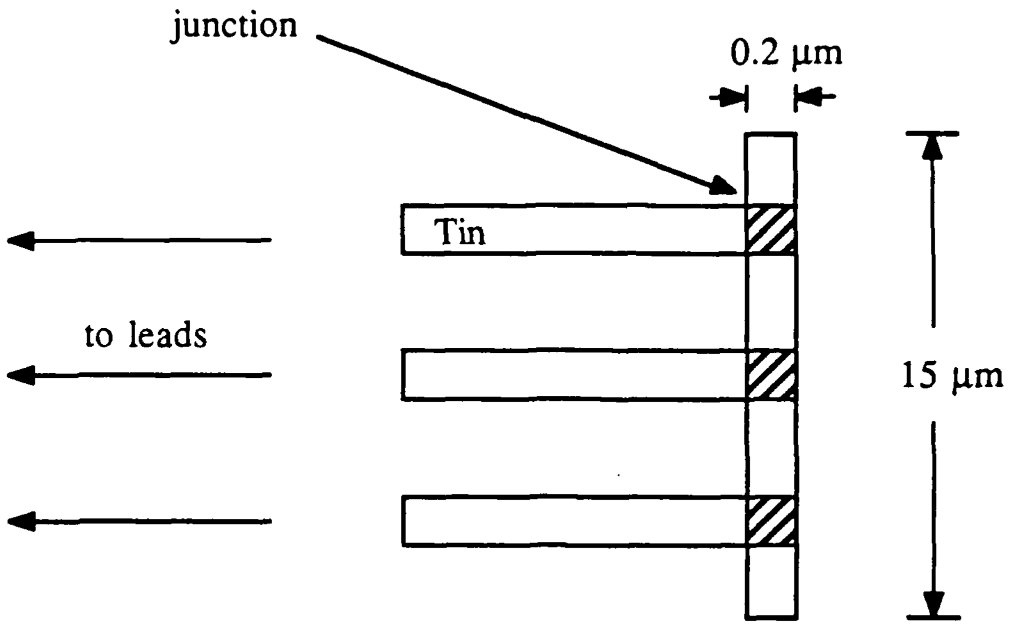

Fig. 4.19: Diagram of the multi-junction sample used to obtain the data in Fig. 4.18. The rectangles represent microfabricated tin wires. Each of the three small-capacitance junctions (striped squares) is isolated from the leads by the other two. The scales in the horizontal and vertical direction differ. This configuration was first employed to investigate charging effects by Fulton and Dolan [1987].

4.4 Summary

In this chapter, we have summarized the results of experiments on small, high-resistance Josephson junctions. The main discoveries are:

1. $I_c(T)$ is reentrant to a degree which grows as R_n increases. It is greatly suppressed below the Ambegaokar-Baratoff $I_{c0}(T)$.

2. $I_r(T)$ reflects the exponential freezeout of quasiparticles for $T \geq 1$ K, but is enhanced over the prediction of the RCSJ model ignoring fluctuations. Below ~1 K, $I_r(T)$ is unexpectedly flat.

3. There exists an anomalous resistance R_0 on the low-voltage branch.

4. A step appears on the low-voltage branch when E_J is reduced by a magnetic field. The size of the step correlates with $e/2C$ for the junction, suggesting the possibility of charging energy effects.

5. Similar nonlinearities are induced by an ac bias. The features are independent of the bias frequency, and thus not due to phase locking to Bloch or Josephson oscillations.

6. In the normal state, dV/dI is enhanced at low voltages, and the IVC has an excess voltage, both signatures of the Coulomb blockade.

We pointed out in chapter 1 that as the junction area decreases, two assumptions of the standard RCSJ model break down. First, the idealization of infinite impedance leads is inappropriate, especially at high frequency, where transmission line theory suggests that the line impedance is roughly that of free space, 377 Ω. Secondly, as we approach the regime $E_C > E_J$, there exists the possibility of strong quantum mechanical fluctuations of the phase. These fluctuations are modified, and, in principle, may be totally suppressed, by the environmental coupling.

In the next chapter, we investigate the consequences of the relatively small impedance presented by the leads at high frequency. Much of the surprising data is explained by an expanded RCSJ-plus-leads model, that also takes account of the nonlinearity at the gap voltage that arises from the onset of pair-breaking quasiparticle tunneling. Finally, in chapter 6, we discuss the evidence for the presence of large quantum mechanical phase fluctuations. The case for their impact is suggestive, but not so compelling as that for the importance of lead effects.

Chapter Five
The RCSJ-plus-leads Model

In this chapter we adapt the standard RCSJ model of a superconducting tunnel junction to include the frequency-dependent impedance presented by the leads and the onset of pair-breaking quasiparticle tunneling at $V = 2\Delta/e$. Section 5.1 outlines the usual RCSJ model (for additional discussions of this model, see Danchi [1983], Hu [1987] and Iansiti [1988]), and presents retrapping current data that deviates strongly from its predictions. We then introduce our extension of the standard model, which resolves this conflict. In sections 5.2 and 5.3 we discuss the implications of the new model for $R_0(T)$ and $I_c(T)$. Although quantitative results are scarce in these last two sections, clear avenues for future research exist. Finally, we note results from samples at low temperature that are inconsistent with a purely classical model and indicate the effect of quantum mechanical fluctuations in these small junction samples.

5.1 The Retrapping Current

The retrapping current I_r has always been the "little brother" of Josephson junction measurements: unappreciated, often ignored entirely, and its physics given attention only after that of the critical current I_c was well understood. Initial theoretical treatment of the RCSJ model left out the inertial (capacitive) term, which is entirely responsible for the existence of I_r, in the name of mathematical simplicity. The effect of thermal fluctuations on I_c was fully studied experimentally [Fulton and Dunkleberger, 1974] fourteen years before the first measurements of their impact on I_r [Iansiti et al., 1987; Kirtley et al., 1988]. At this moment, however, the retrapping current is enjoying a rise in popularity as experimenters have begun to exploit its sensitivity to the junction's electrical environment.

For an *underdamped* junction in the conventional model, I_r is proportional to the damping ($\propto 1/Q$). By contrast, the most likely observed value of the critical current, limited by thermal activation or MQT, is only logarithmically sensitive to changes in damping, an effect often masked by uncertainty in I_{c0}, the junction's unfluctuated critical current.

5.1.1 The retrapping current in the RCSJ model

Our starting point for understanding the dynamics of a Josephson junction is the resistively-and-capacitively-shunted-junction (RCSJ) model [McCumber, 1968]. For the present we include only the capacitance derived from the metal-oxide-metal sandwich device structure, while the resistor represents the dissipative conduction across the tunnel junction. In our experiments the junction's intrinsic dissipation is entirely due to quasiparticle tunneling through the oxide barrier. For the moment, however, let us assume that there is instead an ordinary (linear) shunt resistor R. The supercurrent channel is governed by the Josephson relations, $I_s = I_{c0}\sin\varphi$ and $d\varphi/dt = 2eV/\hbar$ [Josephson, 1962], where I_{c0} is the unfluctuated critical current, φ is the order parameter phase difference between the two junction electrodes, and V is the voltage across the junction. Current conservation leads to the "tilted-washboard" equation of motion for φ (Fig. 5.1):

$$\left[\frac{\hbar}{2e}\right]^2 C\frac{d^2\varphi}{dt^2}+\left[\frac{\hbar}{2e}\right]^2\frac{1}{R}\frac{d\varphi}{dt}+\frac{\hbar I_{c0}}{2e}\sin\varphi=\frac{\hbar I}{2e} \quad , \tag{5.1}$$

where I is the applied dc current. This may be generalized to include an applied ac current, or, as we will consider later, the noise currents generated by the resistor as required by the fluctuation-dissipation theorem. We linearize (5.1) by setting $\sin\varphi = \varphi$, and then define the oscillation angular frequency for $R = \infty$ as the plasma frequency $\omega_p = (2eI_{c0}/\hbar C)^{1/2}$. The damping parameter $Q = \omega_p RC$ is the quality factor of the oscillation in this linearized system. For $Q \geq 1$ and $I_{r0} < I < I_{c0}$, the system is bistable. $\varphi(t)$ can be in the "running

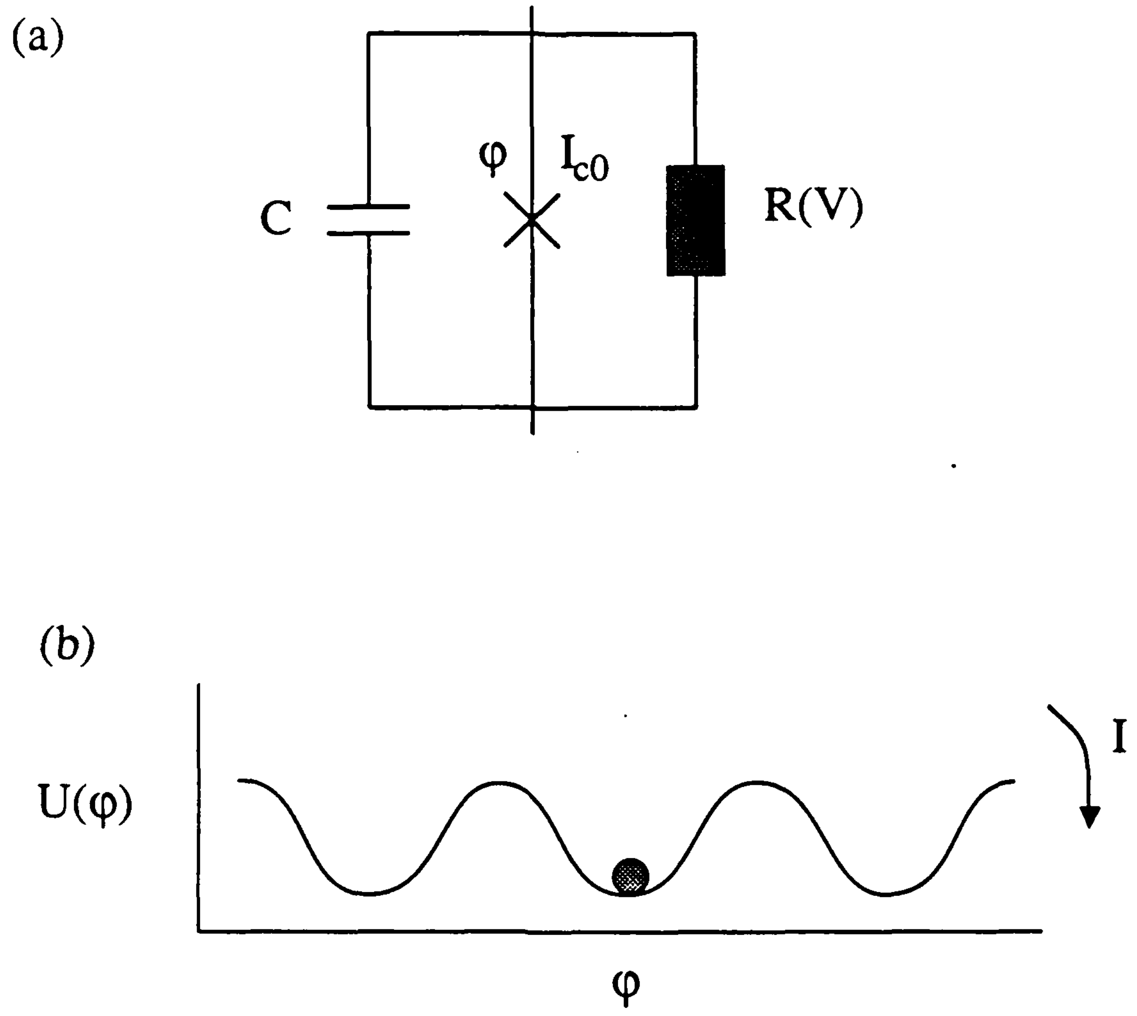

Fig. 5.1: (a) The RCSJ model. R(V) may be a quasiparticle tunneling channel, as well as an ordinary resistor. (b) The washboard picture. The mass of the ball, the height of the potential barrier, and the tilt are proportional to C, I_{c0}, and I, respectively.

state," where the potential energy gained by moving through one period is exactly balanced by the energy dissipated in the damping resistor, or φ can be in the "trapped state," sitting at the bottom of a potential well. It is simple to show that for $Q >> 1$ the minimum current for which this bistability exists (the "unfluctuated retrapping current") is given by $I_{r0} = 4I_{c0}/\pi Q$ [Stewart, 1968; Chen, et al., 1988].

To derive this result, Chen, et al. consider the phase motion in an untilted potential, neglecting damping, and solve for the trajectory which has zero velocity at the potential maxima. The solution is $\varphi(t) = 2\sinh^{-1}(\tanh\omega_p t)$. Integrating $V^2(t)/R$ for the motion and setting it equal to the potential energy gained by moving through one period when the tilt is I_{r0} ($\Delta P.E. = hI_{r0}/2e$) yields the desired result. In practice this formula is good to within 10% for any $Q \geq 1$. [Ben-Jacob et al., 1982]

When the dissipation is due to a quasiparticle channel with normal resistance R_n, the situation is complicated considerably. The quasiparticle tunneling I-V characteristic is highly nonlinear (Fig. 5.2), raising the question, "what is the effective resistance R^* that satisfies the relation $I_{r0} = 4I_{c0}/\pi\omega_p R^* C$?" We first note that since $I_r \leq I_{c0}$, retrapping occurs from a voltage $V \leq 2\Delta/e$, so that we expect only the part of the tunneling I-V curve below the gap to be relevant.

With this in mind, two theories have been put forward for the effective resistance. The "leakage-resistance" (L-R) model [Iansiti et al., 1985] makes the approximation that $R^*(T) = R_L = R_n e^{\Delta/kT}$, reflecting the exponential freeze-out of quasiparticles at low T and the intuitive result $R^*(T_c) = R_n$. This amounts to replacing the quasiparticle IVC with a two-part resistor whose current level at $V = 2\Delta/e$ is about equal to that of the quasiparticle channel just before the huge current increase. In contrast, Chen, Fisher, and Leggett (CFL) [1988] concentrate on the diverging dynamic conductance at *low* voltages to arrive at the result (valid for $\Delta >> kT >> \hbar\omega_p$)

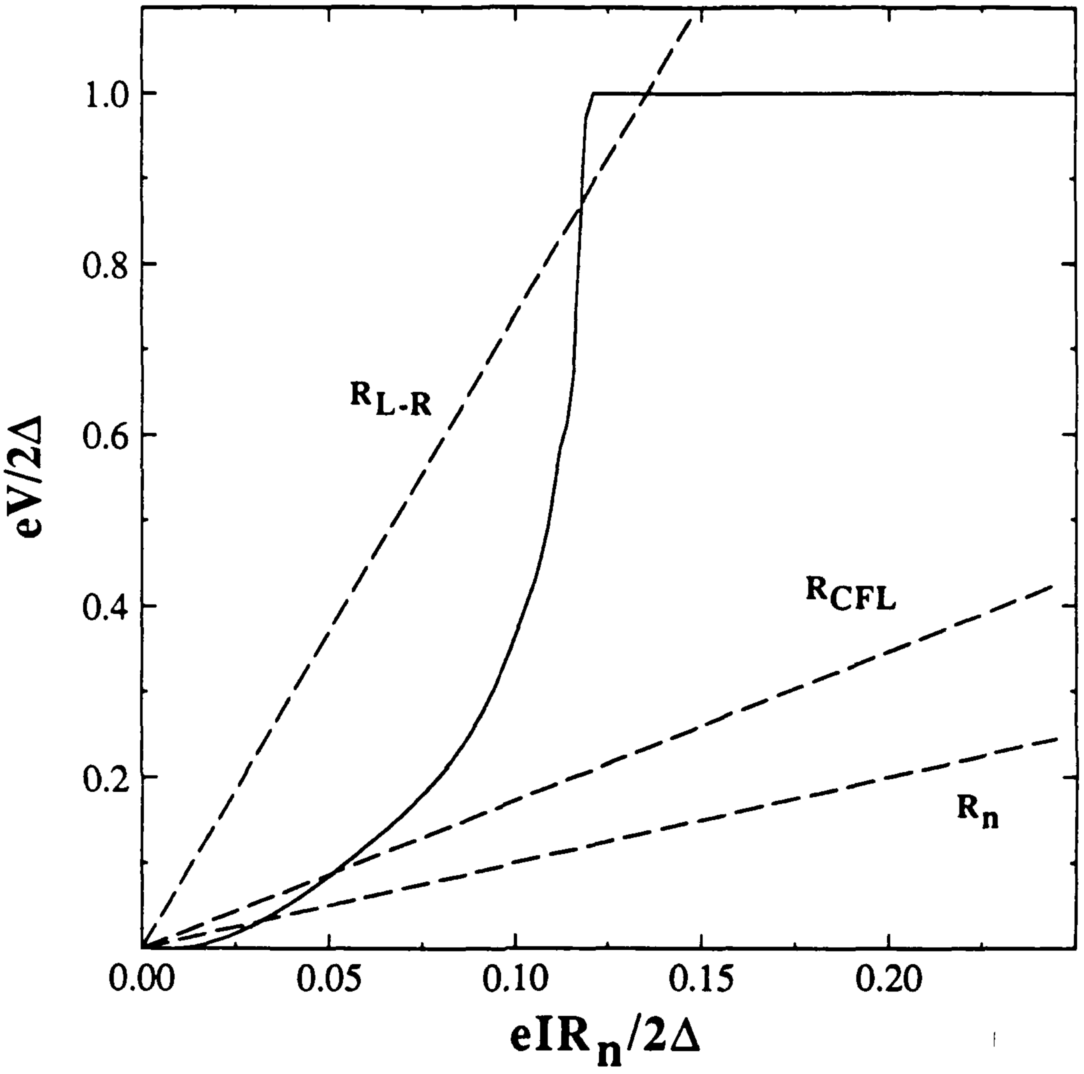

Fig. 5.2: A plot of the true quasiparticle I-V curve and three approximations. The solid line is a theoretical tunneling I-V for $T = \Delta/2ek$ [Van Duzer and Turner, 1981]:

$$I_{qp} = \frac{2e}{R_n} e^{-\Delta/kT} \left(\frac{2\Delta}{eV + 2\Delta} \right)^{1/2} (eV + \Delta) \left(\sinh \frac{eV}{2kT} \right) K_0 \left(\frac{eV}{2kT} \right) .$$

The three dashed lines show the L-R, CFL, and normal resistances. For the CFL resistance, we have used $\hbar\omega_p = \Delta/4e$.

$$R^*_{CFL}(T) = R_n \, e^{\Delta/kT} \left[\frac{3kT}{4\Delta\left\{\ln(\pi kT/\hbar\omega_p) - 0.237\right\}} \right] . \tag{5.2}$$

Both theories predict that $I_r \rightarrow 0$ as $T \rightarrow 0$ due to the dominating $e^{\Delta/kT}$ factor in $R^*(T)$. The difference between the two results is the factor in brackets in (5.2), which is less than one, so the L-R model predicts a larger $R^*(T)$ and smaller $I_r(T)$ than the CFL model.

The measured $I_r(T)$ for a number of samples is presented in Fig. 5.3, along with the predictions of the L-R and CFL theories for the 8.3 kΩ sample; the predictions for the other samples are curves of similar shape, translated vertically on the log plot to reflect the increase or decrease of I_{c0}. The major disagreement between experiment and theory is the low temperature plateau in I_r observed for each sample, differing strongly from the prediction that $I_r = 0$ at $T = 0$. The fit at higher temperature is better, reproducing the increase of the data with increasing T, but still is unsatisfactory.

If we include noise currents in the RCSJ model [Ben-Jacob, et al., 1982; Chen, et al., 1988], we can force a fit at high temperature for each of our samples. As in the more familiar case of premature escape from the zero-voltage state [Fulton and Dunkleberger, 1974], fluctuations lead to a distribution of retrapping currents. Since the bistable region is $I_{r0} \le I \le I_{c0}$, and since both solutions must exist for there to be switching from one to the other, the effect of fluctuations is to *increase* I_r (while they *decrease* I_c) in a statistical fashion, with a most likely observed value that may be much larger than I_{r0}. The lifetime of the running state in the presence of thermal fluctuations is $\tau \approx (2\pi/\omega_p)\exp\{(I-I_{r0})^2R^2C/kT\}$ [Chen, et al., 1988]. For $I = 2I_{r0}$, this may be written in the more intuitive form $\tau \approx (h/2eV_{r0})\exp(CV_{r0}^2/kT)$, where $V_{r0} \equiv I_{r0}R$ is approximately the voltage from which the system retraps in the absence of fluctuations. We recognize the prefactor as the inverse of the Josephson frequency at retrapping, $\nu_J = 2eV_{r0}/h$, and the activation energy in the Boltmann factor is twice the energy stored in the capacitor at $V = V_{r0}$. This energy is a measure of the size of the fluctuation needed to

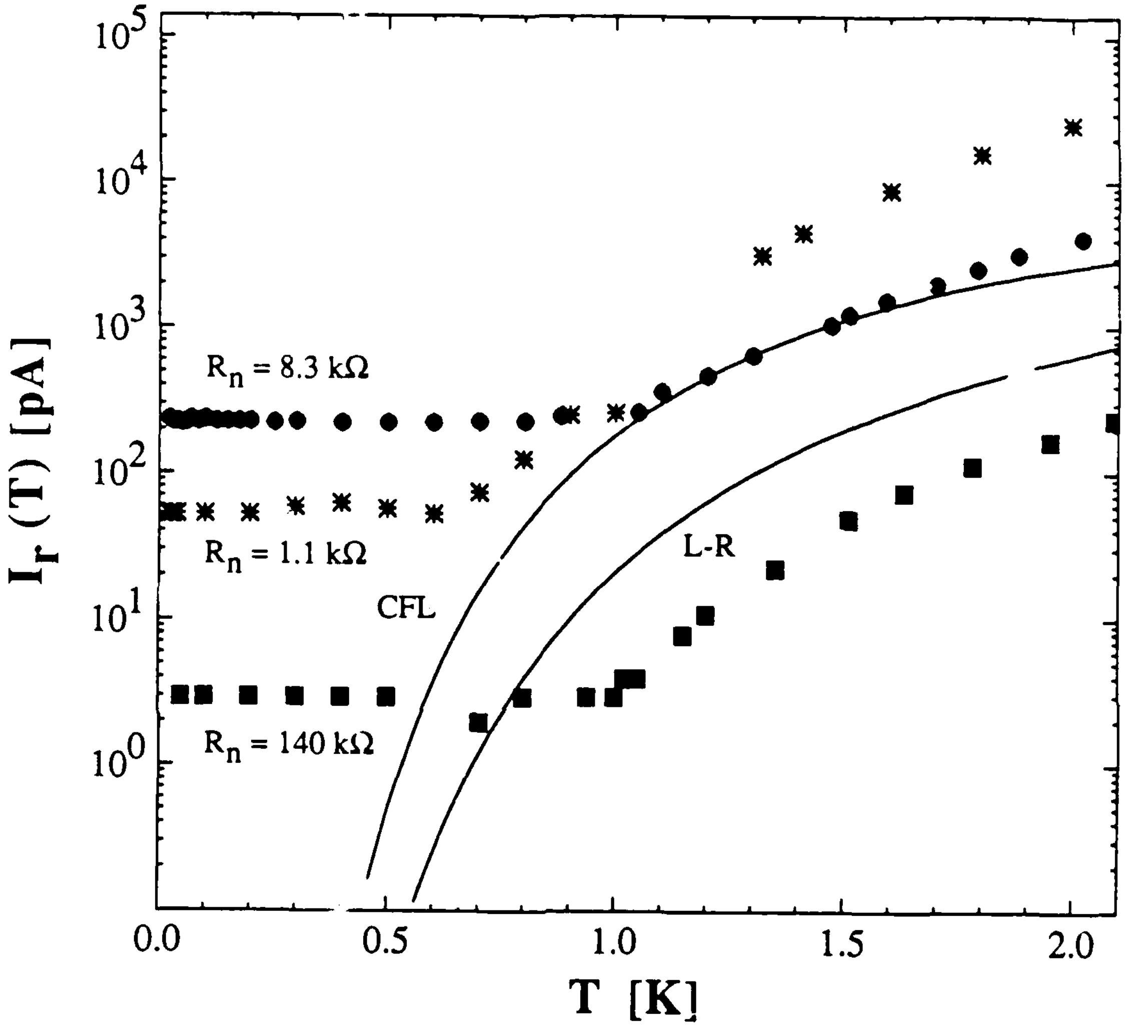

Fig. 5.3: $I_r(T)$ for three samples with two theories for one data set. The solid lines show the values of $I_r(T)$ predicted for the 8.3 kΩ junction by the CFL and L-R theories in the absence of fluctuations. Each follows the trend of the data for $T > 1$ K (the CFL theory gives a fairly good fit), but both deviate strongly from the data at low T.

trigger retrapping. An equation for τ of this form also applies when the noise currents are due to "blue noise" or "quasiparticle-colored blue noise" at $T = 0$, with kT replaced by $\hbar\omega_p/2$ and Δ; the activation energy is unchanged [Chen, et al., 1988] .

As in the case of premature switching from the trapped state, each form for τ yields a most likely measured retrapping current I_r^*, whose value solves the implicit equation $d\tau(I_r^*)/dI = 1/|I|$, where I is the current sweep rate [Danchi et al., 1984]. A simpler equation which gives nearly the same result and is more intuitive is $\tau(I_r) = \tau_{expt}$, where τ_{expt} is the experimental timescale (e.g. the time to sweep the current over some active range); the precise value of this time is vague as we have defined it, but it affects I_r only logarithmically. Given these four theories (L-R, CFL, L-R plus fluctuations, and CFL plus fluctuations), each with a similar T dependence but different magnitude, there is usually one that fits the data fairly well for temperatures above the point where I_r levels off (see Fig. 5.4). Since the theory that best fits the data differs from sample to sample, however, and since *none* of these theories predicts the plateau at low T, some essential physics must still be lacking. This physics is the interaction of the low impedance presented by the leads at high frequency and the sharp increase in quasiparticle current at $V = 2\Delta/e$.

5.1.2 The RCSJ-plus-leads model

We now turn to our explanation of the I_r data, which relies on a more sophisticated junction model where the Josephson channel with unfluctuated critical current I_{c0} is shunted by the junction's geometric capacitance C, a quasiparticle channel with normal resistance R_n, and a transmission line formed by the leads. We use the theoretical $I_{c0}R_n$ product to determine I_{c0}, and a specific capacitance of 25 fF/μm^2, combined with the measured junction area, to estimate C. To understand the effect of leads on I_r, and to motivate a "two-frequency" approximation of the line used below, it is helpful to review the

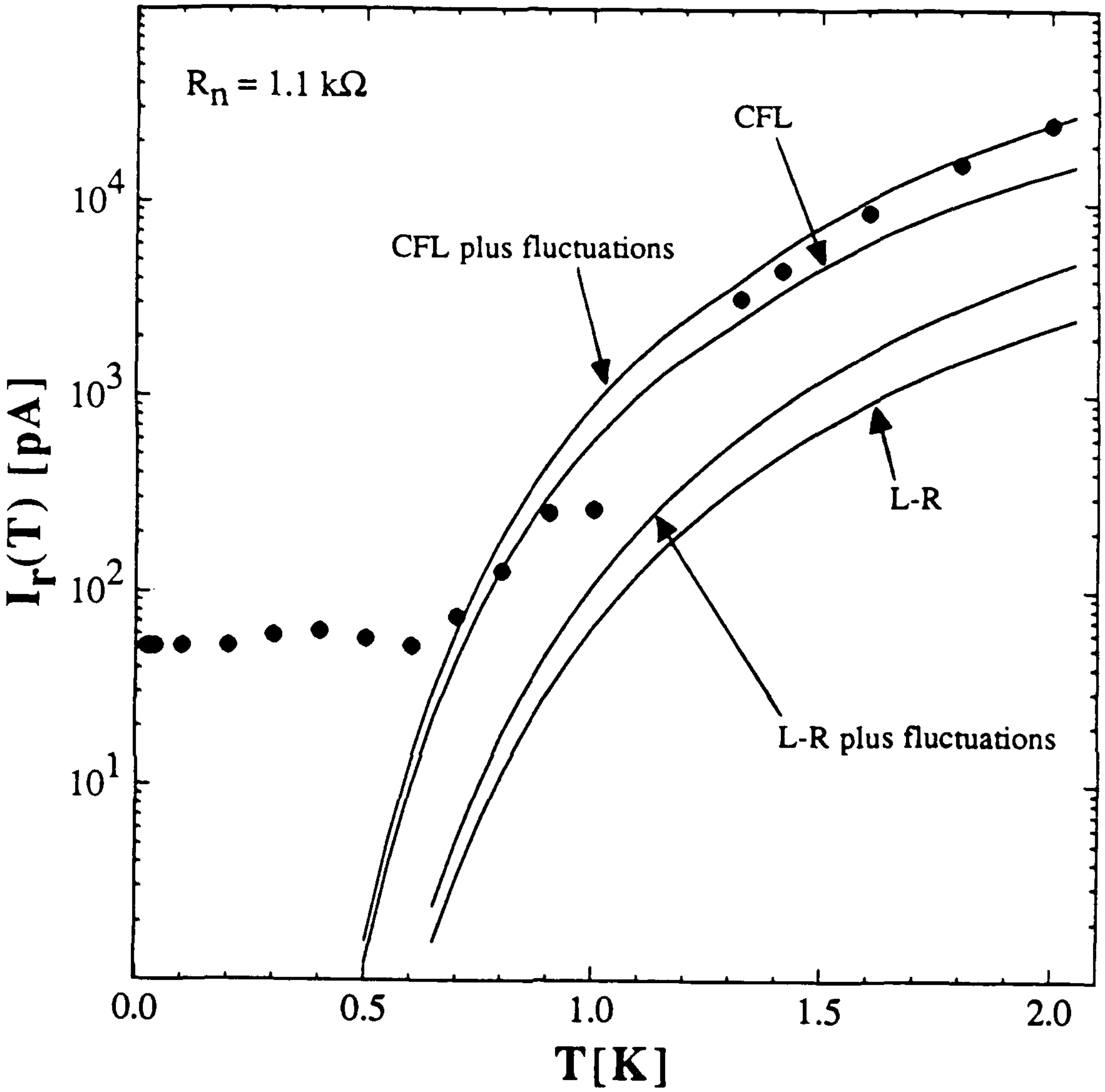

Fig. 5.4: $I_r(T)$ for the 1.1 kΩ sample (solid dots) as well as four theories (lines): the L-R theory with and without thermal fluctuations and the CFL theory with and without fluctuations. Note that for this sample the best fit at high temperature is provided by the CFL theory with fluctuations, while for the 8.3 kΩ sample, the CFL theory *without* fluctuations agreed with the data.

dynamics on the retrapping branch of the I-V curve for the RCSJ model with a linear shunt resistor and no fluctuations.

In this case, the phase point moves through the sinusoidal potential, slowing down as it climbs the potential maxima and speeding up as it moves towards the minima. The motion is strictly periodic (taking φ modulo 2π), and $V(t) \propto d\varphi(t)/dt$ has Fourier components at dc, and the fundamental and harmonics of $\omega_J = 2eV(I)/\hbar$, the frequency with which the particle traverses one period of the potential. For $I >> I_{r0}$ the potential is a perturbation on the "terminal velocity" condition $V(I) = IR$. The voltage is well approximated by $V(t) \approx V(I)+v_{ac}\cos\omega_J t$; the Josephson channel carries little dc current, the I-V curve of the device is well approximated by $V(I) = IR$, and the higher harmonics of the motion are negligible. It is only close to I_{r0} that the I-V curve deviates strongly from that of the resistor alone, and that the higher harmonics become important. Using an analog simulator of (5.1), we see that even at 1.1 I_{r0} the dc voltage is still within 15% of IR, and the second harmonic of ω_J is 20 dB down from the fundamental. These results are the foundation of the procedure for estimating I_{r0} proposed in the next paragraph.

To find I_{r0}, we could try to solve for the potential tilt that admits the trajectory with $d\varphi/dt = 0$ at all potential maxima. Our simpler, approximate procedure assumes that on the retrapping branch, for $I > I_{r0}$, the I-V curve is given by $V(I) \approx V_S(I) = IR$, where $V_S(I)$ is the I-V characteristic of the shunt *alone*. We also assume that the dominant Fourier components of the phase point motion are at dc and $\omega_J = 2eV_S(I)/\hbar$, so that the Josephson channel sources a current $I_{c0}\sin\omega_J t$, which flows through R and C according to their impedances at ω_J. The average power dissipated at ω_J is $I_{c0}^2\mathrm{Re}[Z(\omega_J)]/2$, where $Z(\omega)$ is the frequency-dependent impedance of R and C in parallel. At large I, $V(I)$ is large, as is ω_J. The capacitor passes most of the current at ω_J, and the resistor dissipates little energy at this frequency. At very small I, $V(I)$ and ω_J are both small, so that at ω_J almost all the current flows through the resistor. The power dissipated at ω_J would now be nearly $I_{c0}^2R/2$, which *exceeds* $IV(I)$, the power fed to the device by the current supply: our assumption that $V(I) \approx IR$ must have broken down. The I-V curve is strongly distorted by the Josephson potential, and retrapping is imminent (or has already occurred). *We will take as an estimate of I_{r0}, the retrapping current in the absence of fluctuations, that current at which the power dissipated at high frequency in this approximation is equal to the power provided to the system by the dc supply.*

To verify the accuracy of this estimate, consider its prediction for the RCSJ model. The retrapping criterion is $I_{r0}V_S(I_{r0}) = I_{c0}^2\mathrm{Re}[Z(\omega_J(I_{r0}))]/2$, or

$$I_{r0}^2 R = \frac{I_{c0}^2 R}{2\left[1+\omega_J^2 R^2 C^2\right]} \approx \frac{I_{c0}^2}{2(2eI_{r0}R/\hbar)^2 RC^2} \quad . \tag{5.3}$$

We obtain the second near-equality by assuming $\omega_J(I_{r0})RC >> 1$. Solving (5.3) yields

$$I_{r0} = \frac{I_{c0}}{2^{1/4}\omega_p RC} \quad , \tag{5.4}$$

which agrees with the conventional result to within a factor $(2)^{1/4}4/\pi \approx 1.5$. This value for I_{r0} gives $\omega_J(I_{r0}) = 2eI_{r0}R/\hbar = \omega_p/(2)^{1/4}$. Since we are in the underdamped limit, $Q = \omega_p RC >> 1$, the assumption used to derive the second half of (5.3) is justified. Our condition gives a good estimate of I_{r0} for the RCSJ model.

To this point we have ignored the leads. Our approximation implies that the lead impedance at dc and ω_J determines I_{r0}. At dc the leads present a large resistance shunted by a large stray capacitance; at ω_J transmission line effects are important. The samples retrap from $V_r \approx 2\Delta/e$ at low T, so $\omega_J/2\pi \approx 500$ GHz. At this high frequency, the impedance of the leads is difficult to determine precisely, but the contribution of the *on-chip* circuitry dominates. The characteristic impedance of an infinite line is typically nearly real with magnitude $(\mu_0/\varepsilon_r\varepsilon_0)^{1/2}\log(R_1/R_2)/2\pi \approx 100\ \Omega$, where $(\mu_0/\varepsilon_0)^{1/2} = 377\ \Omega$ is the impedance of free space, ε_r is the relative permitivity of the embedding dielectric (or some effective permitivity if there are regions with different permitivities), and R_1 and R_2 are characteristic dimensions of the line [Jackson, 1975, p. 385]. Any line with impedance discontinuities will exhibit resonances, but there is nothing in the data that indicates that any resonant effect is important. This could be due to an averaging of line parameters over some frequency range larger than any resonance width, losses which attenuate the reflected wave responsible for a resonance, or the lack of a resonance in the frequency range of interest.

With these ideas in mind, we model the leads as two channels in parallel with the junction: one at dc with large R_{dc} ($>>R$) and C_{dc}, and a second at ω_J with purely real admittance $Y_{ac} = G_{ac} \approx (100\ \Omega)^{-1}$. We require that Y_{ac} be open at dc; a capacitance in series reminds us of this qualification (see Fig. 5.5). The retrapping condition, $I_{r0}V_S(I_{r0}) = I_{c0}^2\mathrm{Re}[Z(2eV_S(I_{r0})/\hbar)]/2$, now yields:

$$I_{r0}V_S(I_{r0}) = I_{c0}^2 \frac{\left(G_{ac}+R^{-1}\right)/2}{\left[G_{ac}+R^{-1}\right]^2 + \left[2eV_S(I_{r0})C/\hbar\right]^2} \quad . \tag{5.5}$$

In the RCSJ model, $I_{r0} = 4I_{c0}/\pi Q \propto 1/R$, so $V_S(I_{r0}) = I_{r0}R = 2\hbar\omega_p/\pi e$, independent of R. According to (5.5), the additional damping of the leads increases I_{r0} and $V_S(I_{r0})$. If $R^{-1} >> G_{ac}$, as is true for low R_n junctions at T not too far below T_c, most of the current at ω_J flows through R, and the line has a negligible effect on I_{r0}. In this limit, we expect $I_{r0} \propto 1/R$, just as in the RCSJ model. When $R^{-1} << G_{ac}$, $V_S(I_{r0})$ is enhanced over the RCSJ value. The denominator of the r.h.s. of (5.5) is dominated by the second term (which increases with R, while the other term is constant), yielding

$$I_{r0}V_S(I_{r0}) = I_{c0}^2 \frac{G_{ac}/2}{\left[2eV_S(I_{r0})C/\hbar\right]^2} \quad . \tag{5.6}$$

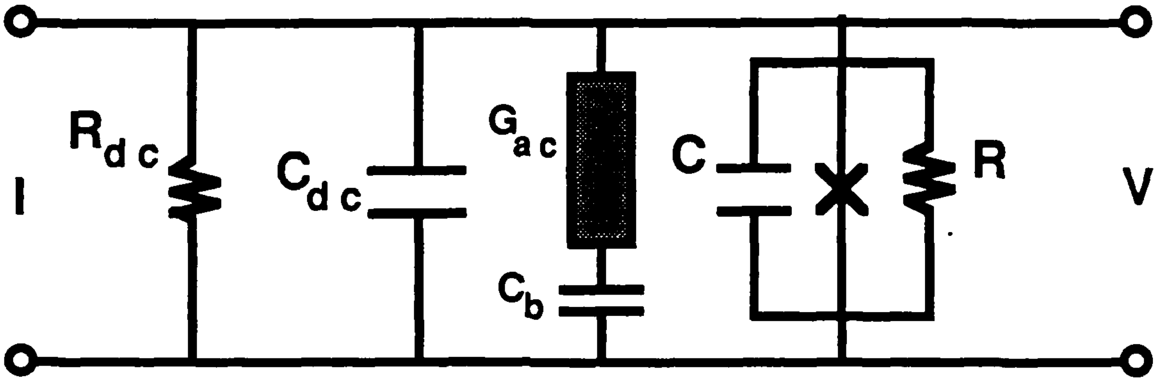

Fig. 5.5: Sketch of the two-frequency circuit model used in this section. C_b is a blocking capacitor indicating that the high-frequency line conductance G_{ac} carries no dc current.

If we set $V_S(I) = IR$, solving for I_{r0} yields

$$I_{r0} = \frac{I_{c0}}{2^{1/4}\omega_p RC}\left[RG_{ac}\right]^{1/4} = I_{r0}^{RCSJ}\left[RG_{ac}\right]^{1/4} \quad . \tag{5.7}$$

where I_{r0}^{RCSJ} is our estimate of I_{r0} for the RCSJ model without transmission line effects (see (5.3)). For the RCSJ model with linear resistor shunt, in the limit $G_{ac} >> R^{-1}$, the R dependence of I_{r0} changes to $I_{r0} \propto R^{-3/4}$. We have simulated this RCSJ-plus-leads model with an analog circuit, and have plotted the results in Fig. 5.6. There is a clear crossover from R^{-1} to $R^{-3/4}$ behavior near $RG_{ac} = 1$ ($R = 5$ kΩ in this simulation).

Now we consider the circuit in Fig. 5.5. The *dc* shunt is a quasiparticle channel with the strong gap nonlinearity, so $V_S(I) \le 2\Delta/e$ for any $I < I_{c0}$. This *maximum* possible dc voltage at retrapping combined with (5.4) implies a *minimum* I_{r0}:

$$I_{r0}^{min} \cong \frac{eI_{c0}^2}{4\Delta}\frac{G_{ac}}{G_{ac}^2 + (4\Delta C/\hbar)^2} \quad , \tag{5.8}$$

where we have used the fact that $R^{-1} << G_{ac}$ in our samples.

The solid line in Fig. 5.7 is $I_{r0}(T)$, obtained from (5.5) as follows: assume that $V_S(I_{r0}) < 2\Delta/e$, so that $V_S(I_{r0}) = I_{r0}R^*$, and calculate I_{r0}; if this results in $I_{r0}R^* > 2\Delta/e$, the assumption is not justified, so recalculate I_{r0} with $V_S(I_{r0}) = 2\Delta/e$. A L-R model was used for R^*, $I_{c0}(T = 0) = 110$ nA, and $G_{ac} = (90\ \Omega)^{-1}$. The open circles in Fig. 5.7 are from simulations using a circuit based on the Magerlein design [Magerlein, 1978; Hu, 1987]. A series combination of a resistor and large capacitor mimicked leads with a nearly real admittance, $Y_{ac} \approx G_{ac} = (90\Omega)^{-1}$ for $\omega > \omega_p$. To model the nonlinearity of the quasiparticle channel at $2\Delta/e$, we used a two-part resistor with $I = V/R_n$ for $V \ge 2\Delta/e$ and $I = V/R^* = V/R_n\, e^{\Delta/kT}$ for $V \le 2\Delta/e$; we chose R_n and C to match the $R_n = 8300\ \Omega$ sample (see Table 5.1). There were no other adjustable parameters.

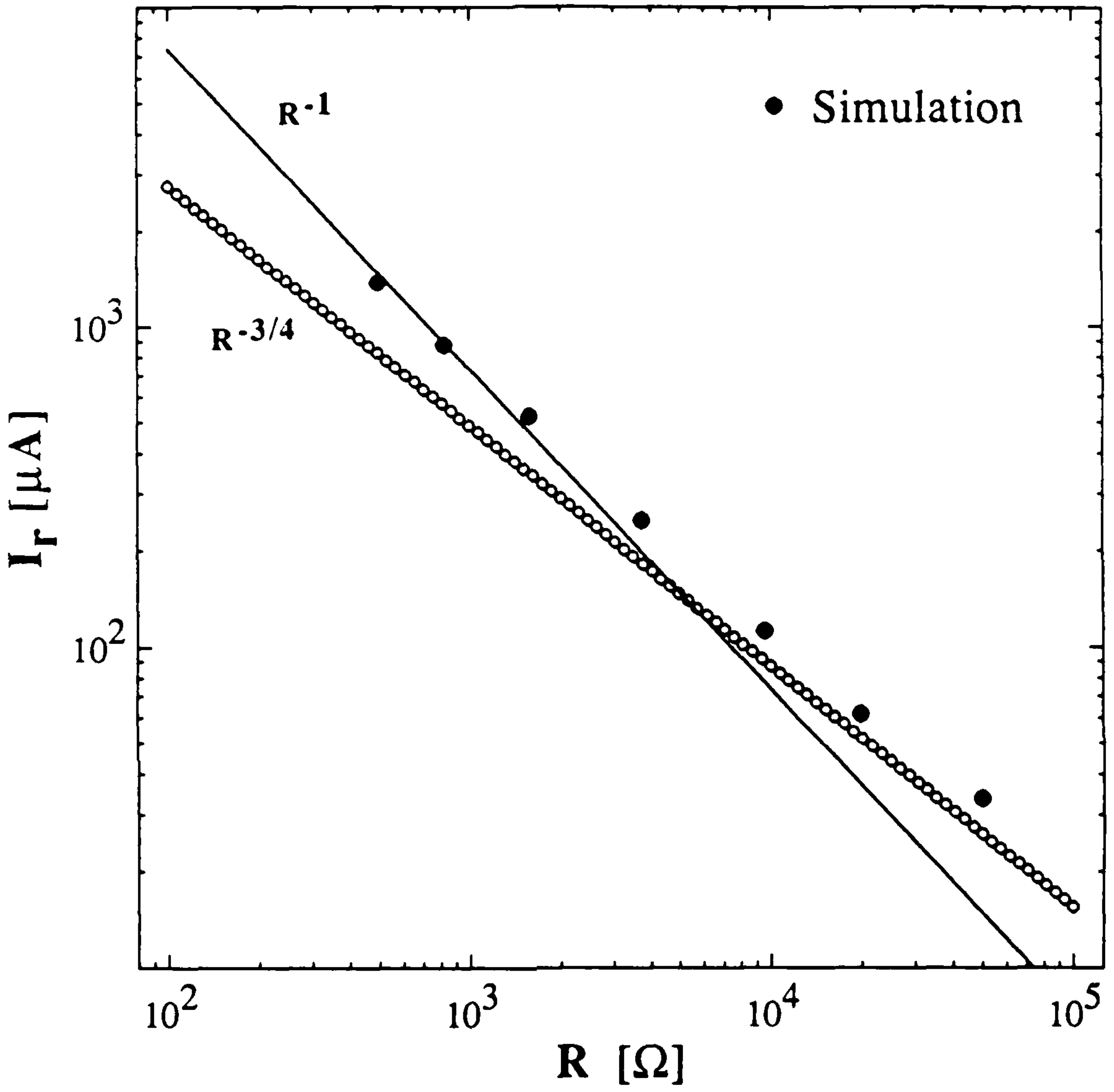

Fig. 5.6: This graph shows the effect of a transmission line on I_{r0} when the dissipation at dc is a linear resistor (*not* a quasiparticle tunneling channel). The solid line is the RCSJ result, $I_{r0} = I_{r0}^{RCSJ} = 4I_{c0}/\pi Q$; the open circles are $I_{r0} = I_{r0}^{RCSJ}[RG_{ac}]^{1/4}$, reflecting (5.6). The solid dots are simulated values. The simulation parameters are: I_{c0} = 1.2 mA, C = 30 nF, and $\omega_p/2\pi$ = 22.3 kHz. The "transmission line" is a 5 kΩ resistor and a 3 μF capacitor in series. For frequencies well above $[2\pi(5\ \text{k}\Omega)(3\ \mu\text{F})]^{-1}$ = 11 Hz, which includes $\omega_p/2\pi$, the line is almost purely resistive, with impedance 5 kΩ. The crossover from the R^{-1} to $R^{-3/4}$ dependence occurs near $R = G_{ac}^{-1}$ = 5 kΩ.

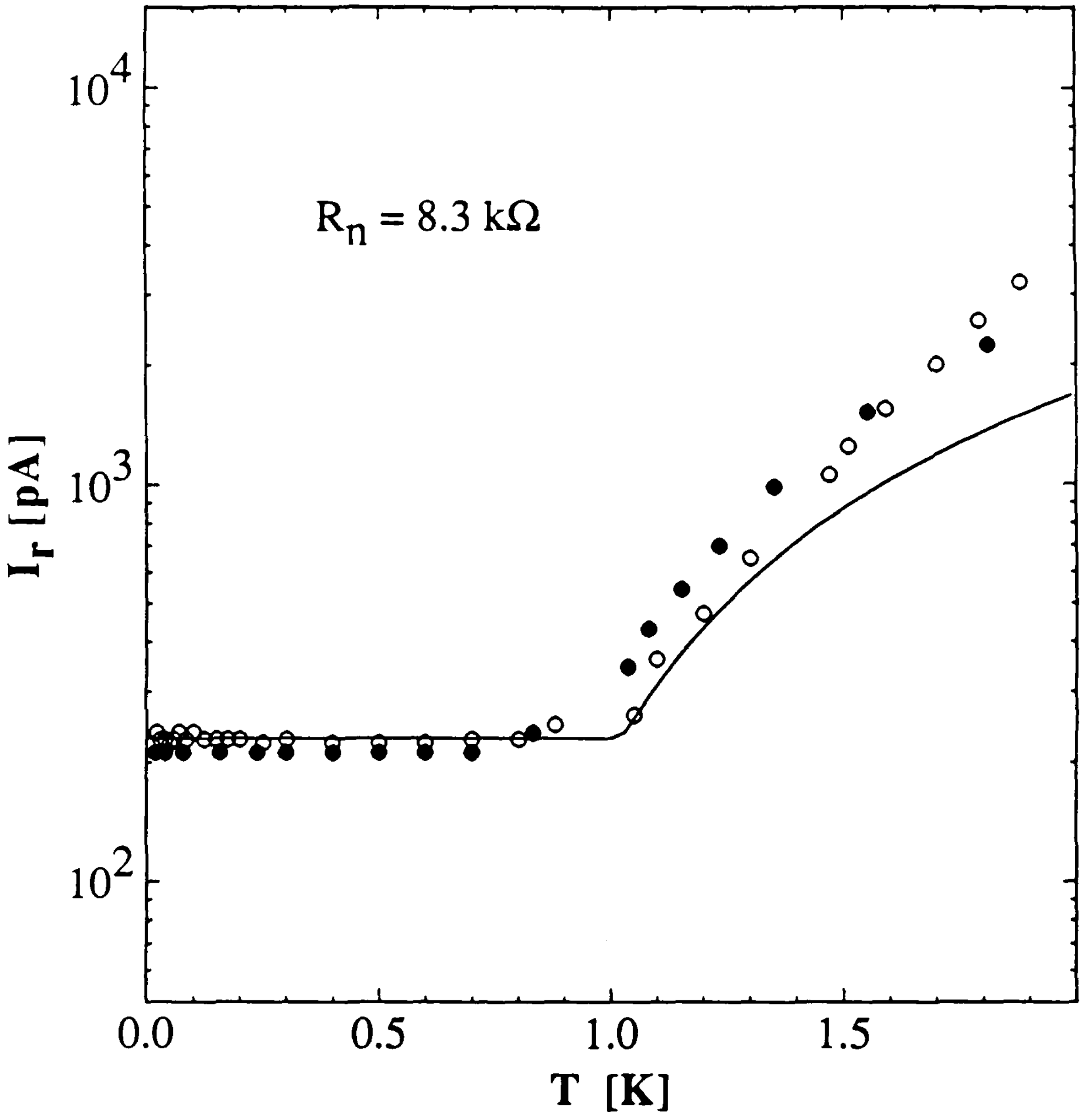

Fig. 5.7: I_r vs. T for the sample with $R_n = 8300\ \Omega$. The open circles are data. The solid dots are results of analog simulations incorporating the transmission line due to the leads. The line is obtained using (5.5) and the procedure described in the text.

Both calculated and simulated $I_r(T)$ agree well with the data, reproducing I_r^{min}, the temperature at which I_r starts to rise, and the abrupt transition between the two behaviors. Interestingly, even when $I_r(T)$ is increasing, it is enhanced by a factor of more than six over the prediction of a model ignoring the damping from the leads. Both the calculated and simulated I_r fall significantly below the measured values for $T > 1.5$ K. This discrepancy is probably due to thermal fluctuations which lead to a measured $I_r > I_{r0}$ [Ben-Jacob, et al., 1982], but are difficult to treat exactly in a model with frequency-dependent damping.

The success of models using a L-R form for R^* supports our intuition that if the junction retraps from near $2\Delta/e$, then the details of the quasiparticle tunneling at $V << 2\Delta/e$ (which lead to the CFL theory of R^*) should not be important. The moderately good fit obtained using a RCSJ model with the CFL $R^*(T)$ (see Fig. 5.3) is apparently fortuitous, reflecting only that a lower $R^*$and leads both act to enhance I_r. The CFL theory for R^* should, however, characterize the quasiparticle channel correctly in samples that retrap from $V << 2\Delta/e$ [Kirtley, et al., 1988].

Finally, we compare the predictions of (5.8) with the measured I_r^{min} for a variety of samples (see Table 5.1), using $G_{ac}=(90\ \Omega)^{-1}$. The agreement is good, reproducing the nonmonotonic nature of I_r^{min} versus R_n and C. We have also calculated our predicted I_r^{min} for the sample of Kirtley, et al.[1988] which showed no minimum at low T. Our value of 3 fA is 4 orders of magnitude smaller than any retrapping current measured in their work; they did not reach temperatures low enough to observe this effect .

5.2 R_0

In the last section, we had great success explaining the $I_r(T)$ data using an extended RCSJ model, which included the high frequency damping provided by the leads. In this section and the next we consider the implications of this model for $R_0(T)$ and $I_c(T)$.

TABLE 5.1: Parameters for various samples. R_n is the normal resistance. C is the geometrical capacitance. I_r^{min} exp is the minimum measured retrapping current. I_r^{min} calc is calculated using (5.8).

Sample	R_n [kΩ]	C [fF]	I_r^{min} exp [pA]	I_r^{min} calc [pA]
1	140	2	3	1.3
2	8.3	3.2	230	230
3	1.1	100	53	25

5.2.1 The importance of $R_0 > 0$

The junction I-V curve (IVC) dictates the need for modification of the RCSJ model. As noted by Ono et al. [1987], an IVC with both hysteresis and a "tilted low-voltage step," i. e. phase evolution (and therefore a dc voltage) on the low-voltage branch, is inconsistent with the usual RCSJ model with fluctuations.

When $I_{r0} \leq I \leq I_{c0}$, the RCSJ model phase space is divided into a basin of attraction of the nonequilibrium ("running") state and one of the equilibrium ("trapped") state, as shown in Fig. 5.8. [Ben-Jacob et al., 1982]. From this figure, it is clear that a typical fluctuation out of the equilibrium basin will lead to escape, not retrapping in another well. The IVC for such a system in the presence of fluctuations will be one of two types. If τ_t, the lifetime of the trapped state, is of order the experimental timescale or longer, there will be a true zero-voltage branch with premature switching to the voltage state at $I \leq I_{c0}$; if, on the other hand, τ_t and τ_r, the lifetime of the running state, are both short (due, for example, to a large amount of thermal noise), the IVC will be non-hysteretic, with a time-averaged $V(I)$.

Ono et al. showed convincingly with computer simulations that a RCSJ model modified to give frequency-dependent damping (see Fig. 5.9) could produce an IVC with $R_0 > 0$. They were, however, only able to reproduce their data quantitatively using a fictitious $T^* >> T_{expt}$. Moreover, because they used a lumped element R-L-C series approximation to the line (see Fig. 5.9), the shunt in their simulation had an unrealistically large impedance at high frequency, where the impedance of the inductor was much greater than 100 Ω, a typical transmission line impedance.

We have qualitatively verified the results of Ono et al. using an analog simulator. The initial simulations were of the RCSJ model with a two-part resistor approximation to the quasiparticle channel. The simulator parameters were: $I_{c0} = 610\ \mu\text{A}$, $C = 200$ nF, $\omega_p/2\pi = 3$ kHz, $R_n = 2.9\ \text{k}\Omega$, $R_l = 27\ \text{k}\Omega$, and $2\Delta/e = 2$ V. At a low noise current level, we observed hysteretic IVCs with premature switching to the running state, and no

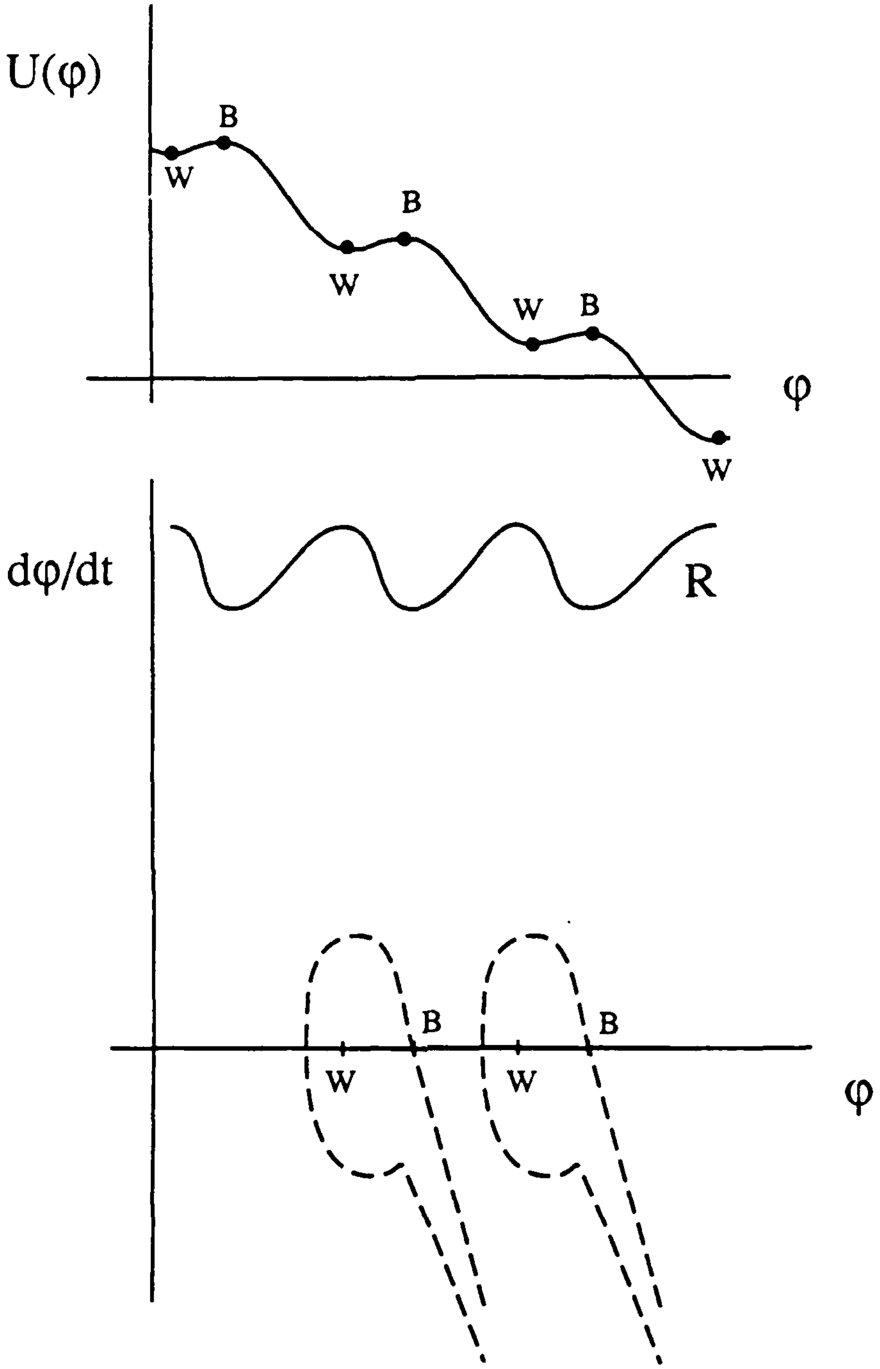

Fig. 5.8: (a) the Josephson potential for $I_{r0} < I < I_{c0}$. W ("well") and B ("barrier") are points of stable and unstable equilibria. (b) phase space for the system. Each point W is the attractor for a trapped state; the curve R is the running state attractor. Points inside a dashed curve form the basin of attraction of a trapped state, while those outside make up the basin of the running state. A typical fluctuation out of one trapped basin puts the system into the running state, not another trapped state.

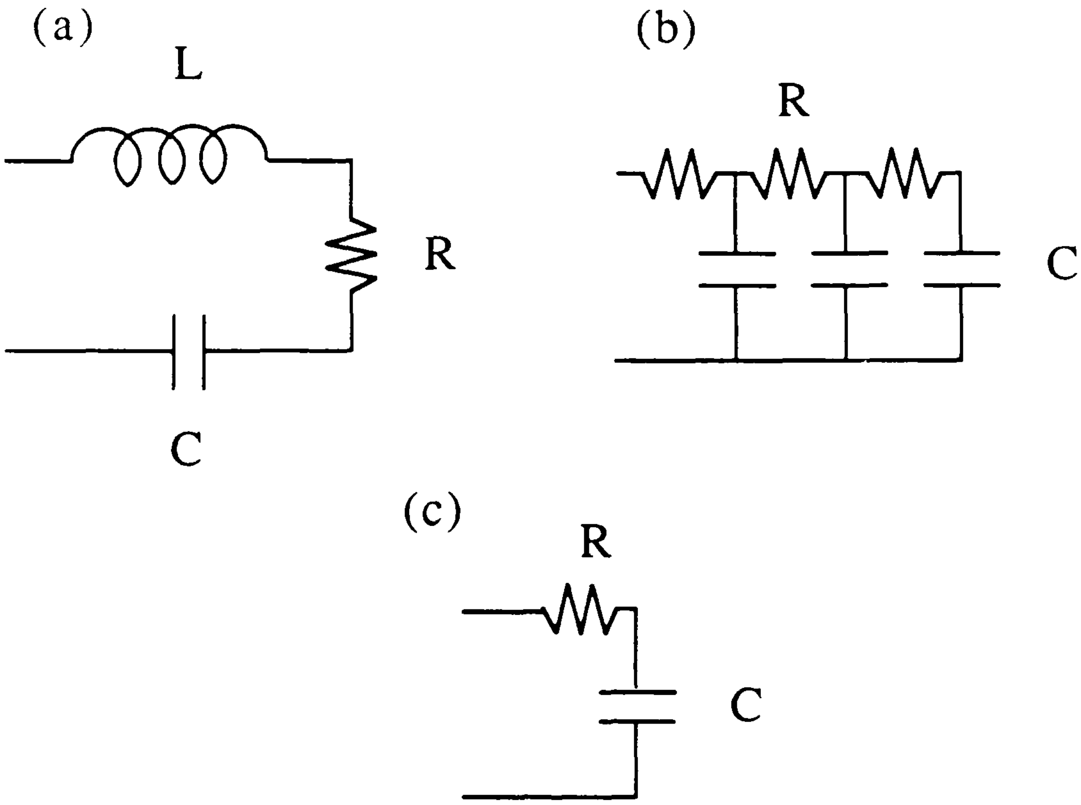

Fig. 5.9: Three model circuits for a transmission line discussed in this section.
(a): L-R-C combination used by Ono, et al. [1987]. (b): three-part ladder model, $R+(R+(R+C)\|C)\|C$, where + (||) indicates series (parallel). (c): $R+C$ combination used for the simulations of $I_r(T)$ (see Fig. 5.6). Only circuits (a) and (b) produce $R_0 > 0$ in analog simulations of the RCSJ-plus-line model with thermal fluctuations.

phase evolution on the low-voltage (here, a true zero-voltage) branch. The size of the hysteresis (i.e. I_c-I_r) decreased with increasing noise, eventually yielding noisy, non-hysteretic curves resembling the results of the theory of Ambegaokar and Halperin [1969] for junctions with $Q = 0$. We never saw a hysteretic IVC with $R_0 > 0$.

In the first attempt to simulate the R_0 branch using a RCSJ-plus-leads model, we added a series combination of a 20 Ω resistor and a 2 μF capacitor to simulate a line with $Z_0(\omega_p) << R_n$, R_L, as we had done in the simulations of I_{r0}. Surprisingly, the behavior was essentially identical to that of the pure RCSJ case. We did *not* see a hysteretic IVC with $R_0 > 0$.

The next step was to use a three-part ladder model of a line: $R+(R+(R+C)||C)||C$, where + and || indicate a series and parallel combination, respectively, and $1/\omega_p C \approx R = 20\ \Omega$ (see Fig. 5.9). This circuit *did* have a branch with $R_0 > 0$ over a wide range of noise current magnitude. For low noise, the voltage consisted of short pulses separated by long intervals with $V = 0$ (no phase evolution); increasing the current noise gave more continuously activated behavior. As expected given the incompatibility of $R_0 > 0$ with the RCSJ model, the phase point was never activated to the running state, which the hysteresis shows to be stable. Instead, the activation was to the basin of attraction for one of the two neighboring wells in the potential, which must more closely approach the basin of the original well in the new, higher-dimensional phase space of the system.

Our conclusion from these simulations is that at least two requirements must be met to produce an IVC with $R_0 > 0$, *within this modified RCSJ model*: first, the damping must increase greatly at high frequency, in order to prevent runaway after a phase slip; and second, the damping must have at least a minimum complexity. We speculate that the damping must have at least two poles, as in the *R*-*L*-*C* series combination used by Ono et al., which our simulations bracketed with one and three poles. To this point we have not done quantitative simulations of our junctions due to the difficulty of supplying "colored" noise (i.e. noise reflecting the frequency-dependent real part of the admittance presented by the junction plus line) to the simulator.

5.2.2 Numerical Results

It is difficult to predict the value of R_0 within the RCSJ-plus-leads model. The physics on the low-voltage branch is that thermal noise excites the phase point out of the potential well, and the point is retrapped after sliding one period (or perhaps several periods) down the potential. There has been little theoretical research into this problem when the damping is frequency-dependent.

The problem of the escape rate from a metastable equilibrium with barrier height $\Delta U >> kT$ and frequency-*independent* damping was solved by Kramers [1940]. His result was $\Gamma = \omega_A/2\pi \exp(-\Delta U/kT)$, where ω_A is a characteristic frequency ("the attempt frequency") that is a function of damping. For light damping ($Q > 1$, in the RCSJ model), $\omega_A = \omega_p$. We expect the Boltzmann factor to be unchanged for junctions with frequency-dependent damping, but it is unclear how ω_A is affected. Given ω_A, however, we can derive an expression for R_0 as outlined in the next paragraph.

Suppose the escape rate is $\Gamma = \omega_A/2\pi \exp(-\Delta U/kT)$, and consider an infinitesimal washboard tilt i (see Fig. 5.10). We allow activation in each direction and assume that φ slips one well (2π) per escape. The net velocity down the potential is $d\varphi/dt = \omega_A \exp(-\Delta U^+/kT)\{1-\exp((\Delta U^+-\Delta U^-)/kT)\}$, where ΔU^+ and ΔU^- are the barriers to escape down and up the potential, respectively. Since $\Delta U^+-\Delta U^- = hi/2e << kT$, we use a Taylor expansion for the second exponential. Using $R_0 \equiv V(i)/i = \hbar\varphi/2ei$, we obtain:

$$R_0 = \frac{h}{4e^2}\left(\frac{\hbar\omega_A}{kT}\right)\exp\left[-\frac{2E_J}{kT}\right] \quad . \tag{5.9}$$

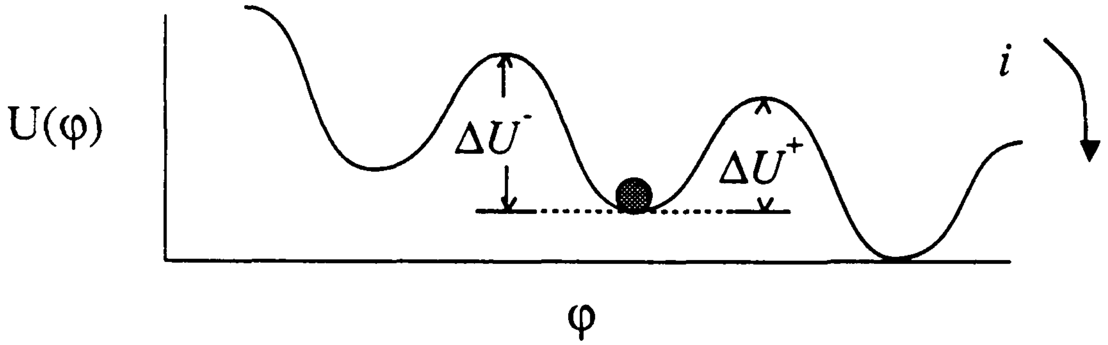

Fig. 5.10: The washboard with a small tilt. ΔU^{+} and ΔU^{-} are the barriers to escape with and against the potential tilt, respectively. When there is enough damping at high frequency to prevent runaway, we expect $V(i) = iR_0$, with R_0 given by (5.8).

We can adapt this procedure for any escape rate. For example, Barone, Cristiano, and Silvestrini [1985] have calculated Γ when the barrier is fairly small:

$$\Gamma = \frac{1}{RC}\left\{\sum_{n=1}^{\infty}\frac{1}{n!n}\left[\left(\frac{\Delta U}{kT}\right)^n - \left(\frac{E_0}{kT}\right)^n\right]\right\}^{-1} . \tag{5.10}$$

Here E_0 is a typical initial energy for the particle in the well. Its value is poorly determined, but when $\Delta U >> kT$, a reasonable value is $E_0 = kT$.

This expression should be accurate for the sample with $R_n = 520\ \Omega$, where lead and quantum effects are minimal. We convert it to a prediction for R_0 by:

$$R_0 = \frac{h}{2ei}\left[\Gamma^+(i) - \Gamma^-(i)\right] , \tag{5.11}$$

where i is a small current, and Γ^+ and Γ^- are the escape rates down and up the potential, respectively. This theory is compared to data in Fig. 5.11. The agreement is excellent.

At low temperature, the intermediate and large-R_n samples have $\Delta U >> kT$ and measurable R_0, allowing comparison with the Kramers prediction that R_0 vanishes exponentially as $T \to 0$. As shown in Fig. 5.12, however, the data level off at low T, proving the existence of non-activated escape.

This is an observation of the effect of quantum fluctuations on these samples. Adding quantum mechanics to the model enhances the escape rate from the potential well above the classical prediction. For samples with $E_J > E_C$, the data agree well with the escape rate calculated using clasical and MQT theory [Iansiti, et al., 1989]. In Fig. 5.13 we show data and theory for $R_0(T)$ for the 14.8 kΩ sample.

We have assumed in the calculation that the effect of damping by the leads is twofold. First, it traps φ after a 2π slip. Second, the damping is not so large as to overdamp the junction, which would inhibit both thermal activation and quantum tunneling,

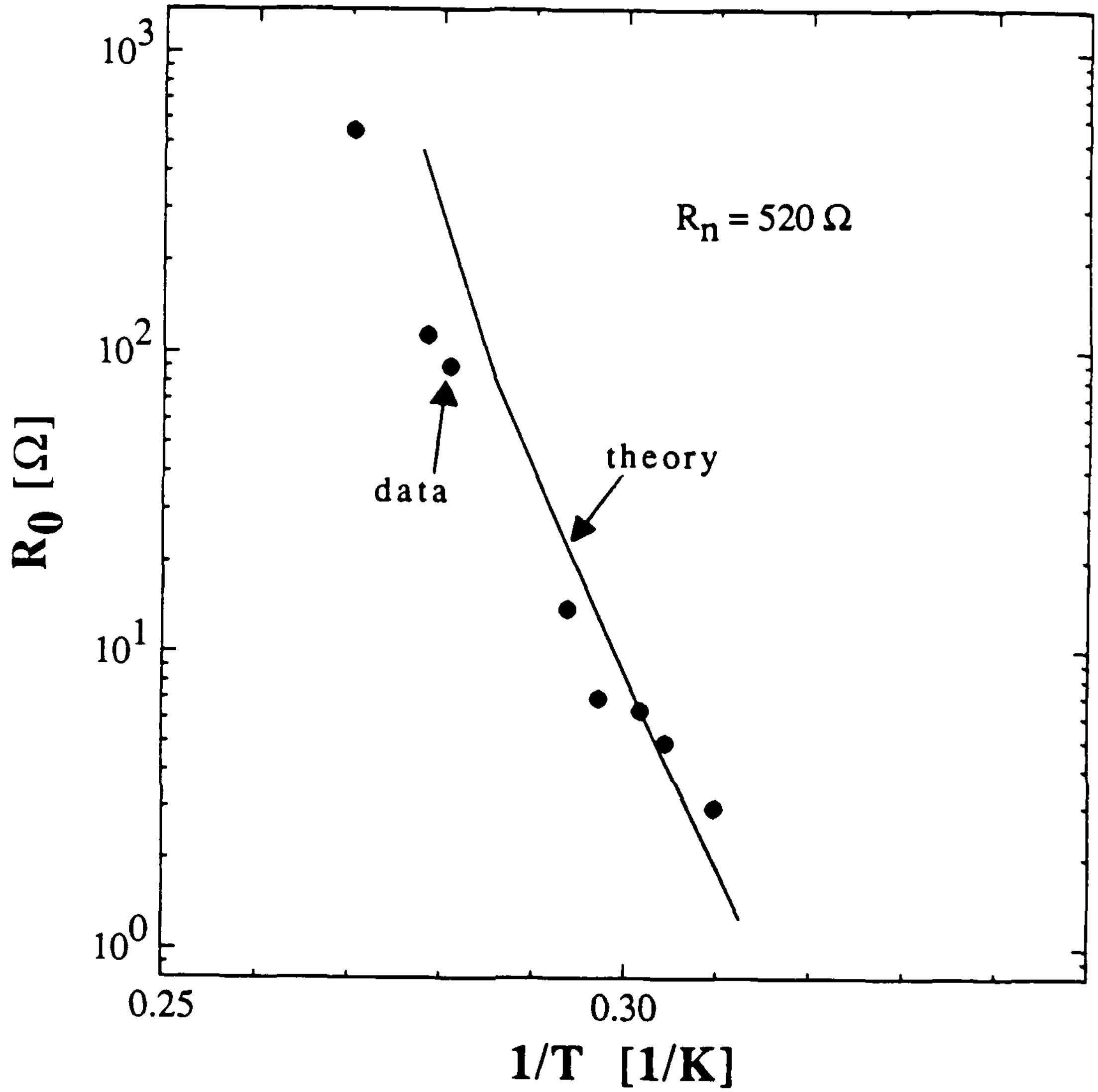

Fig. 5.11: R_0 vs. $1/T$, data and theory, for the sample with $R_n = 520\ \Omega$. The solid dots are data. The line is the prediction of a theory discussed in the text.

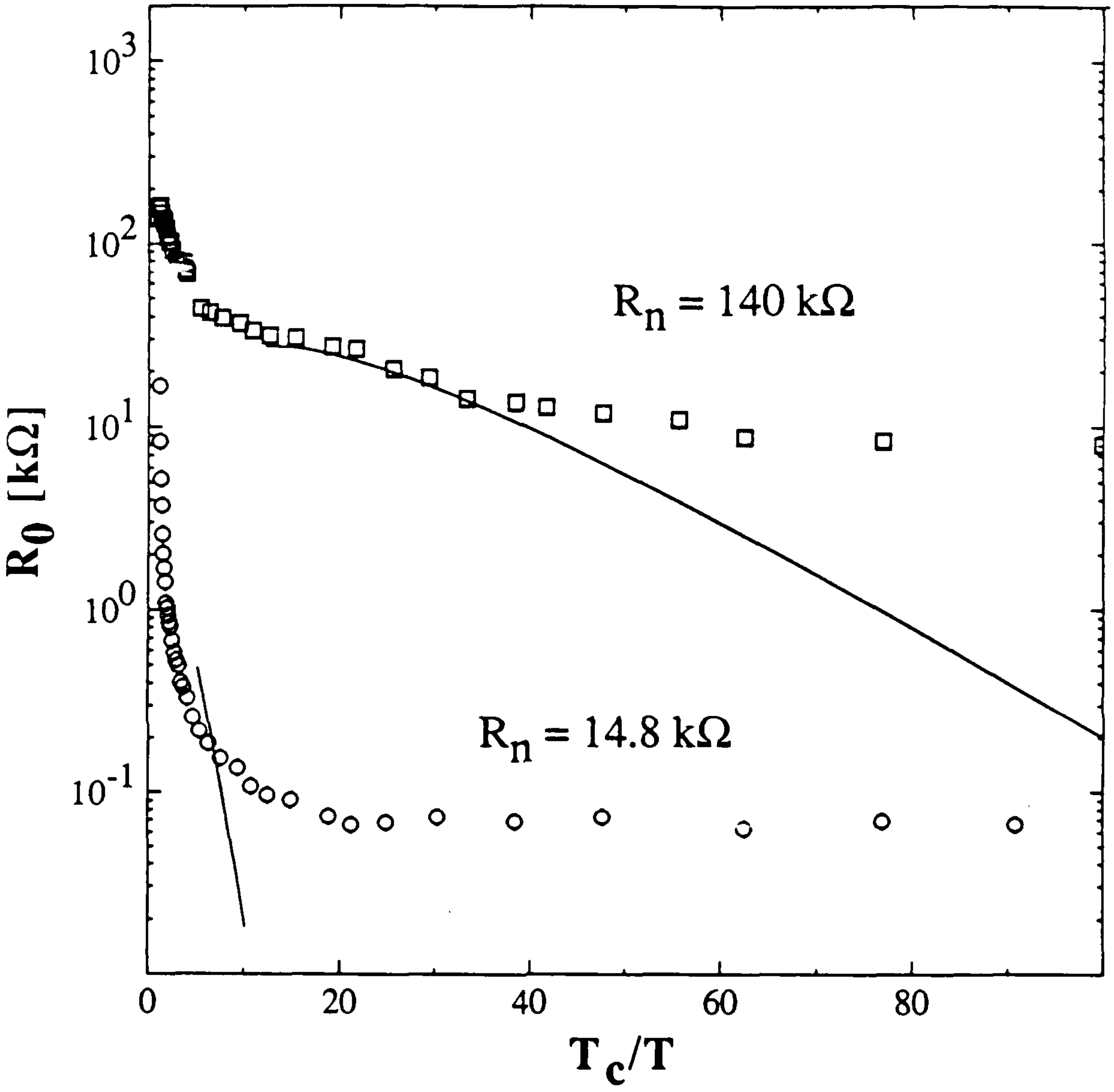

Fig. 5.12: $R_0(T_c/T)$ data and classical theory for the samples with R_n = 140 kΩ (squares) and 14.8 kΩ (circles). The solid lines are the predictions of a classical theory described in the text. As $T \to 0$, the predictions vanish exponentially as the Boltzmann factor $e^{-\Delta U/kT}$. The data level off due to the effect of quantum fluctuations of φ.

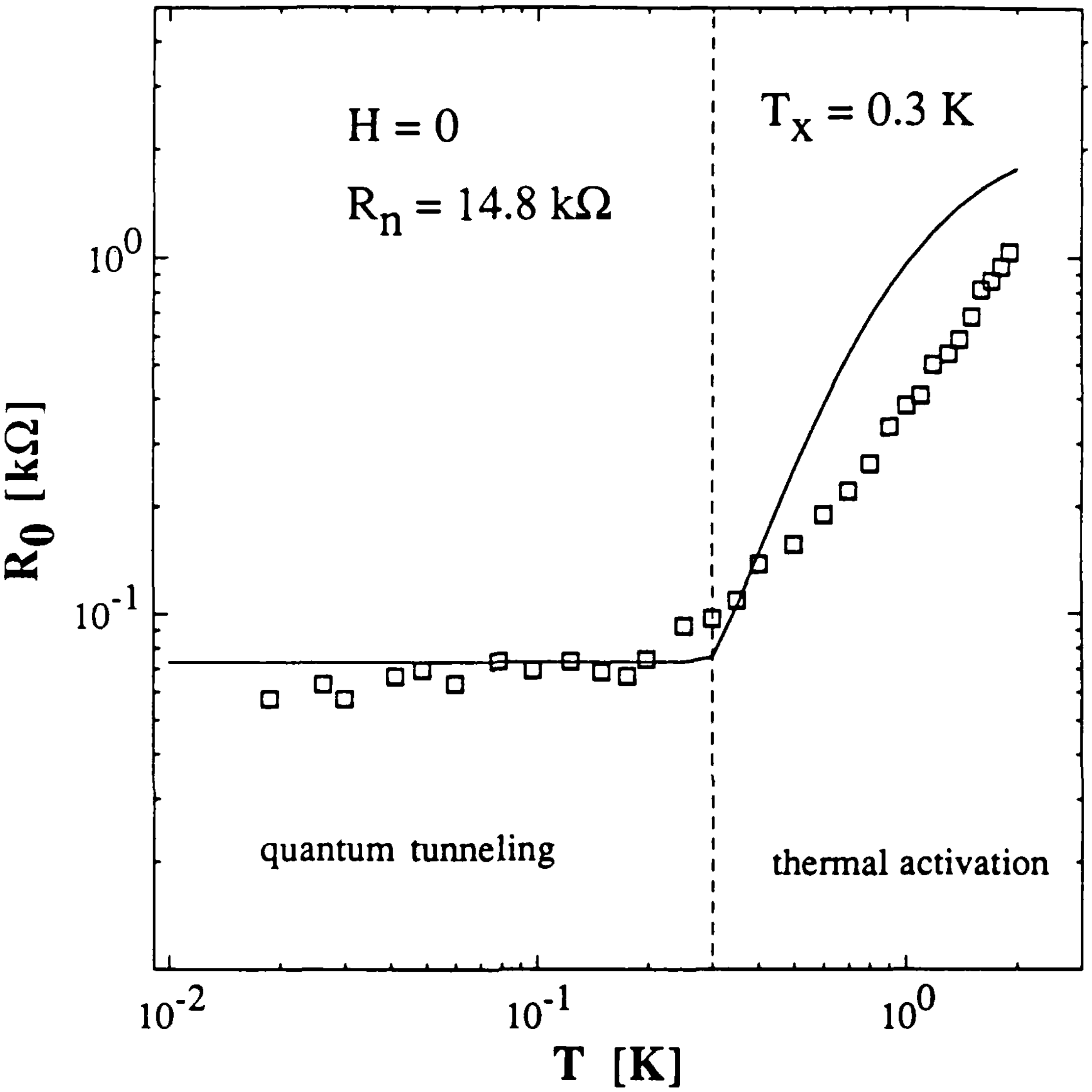

Fig. 5.13: $R_0(T)$ data and theory for the sample with R_n = 14.8 kΩ, in zero magnetic field. The data are the open squares. The line is a theory described in the text. In the vicinity of the crossover temperature, $T_{xo} \approx 0.3$ K (dotted line), the escape rate goes from thermally activated behavior to its low temperature limit, predicted by MQT theory.

but is sufficient to keep the junction out of the extremely underdamped regime ($Q >> \Delta U/kT$, which would be the case if the damping were only due to quasiparticle tunneling), where thermal activation is reduced by slow equilibration of φ to the bath temperature. We assume that the leads have no other effect upon the escape rate.

The $T = 0$ escape rate due to quantum tunneling is [Caldeira and Leggett, 1981]:

$$\Gamma_{qm} = \frac{\omega_p}{2\pi}\left[12\pi\sqrt{6}\right]\sqrt{\frac{\Delta U}{\hbar\omega_p}}\exp\left(-\frac{36}{5}\frac{\Delta U}{h\omega_p}\right) \tag{5.12}$$

Above the crossover temperature between quantum tunneling and thermal activation, $T_{xo} = \hbar\omega_p/2\pi k$, we calculate the escape rate with the Kramers form for the usual RCSJ model in the underdamped regime. In each case the conversion from escape rate to R_0 is made using the argument leading to (5.9). The agreement between data and theory is very good. Moreover, as shown in Fig. 5.14, data for $R_0(T)$ from the same junction with I_{c0} reduced by a magnetic field do not level off at low temperature, arguing that extraneous noise is not causing these observations.

Martinis and Kautz [1989] assumed that φ slipped several wells after each escape to fit their data, which agreed with their computer simulations. In contrast, our data for $R_0(T)$ agrees well with analytic calculations assuming single-well slips. This could be due to the significantly larger damping at high frequency in our samples, which suppresses multiple-well slips (our $Z(\omega_p) \approx 100\ \Omega << \sim 5000\ \Omega$ for Martinis and Kautz).

5.3 The Critical Current

For the moment, assume that the value of R_0 is known; in the previous section, we showed that, for our samples, its value is roughly what we would calculate using Kramers' theory (or, if appropriate, MQT theory) for the escape rate from the potential well and the

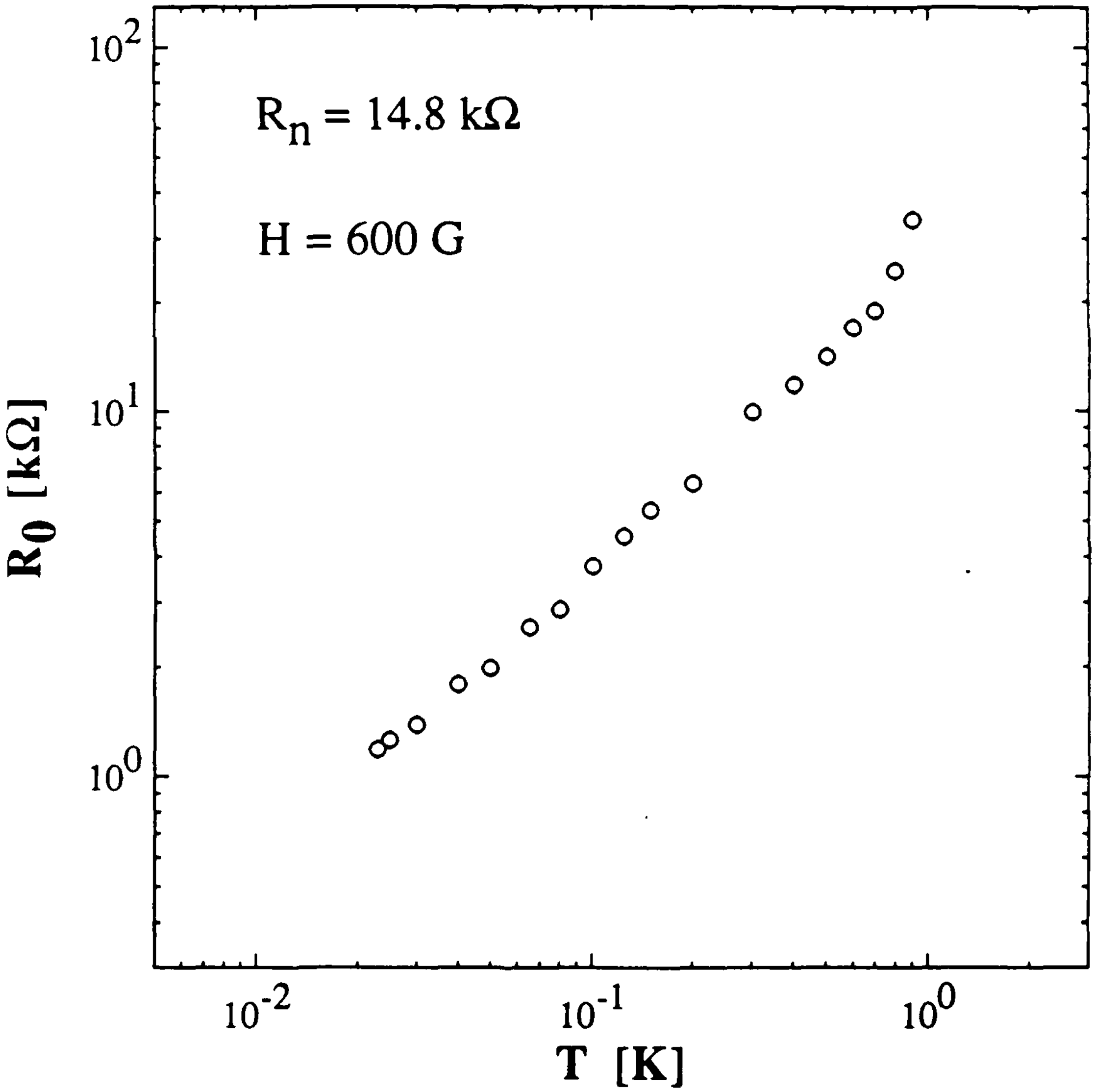

Fig. 5.14: $R_0(T)$ data for the sample with $R_n = 14.8$ kΩ in an applied magnetic field $H = 600$ G. The data appear thermally activated over the entire temperature range, suggesting that the low-temperature plateau observed in the data with $H = 0$ (Fig. 5.13) is *not* due to extraneous noise.

assumption that φ slips 2π per escape event. If R_0 is known, we can apply to I_c some of the arguments developed in section 5.1.

I_c, like I_r, is determined by damping. This is indicated both by the phase evolution on the low-voltage step and the narrow critical current distribution observed in our experiments. The phase point is activated frequently out of the potential well, and only the high frequency damping prevents runaway (a voltage switch to $2\Delta/e$). At a large enough tilt, this braking is not sufficient, and φ runs free. Unlike premature switching in the standard RCSJ model with noise, this runaway is *not* the result of a single rare escape, so we expect a narrow distribution of measured critical currents. As long as we can interpret I_c as the current at which the system switches from one type of motion (hopping down the potential) to another (runaway), we can apply the energetic argument that led to the estimate of $I_r(T)$.

The (dc) power input to the junction is $IV(I) \approx I^2 R_0$. This power must be dissipated as φ hops down the potential. If the characteristic frequency of a hop is ω_p, an estimate of the power dissipated is $I_{c0}{}^2\mathrm{Re}[Z(\omega_p)]/2$, where $Z(\omega)$ is the impedance presented by the combination of the junction capacitance, the quasiparticle channel, and the leads. Assuming that runaway (the measured I_c) occurs when the dc input power exceeds this upper bound, and that the high-frequency line impedance is $G_{ac} >> R_L{}^{-1}, R_n{}^{-1}$, we obtain:

$$I_c^2 R_0 = \frac{I_{c0}^2 G_{ac} / 2}{G_{ac}^2 + \omega_p^2 C^2} \quad . \tag{5.13}$$

The relation (5.10) predicts that

$$\left(\frac{I_c}{I_{c0}}\right)^2 R_0 = R' = \frac{G_{ac} / 2}{G_{ac}^2 + \omega_p^2 C^2} \quad , \tag{5.14}$$

where R' should be about 50 Ω for each of our samples, since $\omega_p C \approx (10^{11}$ rad/sec)x (10^{-15} F) = 0.0001 $\Omega^{-1} << G_{ac} \approx 0.01\ \Omega^{-1}$. Fig. 5.15 is a plot of I_c/I_{c0} versus R_0 for a number of samples. The trend $(I_c/I_{c0})^2 R_0$ equals a constant is followed relatively well, but the data is best fit by $R' = 6\ \Omega$, about one tenth the predicted value. The deviation from this form at high R_0 (high T) is due to the disappearance of hysteresis in the IVC. Beyond this point, there is no switching from hopping to runaway motion at I_c, but rather some averaging between the two states. We no longer expect our energy arguments, dependent on the switching, to apply.

Guided by this reasoning, we can analyze the data of other workers. The IVC published by Ono et al. [1987] (their Fig. 1) has $I_{c0} = 20$ nA, $I_c = 1.3$ nA, and $R_0 = 6$ kΩ, so that $(I_c/I_{c0})^2 R_0 = R' = 25\ \Omega$. The junction in this experiment, like ours, had no special transmission line patterned onto the chip; the high frequency line impedance is about 100 Ω. Since their $\omega_p C \approx (10^{11}$ rad/sec)(10^{-14} F) = 0.001 Ω^{-1} is negligible compared to the line admittance, (5.14) predicts R' should be the same as for our samples. Although their value of 25 Ω is a bit above the best fit to our data (6 Ω), their measured $(I_c/I_{c0}, R_0)$ pair lies within our data's scatter, as indicated in Fig. 5.15. Moreover, their measured R' agrees well with the prediction of (5.14).

Finally we turn to the data of Martinis and Kautz [1989], who used very resistive on-chip circuitry as a well characterized high-frequency environment for their sample. They were able to fit the R_0 and I_c data nearly exactly with a complicated computer simulation, which included a multipart lumped-component approximation to the line. Their sample B had the reentrant $I_c(T)$ common to our samples. The two IVCs with $T = 1.27$ K and 2.1 K in their Fig. 2 lie in the temperature range below the local minimum in I_c for which our relation between I_c and R_0 holds. For both these curves $I_{c0} = 50$ nA, and $C = 20$ fF. The 1.27 K curve has $I_c = 1.23$ nA and $R_0 = 4.7$ kΩ; for the 2.1 K curve, $I_c = 1.17$ nA and $R_0 = 11$ kΩ. The values of $(I_c/I_{c0})^2 R_0$ are 3 Ω and 6 Ω respectively.

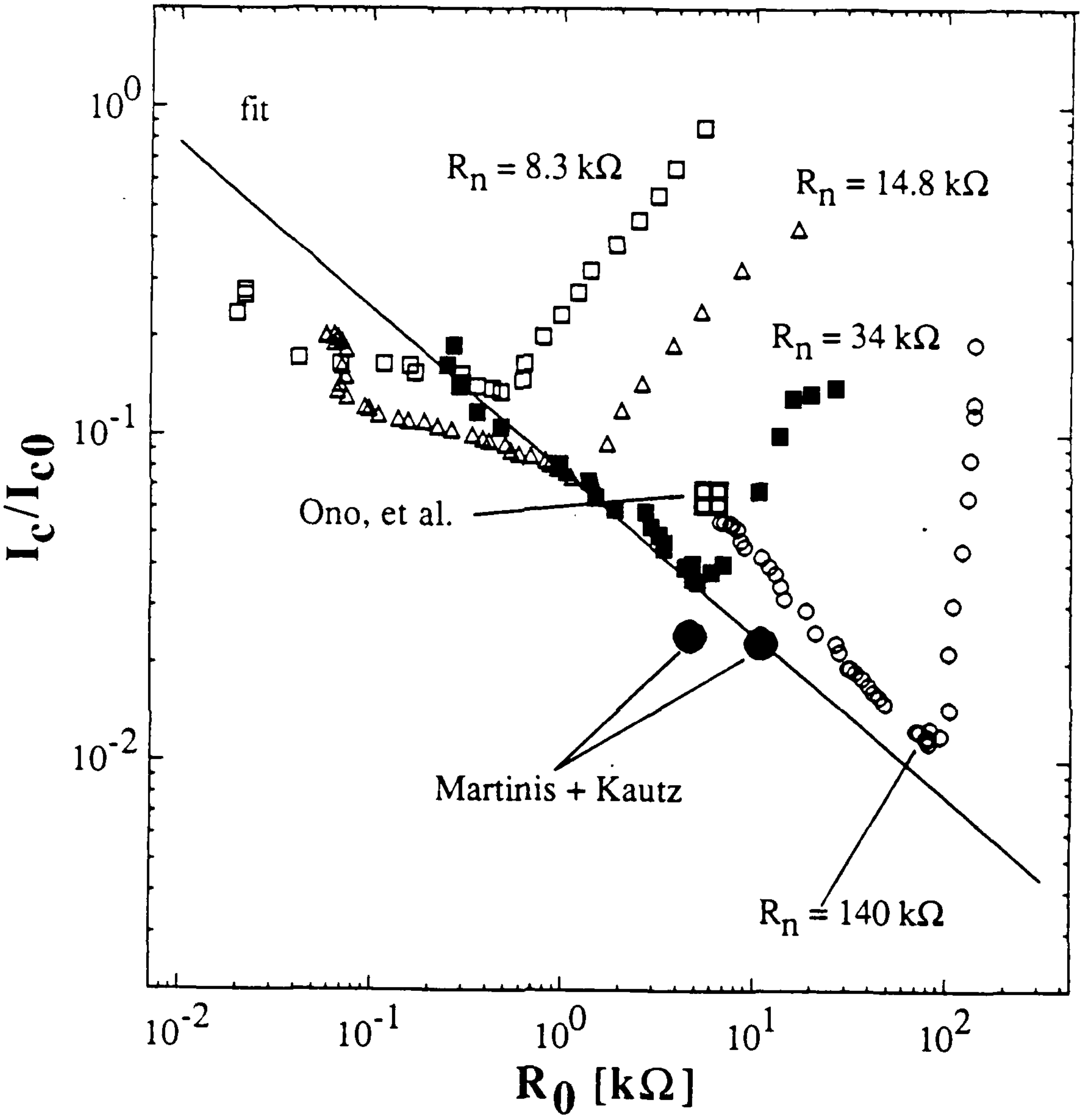

Fig. 5.15: I_c/I_{c0} vs. R_0 for four junctions from this work and samples of other authors. The open squares, triangles, solid squares, and circles are data from the samples with R_n = 8.3, 14.8, 34, and 140 kΩ respectively. The large solid circles and box are data taken from Martinis and Kautz [1989], and Ono, et al. [1987]. The solid line is a rough fit to the data, $(I_c/I_{c0})^2 R_0 = 6\ \Omega$.

This sample is different from ours and that of Ono, et al. Patterned onto the chip is an extremely resistive line connected to the junction. Martinis and Kautz estimate its resistance and stray capacitance as $r = 200\ \Omega/\mu\text{m}$ and $c = 50\ \text{aF}/\mu\text{m}$; even at $\omega_p/2\pi = 14$ GHz, the line's inductance is negligible.[§] Ignoring the inductance, the line impedance at ω_p is $4800\ \Omega$ (cf. our $100\ \Omega$). Unlike our sample, here it is the *line* admittance, not $\omega_p C$, that is negligible in the denominator of (5.14); for this junction, $\omega_p C \approx (10^{11}\ \text{rad/sec})(20\ \text{fF}) = 0.002\ \Omega^{-1} >> G_{ac} \approx 0.0002\ \Omega^{-1}$. Remarkably enough, evaluating (5.14) yields $R' = 30\ \Omega$, almost the same as the $50\ \Omega$ predicted for our samples, radically different though they are. As shown in Fig. 5.15, Martinis and Kautz's $(I_c/I_{c0}, R_0)$ pairs fall among our data, agreeing with the prediction that R' should be about the same as for our samples, despite the vastly different line configuration.

The experiment of Martinis and Kautz also illuminates some of the problems with the simple calculation of I_c. The only nominal difference between their samples A and B is the length of the resistive line attached to the junction. At ω_p, however, the admittance of the line is the same for both samples because each line is much longer than the extinction length l_x at that frequency.[†] The two samples have equal R_0 at each temperature; (5.14) predicts that they should have the same I_c, but that of sample A is consistently higher.

Although not predicted by our simple view of the junction dynamics which leads to (5.14), this result is in accord with the intuition that damping controls I_c. The line of each sample looks open at low frequencies, and their impedances are equal at high frequencies when l_x is much less than either line length. In between these two regimes, the damping in sample A is greater. Therefore, its I_c should be larger, as borne out by the experiments. The simple assumption, that only $Z(\omega_p)$ is relevant, ignores the complex motion that φ undergoes due to thermal noise. In the case of I_r in the absence of noise, the strictly periodic phase motion justifies the assumption that only circuit parameters at dc and ω_J are important. It is not so accurate for the case of I_c in the presence of noise. The approximate procedure is useful, however, contains the essential physics of this phenomenon, and might be extended to predict the dependence of I_c on the damping in a wide frequency range.

[§] $\omega_p l \approx (10^{11}\ \text{rad/sec})(200\ \text{fH}/\mu\text{m}) = 0.02\ \Omega/\mu\text{m}$ may be ignored in comparison to $r = 200\ \Omega/\mu\text{m}$. The inductance becomes important only at $\omega \approx (200\ \Omega/\mu\text{m})/(200\ \text{fH}/\mu\text{m}) = 10^{15}$ rad/sec, well above the superconducting energy gap of niobium or any other relevant frequency.

[†] The extinction length is roughly the length of line that has dc resistance equal to the line impedance. Here that is about 25 μm, in contrast with the 500 μm and 1.5 mm line lengths for the two samples.

5.4 Summary

In this chapter, we noted that the usual RCSJ model is incompatible with two phenomena common to our samples: the flat minimum in $I_r(T)$ at low T, and the existence of hysteretic IVCs with $R_0 > 0$ on the low-voltage branch. This motivated a new RCSJ-plus-leads model, which accounts for high-frequency losses in the leads.

The model agrees well with the $I_r(T)$ data. We cannot make a complete quantitative comparison with the $R_0(T)$ data, due to the lack of theoretical work on escape from a potential well with a small barrier and frequency-dependent damping. The data agree well with calculations that include the crossover from quantum tunneling to thermal activation, assuming that φ slips one well per escape. We have also argued that general energetic considerations account for the relationship $(I_c/I_{c0})^2 R_0 =$ constant that characterizes most of the data. The predictions of the energy argument also agree with data from other groups.

Chapter Six

Conclusions and Suggestions for Future Work

The standard RCSJ model of the Josephson junction was suggested by McCumber in 1968. Through the last 22 years, experiments on these devices have repeatedly provided exciting new results, whose explanations have required the consideration of an ever expanding list of physical phenomena. To this list, which includes macroscopic quantum tunneling (MQT) [Martinis, et al., 1987], chaos [Hu, 1987], and thermal activation over a barrier [Fulton and Dunkleberger, 1974], we now add frequency-dependent damping and the physics of the quantum rotor coupled strongly to its environment.

We began this work not only with the goal of exploring these ideas, but also with faith that a novel part of the device parameter space would hold the same richness that infused the work of earlier experimenters. Our investigations, driven by the development of electron beam lithography at Harvard, led to unexpected and stimulating discoveries. We summarize them here, along with our conclusions and suggestions for future work.

In this report, three types of behavior have been suggested for φ, the order parameter phase difference between the electrodes of a Josephson junction. We can call these classes "classical," "MQT-like," and "purely quantum mechanical."

This division is certainly arbitrary. The correspondence principle dictates that "classical mechanics" *is* quantum mechanics of the full Hamiltonian of φ plus the environment, in the large quantum number limit. By "classical," we mean that negligible errors result from the approximation that φ is a sharp variable, undergoing damped dynamics in the cosinusoidal potential. The damping is strongly frequency-dependent in our samples, and in any large-R_n sample, at low T, connected directly to leads.

"MQT-like" behavior is quantum mechanics in the limit where the bandstructure is tight-binding-like (flat bands, separated by energy $\hbar\omega_p$), and the wavefunction $\psi(\varphi)$ has width much less than 2π, but much larger than the rms fluctuations predicted by equipartition, $\delta\varphi_{rms} = (kT/E_J)^{1/2}$. In the samples of previous MQT studies, the phase tunnels from the potential well into a running state. If the MQT picture applies to our samples, the tunneling is into a metastable state in a neighboring well, and, since that state is not at the same energy as the initial state for a small current (washboard tilt), the tunneling is inelastic.

By "purely quantum mechanical," we mean that both these approximations do not apply. Specifically, there exist effects due to a band structure that is not flat and has gaps separating the bands. If the gaps are not effective, the system acts like a normal junction in the large charging energy limit.

In our experimnents, the first two behaviors have been observed clearly; the evidence for the third is suggestive but not convincing.

Many of our measurements agree with the classical approximation in the presence of frequency-dependent damping. Moreover, the results differ qualitatively from those of the standard RCSJ model. One striking change is documented in the $I_r(T)$ data. At high temperature, the measured retrapping current is enhanced above the RCSJ value by dissipation in the leads. As $T \rightarrow 0$, I_r reaches a constant, non-zero value (in contrast to the exponentially vanishing $I_r(T)$ predicted by the RCSJ model), due to the existence of the small high-frequency impedance of the leads and pair-breaking quasiparticle tunneling at $V = 2\Delta/e$, two sources of dissipation that do not vanish at low temperature.

A non-zero R_0, not expected in the usual RCSJ model, is explained by the inclusion of frequency-dependent damping. The existence of phase-evolution on the low-voltage branch implies that the measured critical current is no longer determined by a single, fluctuation-driven escape (as in the underdamped RCSJ model), but is now dependent upon *damping*. We have proposed an energy balance argument which leads to a simple calculation for I_c in a hysteretic IVC, given R_0 and the high-frequency embedding impedance. The predictions agree fairly well with our data, as well as data from other groups. Some of these latter data are from samples whose high frequency environment is much different from that of our own, making them a good test of the theory.

It is difficult to make quantitative predictions for $R_0(T)$, since the barrier to activation in our samples is often small, that is, $\Delta U = 2E_J$ is only slightly larger or even smaller than kT. No reliable theory for this regime exists. Moreover, no theory exists for the effect of frequency-dependent damping on the escape rate. If we assume that the leads limit the slip to 2π when the phase point escapes from the well, but have no effect on the escape rate itself, our $R_0(T)$ data for low-R_n samples (which have $\Delta U >> kT$ for T not too close to T_c) agree well with the Kramers theory for thermal activation. R_0 decreases exponentially with decreasing T, until it is below our minimum resolution.

The intermediate and large-R_n samples have $\Delta U >> kT$ at sufficiently low temperature, allowing comparison to Kramers' theory. It predicts an exponentially vanishing $R_0(T)$ as $T \rightarrow 0$, but the observed $R_0(T)$ levels off, suggesting the effect of quantum fluctuations of φ. Once again, assuming that the leads retrap φ after a 2π slip and have a negligible effect on the escape rate itself, the data agree well with the escape rate predicted by MQT theory in those samples with E_J not too much larger than E_C, where this theory should be most applicable. $R_0(T)$ data from a junction with I_{c0} reduced by a magnetic field do not level off at low T, arguing that extraneous noise is not the source of these observations.

We now turn to the question of purely quantum mechanical behavior, the theory of which was sketched in chapter 2. The strongest evidence for such behavior is the resemblance between curve "$kT/E_C = 0.5$" in Fig. 2.7, a theoretical IVC for a Josephson junction with quasiparticle tunneling and thermal fluctuations, and the IVC of the 140 kΩ junction Fig. 1.5. In each, $V(I)$ increases rapidly for small currents, and then levels off at $V \approx e/2C$. After the plateau, the theoretical $V(I)$ approaches that of a junction with $I_{c0} = 0$, over a narrow current range. Similarly, the measured IVC has a discontinuous jump to the quasiparticle characteristic at $I = I_c$.

It is unlikely that classical dynamics could lead to an IVC like the one measured. Had we observed the predicted current steps in the IVCs with an added ac field (Figs. 4.12, 4.13, and 4.14), however, our claim of quantum behavior would be considerably stronger. The ac-driven IVCs do not resemble the predictions of either classical or quantum theory. Further simulation (both analog and digital) of the RCSJ-plus-line model with fluctuations, in the limit of small I_{c0}, is needed to rule out the possiblity of a classical explanation. Understanding is also needed of the effect of leads on the quantum theory. Present theories of N-I-N tunneling with frequency-dependent damping [Cleland, et al., 1990; Devoret, et al., 1990] may provide some guidance.

Given our results, clear avenues for future research exist. First, more convincing evidence of the quantum mechanical regime is needed. It is possible that the leads' high frequency damping, and the noise current associated with it through the fluctuation-dissipation theorem, are modifying the junction behavior. Cleaner observations of this regime might be made in samples with *integrated*, highly resistive leads, whose impedance in the gigahertz range, although much smaller than the dc impedance, can be much greater than the usual 100 Ω [Martinis and Kautz, 1989]. Unfortunately, even a small measuring current passing through such resistive leads can weaken the desired quantum dynamics by heating the sample, especially at dilution refrigerator temperatures where heat-sinking is difficult.

Heating can be avoided if the blocking impedance is lossless, e. g. due to other low-capacitance junctions. Recent work by another group on arrays of Al junctions [Geerligs, et al., 1989] has produced IVCs with a negative-dynamic-resistance region much like that predicted by the quantum junction theory, when interband transitions due to Zener tunneling and thermal activation are negligible. Experiments done at Harvard on Sn arrays, however, show no such behavior.† The IVCs for these arrays in zero-field resemble those of single junctions in the classical and MQT-like regimes.

After confirmation of the quantum regime, the next logical step is to observe the Bloch oscillations directly, both through phase-locking to an ac signal, and detecting the voltage oscillations associated with the coherent Cooper pair transfer. An elegant approach to the second objective would be to detect with one junction the Bloch oscillations occuring in another, analogous to Giaver's famous experiment, in which Josephson oscillations in one junction led to detectable photon-assisted-tunneling steps in a second [Giaever, 1965].

Further research is needed on the device applications of these effects. Likharev and Zorin [1985] have suggested that Bloch oscillations, phase-locked to a microwave field ($v_B = I/2e$), be used in a superconducting current standard, just as synchronized Josephson oscillations ($v_J = 2e/\hbar$) define the standard volt. The quantum Hall effect ($V = hI/ne^2$, n an integer) would close the "quantum metrological triangle" (see Fig. 6.1). Comparison of the results of the three experiments would tell whether a deviation exists from the fundamental relations. Initial work towards this goal has so far exploited only the incoherent tunneling of *normal* electrons [Geerligs, et al., 1990]. The steps in the IVC were noise-rounded, precluding the use of the device as a current benchmark.

In conclusion, using electron beam lithography and dilution refrigeration, we have studied Josephson junctions with small geometric capacitance and large normal resistance. The assumption of the usual RCSJ model that the leads can be ignored is no longer valid; this has a profound effect on the junction IVC. We have strong evidence that quantum fluctuations of the phase, also neglected in the RCSJ model, are important at low temperature. We have presented a number of semiquantitative methods to predict the important quantities I_c, I_r, and R_0. Finally, we have suggested several intriguing areas for

---

† T. S. Tighe, private communication.

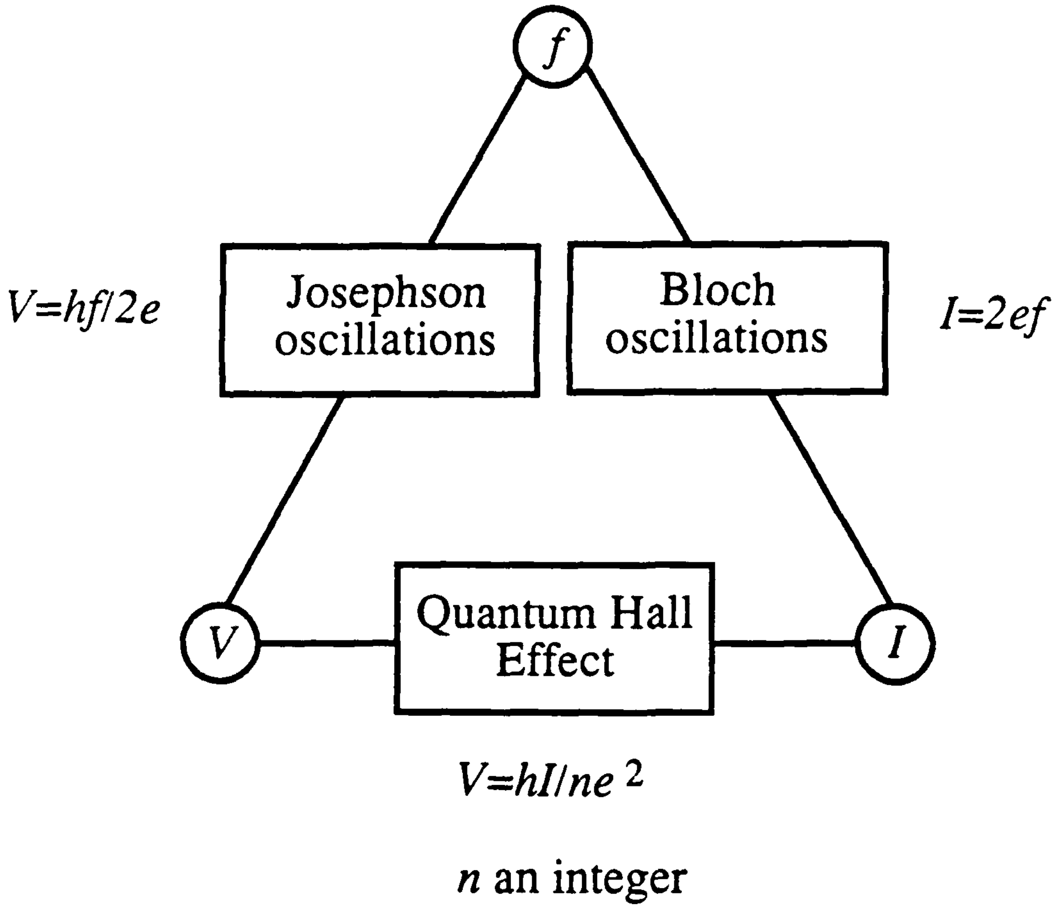
f
$V=hf/2e$
Josephson oscillations
Bloch oscillations
$I=2ef$
V
Quantum Hall Effect
I
$V=hI/ne^2$
n an integer

Fig. 6.1: The quantum metrological triangle. DC voltage and current standards are made by synchronizing Josephson and Bloch oscillations to a well-calibrated frequency source. These standards can be compared using the quantum Hall effect, $V = hI/ne^2$, n an integer. Any discrepancy arising in the experiment indicates that at least one of the three fundamental relationships is inexact. Adapted from Likharev and Zorin [1985].

further work, especially the need for theoretical insight into the impact of frequency-dependent damping on both thermal activation and quantum tunneling.

References

Akoh, H., O. Liengme, M. Iansiti, M. Tinkham, and J. U. Free, Phys. Rev. **B33**, 2038 (1986).

Ambegaokar, V. and A. Baratoff, Phys. Rev. Lett. **10**, 486 (1963).

Ambegaokar, V. and B. I. Halperin, Phys. Rev. Lett. **22**, 1364 (1969).

Ambegaokar, V., U. Eckern, and G. Schön, Phys. Rev. Lett. **48**, 1745 (1982).

Ashcroft, N. W. and N. D. Mermin, *Solid State Physics* (Saunders College, Philadelphia, 1976).

Averin, D. V. and K. K. Likharev, J. Low Temp. Phys. **62**, 345 (1986).

Averin, D. V. and K. K. Likharev, IEEE Trans. Magn. **23**, 1138 (1987). .

Averin, D. V. and K. K. Likharev, "Single Electronics: A Correlated Transmission of Single Electrons and Cooper Pairs in Systems of Small Tunnel Junctions", in *Quantum Effects in Small Disordered Systems*, ed. B. L. Altshuler, P. A. Lee, and R. A. Webb, to be published.

Averin, D. V., A. B. Zorin, and K. K. Likharev, Zh. Eksp. Teor. Fiz. **88**, 692 (1985) [Sov. Phys. JETP **61**, 407 (1985)].

Barone, A., R. Cristiano, and P. Silverstrini, J. Appl. Phys. **58**, 3822 (1985).

Basavaiah, S. and J. H. Greiner, J. Appl. Phys. **47**, 4201 (1976).

Ben-Jacob, E. and Y. Gefen, Phys. Lett. **108A**, 289 (1985).

Ben-Jacob, E., D. J. Bergman, B. J. Matkowsky, and Z. Schuss, Phys. Rev. **A26**, 2805 (1982).

Ben-Jacob, E., E. Mottola, and G. Schön, Phys. Rev. Lett. **51**, 2064 (1983).

Bracewell, R. N., *The Fourier Transform and Its Applications* (McGraw-Hill, Inc., New York, 1978).

Broers, A. N., W. W. Molzen, J. J. Cuomo, and N. D. Wittels, Appl. Phys. Lett. **29**, 597 (1976).

Broers, A. N., J. M. E. Harper, and W. W. Molzen, Appl. Phys. Lett. **33**, 392 (1978).

Büttiker, M., Phys. Rev. **B36**, 3548 (1987).

Caldeira, A. O., and A. J. Leggett, Phys. Rev. Lett. **46**, 211 (1981).

Chen, Y. C., Matthew P. A. Fisher, and A. J. Leggett, J. Appl. Phys. **64**, 3119 (1988).

Cleland, A. N., J. M. Schmidt, and John Clarke, Phys. Rev. Lett. **64**, 1565 (1990).

Danchi, W. C., Technical Report No. 23 (Tinkham series, Div. of Appl. Sci., Harvard University, 1983).

Danchi, W. C., J. Bindslev Hansen, M. Octavio, F. Habbal, and M. Tinkham, Phys. Rev. **B30**, 2503 (1984).

Delsing, P., K. K. Likharev, L. S. Kuzmin, and T. Claeson, Phys. Rev. Lett. **63**, 1180 (1989a).

Delsing, P., K. K. Likharev, L. S. Kuzmin, and T. Claeson, Phys. Rev. Lett. **63**, 1507 (1989b).

Devoret, M. H., J. M. Martinis, and J. Clarke, Phys. Rev. Lett. **55**, 1908 (1985).

Devoret, M. H., D. Estève, H. Grabert, G.-L. Ingold, H. Pothier, and C. Urbina, Phys. Rev. Lett. **64**, 1824 (1990).

Dolan, G. J., Appl. Phys. Lett. **31**, 337 (1977).

Dolan, G. J. and T. A. Fulton, IEEE Electr. Dev. Lett. **EDL-4**, 178 (1983).

Eckern, U., G. Schön, and V. Ambegaokar, Phys. Rev. **B30**, 6419 (1984).

Feynman, R. P. and A. R. Hibbs, *Quantum Mechanics and Path Integrals* (McGraw-Hill, Inc., New York, 1965).

Forrester, M., Technical Report No. 26 (Tinkham series, Div. of Appl. Sci., Harvard University, 1988).

Fulton, T. A. and G. J. Dolan, Appl. Phys. Lett. **42**, 752 (1983).

Fulton, T. A. and G. J. Dolan, Phys. Rev. Lett. **59**, 109 (1987).

Fulton, T. A. and L. N. Dunkleberger, Phys. Rev. **B9**, 4760 (1974).

Geerligs, L. J. and J. E. Mooij, Physica **B152**, 212 (1988).

Geerligs, L. J., M. Peters, L. E. M. de Groot, A. Verbruggen, and J. E. Mooij, Phys. Rev. Lett. **63**, 326 (1989).

Geerligs, L. J., V. F. Anderegg, P. A. M. Holweg, J. E. Mooij, H. Pothier, D. Esteve, C. Urbina, M. H. Devoret, Phys. Rev. Lett. **64**, 2691 (1990).

Giaever, I., Phys. Rev. Lett. **5**, 147 (1960).

Giaever, I., Phys. Rev. Lett. **22**, 904 (1965).

Guinea, F. and G. Schön, Europhys. Lett **1**, 585 (1986).

Gurvitch, M., M. A. Washington, and H. Huggins, Appl. Phys. Lett. **42**, 472 (1983).

Hatzakis, M., Appl. Phys. Lett. **18**, 7 (1971).

Hatzakis, M., J. Vac. Sci. Technol. **12**, 1276 (1975).

Howard, R. E., E. L. Hu, L. D. Jackel, L. A. Fetter, and R. H. Bosworth, Appl. Phys. Lett. **35**, 879 (1979).

Hu, Qing, Technical Report No. 25 (Tinkham series, Div. of Appl. Sci., Harvard University, 1987).

Hu, Qing, C. J. Lobb, and M. Tinkham, Phys. Rev. **B35**, 1687 (1987).

Hu, Qing, C. A. Mears, P. L. Richards, and F. L. Lloyd, Phys. Rev. Lett. **64**, 2945 (1990).

Iansiti, M., Technical Report No. 27 (Tinkham series, Div. of Appl. Sci., Harvard University, 1988).

Iansiti, M., Qing Hu, R. M. Westervelt, and M. Tinkham, Phys. Rev. Lett. **55**, 746 (1985).

Ianisit, M., A. T. Johnson, W. F. Smith, C. J. Lobb, and M. Tinkham, Jap. J. of Appl. Phys. **26**, Suppl 26-3, 1557 (1987a).

Iansiti, M., A. T. Johnson, W. F. Smith, H. Rogalla, C. J. Lobb, and M. Tinkham, Phys. Rev. Lett. **59**, 489 (1987b).

Iansiti, M., A. T. Johnson, C. J. Lobb, and M. Tinkham, Phys. Rev. Lett. **60**, 2414 (1988).

Iansiti, M., M. Tinkham, A. T. Johnson, Walter F. Smith, and C. J. Lobb, Phys. Rev. **B39**, 6465 (1989a).

Iansiti, M., A. T. Johnson, C. J. Lobb, and M. Tinkham, Phys. Rev. **B40**, 11370 (1989b).

Jackson, J. D., *Classical Electrodynamics* (Wiley and sons, New York, 1975).

Josephson, B. D., Phys. Letters **1**, 251 (1962).

Kirtley, J. R., C. D. Tesche, W. J. Gallagher, A. W. Kleinsasser, R. L. Sandstrom, S. I. Raider, and M. P. A. Fisher, Phys. Rev. Lett. **61**, 2372 (1988).

Kramers, H. A., Physica (Utrecht) **7**, 284 (1940).

Kratschmer, E. and M. Isaacson, J. Vac. Sci. Technol. **B4**, 361 (1986).

Li, Q., C. H. Watson, R. G. Goodrich, D. G. Haase, and H. Lukefahr, Cryogenics **26**, 467 (1986).

Likharev, K. K. and A. B. Zorin, J. Low Temp. Phys. **59**, 347 (1985).

Love, M. S. and A. C. Anderson, Rev. Sci. Instrum. **58**, 1113 (1987).

Mackie, S. and S. P. Beaumont, Solid State Technology, August 1985, 117 (1985).

Magerlein, J. H., Rev. Sci. Instrum. **49**, 486 (1978).

Martinis, John M. and R. L. Kautz, Phys. Rev. Lett. **63**, 1507 (1989).

Martinis, John M., Michel H. Devoret, and John Clarke, Phys. Rev. **B35**, 4682 (1987).

McCumber, D. E., J. Appl. Phys. **39**, 3113 (1968).

Ono, R. H., M. J. Cromar, R. L. Kautz, R. J. Soulen, J. H. Colwell, and W. E. Fogle, IEEE Trans. Magn. **MAG-23**, 1670 (1987).

Orr, B. G., H. M. Jaeger, A. M. Goldman, and C. G. Kuper, Phys. Rev. Lett. **56**, 378 (1986).

Rooks, M. J., S. Wind, P. McEuen, and D. E. Prober, J. Vac. Sci. Technol **B5**, 318 (1987).

Schmid, A., Phys. Rev. Lett. **51**, 1056 (1983).

Schön, G., Phys. Rev. **B32**, 4469 (1985).

Schön, G. and A. D. Zaikin, "Quantum Coherence Effects, Phase Transitions, and the Dissipative Dynamics of Ultra Small Tunnel Junctions," preprint.

Smith, Walter F., Technical Report No. 28 (Tinkham series, Div. of Appl. Sci., Harvard University, 1989).

Stewart, W. C., Appl. Phys. Lett. **12**, 277 (1968).

Tinkham, M., *Introduction to Superconductivity* (McGraw-Hill Inc., New York, 1975).

van Bentum, P. J. M., H. van Kempen, L. E. C. van de Leemput, and P. A. A. Teunissen, Phys. Rev. Lett. **60**, 369 (1988).

Van Duzer, T. and C. W. Turner, *Principles of Superconductive Devices and Circuits* (Elsevier North Holland Inc., New York, 1981).

van Wees, B. J., H. van Houten, C. W. J. Beenakker, J. G. Williamson, L. P. Kouwenhoven, D. van der Marel, and C. T. Foxon, Phys. Rev. Lett. **60**, 848 (1988).

Wang, T. C. and R. I. Gailey, Phys. Rev. **B18**, 293 (1978).

Wittels, N. D., in *Fine Line Lithography*, R. Newman, ed. (North-Holland, New York, 1980).

Zaikin, A. D. and I. N. Kosarev, Phys. Lett. **131A**, 125 (1988).

Zener, C., Proc. Roy. Soc. A, **145**, 523 (1934).

Appendix: Sample Fabrication Procedures

Cleaning substrates (suitable for new silicon wafers):

1. 5 minute ultrasonic in trichloroethylene (TCE).
2. 5 minute ultrasonic in acetone.
3. 5 minute ultrasonic in methanol. Steps 1-3 form the "T-A-M" cleaning process.
4. Blow dry.

Pad fabrication:

1. Spin Shipley 1400-27 photoresist at 4500 rpm for 45 seconds (~1.2 μm).
2. Bake 20 minutes at 70 C.
3. Soak 10 minutes in chlorobenzene.
4. Bake 10 minutes at 70 C.
5. Blow dry.
6. Expose 3.5 seconds with Karl Suss mask aligner.
7. Develop about 60 seconds with Shipley 351 developer. Remove a few seconds after the large open areas of the pads look clear. The undercut should be barely visible (~1 μm).
8. Evaporate about 50 Å Cr followed immediately by 450 Å Au. The cold trap must be used.
9. Liftoff with acetone. If undercut is produced, the liftoff is immediate.

Intermediate cleaning:

1. 30 minute in gently boiling photoresist stripper on hot plate.
2. 5 minute ultrasonic cleaning in 18 MΩ-cm water.
3. Dip in methanol. This must be done because water and TCE (step 4) react in an unpleasant manner.

4. 5 minutes ultrasonic "T-A-M" (See substrate cleaning section).

This thorough cleaning process is essential. Any photoresist residue on the pads will cause the pressed indium contacts to fall off the sample.

Sample fabrication with EBL:

1. Spin PMMA(MAA), 0.12 g/ml in acetic acid, at 2000 rpm for 60 sec.
2. Bake 60 min. at 180 C.
3. Spin PMMA [950 K mol. wt., 4 % in chlorobenzene] at 8000 rpm for 60 seconds.
4. Bake 60 min. at 180 C.
5. Expose in SEM. A silver paint contact to the Si substrate allows charge to flow off the sample. Typical exposure parameters: 12 keV electrons, beam current 4.5 pA, exposure time 250 μs/pixel at 1000X magnification.
6. Develop in IPA:MIBK, 1:3, until desired undercut is achieved. 10 minutes is typical. Inspect every 3 min. for best results. Rinse thoroughly with IPA.
7. Developed samples may be kept in fluoroware containers for several months without degradation. Undercut will increase slightly during this time.

Deposition:

1. Fasten the sample to the rotating evaporator stage. Screws must be tight enough to hold the sample, but not so tight that they crack the substrate.
2. Evacuate chamber. Check dc plasma oxidation wire for shorts to ground.
3. Pump overnight to achieve base pressure of cryopump (~1.5 x 10^{-7} T).
4. Run LN through the sample stage cooling line for 1 hour before deposition. Keep LN flowing during the entire deposition procedure. If the stage warms, the Sn films will be lumpy, and the lines discontinuous.

5. Tilt stage in one direction. Deposit first Sn layer *quickly* (about 300 Å/sec).
6. Flush chamber 3 times with 60 mT O_2 99.999 %.
7. With 30 mT pure O_2 in the chamber, apply 1100 V to the dc plasma wire. The plasma should glow bright blue. Keep the shutter *open* since the mean free path is larger than the shutter-sample distance. Oxidize for 1-10 min for samples with varying critical current densities. The oxide thickness seems to saturate after 10 min. Evacuate chamber before depositing second layer.
8. Tilt stage in other direction. Quickly deposit the second Sn layer.
9. Stop the LN flow. Warm the sample to room temperature before removing. One may wait overnight, or add N_2 exchange gas after about 1.5 hr. This reduces the total warm-up time to about 5 hours.

Deep ultraviolet (DUV) lithography:

1. Start with a Si wafer with the PMMA bilayer used for EBL (see the section "Sample fabrication with EBL").
2. Place wafer on the rubber membrane of the DUV chuck. Be sure the mask is flat on the chuck baseplate, not held up by the vacuum port hose barb.
3. Pump on the vacuum port. Watch the wafer contact the mask. If the wafer slides out of position, turn off the pump, and reposition the wafer.
4. Set the integrator control to "68", and turn on DUV source. With a new bulb, this exposure takes about 6 min.
4. Develop in IPA:MIBK, 1:3, for 60 seconds. Rinse thoroughly with IPA. The sample is now ready for EBL.

Canyon lithography:

1. Spin PMMA [950 K mol. wt., 6 % in chlorobenzene] at 2000 rpm for 60 seconds. This results in a *thick* layer, about 0.7 µm.

2. Expose in the SEM with a dose that purposefully *under*exposes the PMMA. Typical parameters: 35 keV electrons, beam current 47 pA, and exposure time 40 μs/pixel. The idea is to form a "canyon" in the resist, not a hole that extends all the way to the substrate.
3. Develop 60 seconds in IPA:MIBK, 1:3.
4. Evaporate 300 Å Cr at a 45° angle to the substrate and at least a 45° angle to any lines. Circles are not possible with this technique, but "Manhattan" geometries are.
5. Reactive ion etch in an O_2 plasma. This transfers the pattern to the substrate and creates the undercut. The longer the etch, the larger the undercut. Typical parameters in the old RIE system: 100 mT O_2, 30 W rf power in, 5 W reflected, etching time 10 min.
6. Metallize, and liftoff in acetone.

Acknowledgements

Many people have helped to make my stay at Harvard stimulating and productive.

I am fortunate to have had Prof. Michael Tinkham as a thesis advisor. From him I have learned my first lessons in how to think, write, and do science. Prof. Chris Lobb has served as a delightful sounding board for my ideas, half-baked and otherwise. Someday we *will* figure out how Weinberg gets that 2*e*.

All the other students who passed through the Tinkham/Lobb group in the last six years helped to create this thesis. Marco Iansiti was my main collaborator, as well as a loyal friend. His gentle encouragement carried me through many difficult moments.

I owe great thanks to the late Jim Gordon, who sold me on the superconductivity group with his great joy at tackling both experimental and theoretical challenges. Martin Forrester amazed me with his seemingly inexhaustible supply of information about photolithography and other arcane cleanroom arts. Qing Hu was a pleasant officemate and taught me the basics of the RCSJ model and Hunan cooking. He also built the analog simulator which proved so useful in this work. Walter Fox Smith deserves great credit for keeping the dilution refrigerator running while half a dozen other students (including me) stumbled through the low end of the learning curve. Gabriel Spalding, our closet materials expert, built the ion-beam sputtering system, a major contribution to the lab's facilities. Sam Benz has been a good friend, whom I can never forgive for making writing a thesis look so easy. Hu Jong Lee and Mark Rzchowski deserve special thanks and praise for acting as cleanroom "überczars" during their postdocs with the group.

Tom Tighe helped me keep my sanity by being the group's social leader. Keep those Friday parties alive! I enjoyed sharing Red Sox fanaticism with Li Ji and a lunchtime coffee habit with Ashraf Hanna. I expect to rely upon Hanna Enterprises, Unlimited for scientific instrumentation in the near future. Lydia Sohn's contagious humor was helpful in the last few (harried) weeks of writing this thesis. Rich Fitzgerald and Niraj Anand also

helped make these last weeks bearable by letting me look over their shoulders and kibitz when I needed a diversion from writing.

Horst Rogalla deserves special mention as a main contributor to the electron-beam lithography system. John Free, a "visitor" who has been here as long as I, contributed to numerous discussions of the RCSJ model. Clive Hayzelden kept our "dinosaur" SEM limping along for many years beyond its expected lifespan. Elizabeth Hemmingway's Thursday teas always provided a welcome and invigorating break. Erica Schulman, Charles Ahn, Dave Ephron, and Dan Lee collaborated with me in their under-graduate research projects. Their enthusiasm made the lab a brighter place. Dan Lee gets special thanks for helping to assemble this thesis.

I would like to thank my sister and brother. Their unwavering support is a source of inspiration and strength. Finally, I dedicate this work to my parents. Their love and confidence is the foundation upon which my life is built.

This research was supported in part by National Science Foundation Grant No. DMR-89-12927, Office of Naval Research Grant No. N00014-89-J-1565, and Joint Services Electronics Program Grant No. N00014-89-J-1023. I am grateful for a National Science Foundation Fellowship during the first three years of my graduate study.